PRODUCTION OF CARBON NANOTUBES USING Fe-FSM-16, Co-FSM-16 AND Ni-FSM-16 TYPE MESOPOROUS CATALYTIC MATERIALS BY CHEMICAL VAPOR DEPOSITION

by

Sinem TAŞ

Submitted to the Graduate School of Engineering and Natural Sciences
in partial fulfillment of
the requirements for the degree of
Master of Science

Sabancı University
February, 2011

PRODUCTION OF CARBON NANOTUBES
USING Fe-FSM-16, Co-FSM-16 AND Ni-FSM-16 TYPE
MESOPOROUS CATALYTIC MATERIALS
BY CHEMICAL VAPOR DEPOSITION

APPROVED BY:

Prof. Dr. Yuda Yürüm ……
(Thesis Advisor)

Prof. Dr. Selahattin Gültekin ……

Prof. Dr. Ferhat Yardım ……

Assist. Prof. Dr. Burç Mısırlıoğlu ……

Assist. Prof. Dr. Selmiye Alkan Gürsel ……

DATE OF APPROVAL: ……

To my family

PRODUCTION OF CARBON NANOTUBES USING Fe-FSM-16, Co-FSM-16 AND Ni-FSM-16 TYPE MESOPOROUS CATALYTIC MATERIALS BY CHEMICAL VAPOR DEPOSITION

Sinem TAŞ

MAT, Master of Science Thesis, 2011

Thesis Supervisor: Prof. Dr. Yuda Yürüm

Keywords: Carbon nanotubes, Chemical vapour deposition, FSM-16, Acetylene

Abstract

FSM-16 was synthesized and loaded with 2 and 4 wt % Fe, Co, and Ni by impregnation method. These catalytic materials were tested in the production of carbon nanotubes using the CVD method. The synthesized materials were characterized by XRD, ^{29}Si-NMR, N_2 physisorption, and SEM-EDS. The effect of metal concentration on structural characteristics of the mesoporous material was studied. XRD results demonstrated that Fe, Co and Ni modified FSM-16 had hexagonal mesoporous structure. However, both XRD and ^{29}Si-NMR characterization proved, as the metal concentration increased, hexagonal mesoporous structure was partially lost. According to BET results, the surface area, pore volume and pore diameter decreased due to metal impregnation. This was an indication of deterioration of silica matrix. SEM results exhibited the morphological differences between FSM-16 and Fe, Co, and Ni modified FSM-16.

Effect of experimental parameters such as metal concentration, reaction temperature and acetylene flow rate for CNTs growth were investigated by using Fe-FSM-16, Co-FSM-16, and Ni-FSM-16. Synthesized CNTs were characterized by SEM, Raman spectroscopy and TGA. It was found that metal concentration (2-4 wt %), and reaction temparature (500-800^{o}C) were critical for CNTs formation. While each catalyst exhibited high production of CNTs at 700^{o}C; and, they were inactive at 500^{o}C. The

diameter of CNTs changed with synthesis temperature, in particular the diameter of the CNTs increased with the reaction temperature. Ni-FSM-16 and Co-FSM-16 showed somewhat lower reactivity in formation CNTs with respect to Fe-FSM-16. Among the catalysts, 4 wt % Fe-FSM-16 improved the formation of CNTs. The effect of acetylene flow rate for CNTs diameters which grown on the 4 wt % Fe-FSM-16 was studied. It was observed that acetylene flow rate did not affect on the diameter of the synthesized CNTs significantly. Diameters of CNTs were almost the same, observed to be in the range of 20-35 nm. Raman measurement indicated that the synthesized products were MWCNTs since no SWCNTs characteristic features appeared in the RBM region.

The characterization results demonstrated that CNTs formation with high efficiency was performed by using 4 wt % Fe-FSM-16 with 80 mL/min acetylene flow rate at 700^{o}C for 30 min.

Fe-FSM-16, Co-FSM-16 VE Ni-FSM-16 TİPİ KATALİTİK MALZEMELER KULLANILARAK KARBON NANOTÜPLERİN KİMYASAL BUHAR DEPOLAMA İLE ÜRETİLMESİ

Sinem TAŞ

MAT, Yüksek Lisans Tezi, 2011

Tez Danışmanı: Prof. Dr. Yuda Yürüm

Anahtar Kelimeler: Karbon nanotüp, kimyasal buhar biriktirme, FSM-16, Asetilen

Özet

Bu çalışmada, FSM-16 tipi mezogözenekli malzeme sentezlenmiş ve bu malzemeye sonradan ekleme (impregnation) yöntemi ile ağırlıkça % 2 ve % 4 Fe, Co ve Ni yüklenmiştir. Bu katalitik malzemeler, karbon nanotüp üretimi için kimyasal buhar biriktirme reaksiyonunda test edilmişlerdir. Sentezlenen malzemeler XRD, ^{29}Si-NMR, N_2 fiziksel adsorplanmasi ve SEM-EDS ile karakterize edilmistir. Metal derişiminin, mezogözenek düzeni üzerine etkisi incelenmiştir. XRD sonuçları; Fe, Co ve Ni ile modifiye edilmiş FSM-16'nın mezogözenekli yapıya sahip olduğunu göstermiştir. Ancak; XRD ve ^{29}Si-NMR sonuçları; metal konsantrasyonu artıkça, hekzagonal mezogözenekli yapının kısmen kaybolduğunu kanıtlamaktadır. BET sonuçlarına göze, sonradan metal eklenmesi nedeniyle yüzey alanı, gözenek hacmi ve gözek çaplarında azalma olmuştur. Bu, silika matrisindeki bozulmasın bir göstergesidir. SEM sonuçları FSM-16 ile Fe, Co, ve Ni modifye edilmiş FSM-16 arasındaki morfolojik farklılıkları sergilemektedir. Karbon nanotüp büyümesini, metal konsantrasyonu, reaksiyon sıcaklığı ve asetilen akış hızı gibi deneysel parametrelerin nasıl etkilediği; Fe-FSM-16, Co-FSM-16 ve Ni-FSM-16 kullanılarak incelenmiştir. Sentezlenen karbon nanotüpler, SEM, Raman Spektroskopisi ve TGA ile karakterize edildi. Metal konsantrasyonun (ağırlıkça % 2 ve % 4) ve reaksiyon sıcaklığının (500^{o}C-800^{o}C), karbon nanotüp oluşumu için önemli olduğu belirlenmiştir. Bu katalizörlerin kullanıldığı deneylerde 500^{o}C de karbon

nanotüp oluşumu gözlenmezken, 700^{o}C de yüksek miktarlarda karbon nanotüp elde edilmiştir. Sentezlenen karbon nanotüplerin çaplarının reaksiyon sıcaklığının artması yönünde büyüdüğü gözlenmiştir. Ni-FSM-16 ve Co-FSM-16, Fe-FSM-16'ya göre karbon nanotüp oluşumuna daha düşük reaktivite göstermiştir. Katalizörler arasında en yüksek miktarda karbon nanotüp üretiminin % 4 Fe-FSM-16 kullanıldığı deneylerde olduğu gözlenmiştir. % 4 Fe-FSM-16 üzerinde büyüyen karbon nanotüplerin çaplarına asetilen akış hızının etkisi incelenmiş, asetilen akış hızının, sentezlenen karbon nanotüplerin çapları üzerinende önemli bir etkisi olmadığı gözlenmiştir. Elde edilen karbon nanotüplerin çaplarının 20-35 nm olduğu saptanmıştır. Raman spektroskopisi bulguları, RBM bölgesinde tek duvarlı nanotüplerin hiçbir karakteristik özelliğini göstermediğinden, sentezlenen ürünlerin çok duvarlı karbon nanotüp olduğunu göstermiştir.

Yüksek verimlilikte karbon nanotüp üretiminin optimum deney parametreleri olarak reaksiyon süresinin 30 dakika, sıcaklığın 700^{o}C, asetilen akış hızının 80 mL/dak ve katalizörün % 4 Fe-FSM-16 olduğu saptanmıştır.

Acknowledgments

First of all, I would like thank to my supervisor Prof. Dr. Yuda Yürüm for his guidance during my research and study at Sabanci University. His guidance helped me in all the time of research and writing of this thesis.

I would specially thank to my committee members, Prof. Dr. Selahattin Gültekin, Prof. Dr. Ferhat Yardım, Assist. Prof. Dr. Burç Mısırlıoğlu and Assist. Prof. Dr. Selmiye Alkan Gürsel for their contributions. Also special thanks to Assoc. Prof. Dr. Mustafa Çulha and his PhD student Mehmet Kahraman for the Raman Spectroscopy Measurement at Yeditepe University. Additionally, I thank Prof. Dr. Zeki Aktaş for the BET measurements at Ankara University and also for his positive attitude. I wish to extend my thanks to all faculty members of Material Science and Engineering Program and Burçin Yıldız for their support and understanding.

I convey special acknowledgement to Yeliz Ekinci, Elif Özden, Burcu Özel, Firuze Okyay, Lale Işıkel Şanlı and Hale Bolat for their valuable friendship. And then there are all the other people who have made Sabanci University a very special place over two years: Özlem Kocabaş, Burcu Saner, Aslı Nalbant Ergun, Mustafa Baysal, Taner Aytun, Kaan Bilge, Gülcan Çorapçıoğlu, Melike Mercan Yıldızhan, Shalima Shawuti, Zuhal Taşdemir, Eren Şimşek, Özge Malay, Seda Aksel, Ayça Abakay, Gönül Kuloğlu, Murat Gökhan Eskin, Dr. Çınar Öncel, Kaan Taha Öner, Nimet Aksoy, and Umman Mahir Yıldırım. Furthermore, I am thankful to TUBITAK for providing me scholarship and project funding (TUBITAK 109M214) during my thesis.

Finally, my deepest gratitude goes to my family for their love and support throughout my life; this dissertation is simply impossible without them.

Table of Contents

1. Introduction **1**

2. Literature Review on Carbon Nanotubes **3**

2.1 Discovery of Carbon Nanotubes 3

2.2 Structure of Carbon Nanotubes 6

2.2.1 Types of Carbon Nanotubes 7

2.3 Properties of Carbon Nanotubes 8

2.3.1 Chemical Reactivity 8

2.3.2 Electrical conductivity 8

2.3.3 Mechanical Properties 8

2.4 Carbon Nanotube Synthesis Methods 9

2.4.1 Arc Discharge Method 9

2.4.2 Laser-Ablation Method 10

2.4.3 Chemical Vapor Deposition (CVD) Method 12

2.5 Growth Mechanism of Carbon Nanotubes 13

2.6 Application Fields of Carbon Nanotubes 16

2.6.1 Composite 16

2.6.2 Field Emission Devices 16

2.6.3 Sensor 16

2.6.4 Hydrogen Storage 17

3. Literature Review on Catalyst **18**

3.1 Mesoporous Materials 18

3.2 Folded Sheet Materials Derived From Layered Silicates 19

3.2.1 Layered Silicates 20

3.2.2 FSM-16 20

3.2.3 KSW-2 21

3.3 Characterization Methods of Mesoporous Material FSM-16 22

3.3.1 X-ray Diffraction 22

3.3.2 N_2 Physisorption 22
3.3.3 Electron Microscopy 23
3.3.4 ^{29}Si-NMR 23
3.4 Studies from Literature about Catalyst Materials 24

4. Experimental **27**
4.1 Materials 27
4.2 Catalyst Preparation 27
4.2.1 Preparation of Kanemite 28
4.2.2 Synthesis of FSM-16 28
4.2.3 Synthesis of Fe-FSM-16, Co-FSM-16, and Ni-FSM-16 28
4.3 Catalyst Characterization 28
4.3.1 X-ray Diffraction Measurements (XRD) 29
4.3.2 NMR Measurements 29
4.3.3 Surface Analysis Tests 29
4.3.4 Scanning Electron Microscopy 29
4.4 Carbon Nanotube Production 30
4.5 Carbon Nanotube Characterization 31

5. Results and Discussion **34**
5.1 Catalyst Characterization 34
5.1.1 XRD Analysis 34
5.1.2 ^{29}Si-NMR Analysis 38
5.1.3 N_2 Physisorption Analysis 39
5.1.4 SEM-EDS Analysis 46
5.2 Carbon Nanotube Characterization 49
5.2.1 Effect of Catalyst 49
5.2.2 Effect of Temperature 53
5.2.3 Effect of Acetylene Flow Rate 62
5.2.4 Raman Spectroscopy Analysis 65
5.2.5 TGA Analysis 69

6. Conclusion **75**

List of Figures

Figure 2.1: Carbon allotropes: a) graphite, b) diamond, d) fullerenes. 3
Figure 2.2 : Iijima's TEM micrographs. 5
Figure 2.2 : Iijima's TEM micrographs. 5
Figure 2.3 : TEM images of carbon nanotubes published in 1952. 5
Figure 2.4 : The unrolled honeycomb lattice of a nanotube 6
Figure 2.5 : Schematic representation of three types of single-wall carbon nanotubes: (a) the "armchair" nanotube; (b) the "zigzag" nanotube; and (c) the"chiral" nanotube. 7
Figure 2.6 : Structures of a) single-walled carbon nanotube (SWNT) and b) multi-walled carbon nanotube (MWNT) 7
Figure 2.7: Experimental set-up of an arc discharge apparatus 10
Figure 2.8 : Schematic representation of laser ablation method. 11
Figure 2.9 : Tem images of SWCNTs are grown by laser ablation method. 11
Figure 2.10 : Schematic representation of CVD system. 12
Figure 2.11 : The SEM images of carbon nanotubes grown on Si substrate. 13
Figure 2.12 : Schematic representation of tip growth (a-c) and base growth (d-f). . 11
Figure 3.1 : Structure of a) MCM-41, b) MCM-48. 19
Figure 3.2 : Graphical depiction of tetrahedra. 20
Figure 3.3 : Schematic model for the formation of FSM-16 21
Figure 3.4 : a) The schematic representation of proposed model of KSW-2 b) typical TEM image of KSW-2 21
Figure 3.5 : Schematic illustration of electronic interactions in chemisorption. A filled orbital on the adsorbate overlaps with an empty one on the metal. 24
Figure 4.1 : CVD set-up for CNTs production 30
Figure 5.1 : XRD pattern of kanemite. 34
Figure 5.2 : XRD pattern of FSM-16 and Fe impregnated FSM-16. 36
Figure 5.3 : XRD pattern of FSM-16,Co and Ni impregnated FSM-16. 37
Figure 5.4 : NMR spectra of a) FSM-16 after calcination,b) FSM-16 before calcination. 38

Figure 5.5 : ^{29}Si NMR spectra for (a) FSM-16,(b) 2 wt % Ni-FSM-16, (c) 4 wt % Ni-FSM-16, (d) 2 wt % Fe-FSM-16, (e) 4 wt % Fe-FSM-16, (f) 2 wt % Co-FSM-16, (g) 4 wt % Co-FSM-16 39
Figure 5.6 : Adsorption-desorption isotherms for FSM-16 and iron modified FSM-16 41
Figure 5.7 : Adsorption-desorption isotherms for cobalt-modified FSM-16 42
Figure 5.8 : Adsorption-desorption isotherms for nickel-modified FSM-16 43
Figure 5.9: Pore size distribution of FSM-16 and Fe modified FSM-16..... 44
Figure 5.10 : Pore size distribution of Co and Ni modified FSM-16 45
Figure 5.11 : SEM images of kanemite 46
Figure 5.12 : SEM images of FSM-16..... 47
Figure 5.13 : SEM images of a) 4 wt % Fe-FSM-16 and b) 2 wt % Fe-FSM-16..... 47
Figure 5.14 : SEM images of a) 4 wt % Co-FSM-16 and b) 2 wt % Co-FSM-16 ... 48
Figure 5.15 : SEM images of a) 4 wt % Ni-FSM-16 and b) 2 wt % Ni-FSM-16..... 48
Figure 5.16 : A set of SEM micrographs of Fe catalyzed CNTs: a) 2 wt % Fe-FSM-16 and b) 4 wt % Fe-FSM-16..... 50
Figure 5.17 : A set of SEM micrographs of Fe catalyzed CNTs: a) 2 wt % Co-FSM-16 and b) 4 wt % Co-FSM-16..... 51
Figure 5.18: A set of SEM micrographs of Fe catalyzed CNTs: a) 2 wt % Ni-FSM-16 and b) 4 wt % Ni-FSM-16..... 52
Figure 5.19 : CNTs growth over 4 wt % Fe- FSM-16 at 600^{o} C 54
Figure 5.20 : CNTs growth over 4 wt % Fe- FSM-16 at 800^{o} C 55
Figure 5.21 : CNTs growth over 2 wt % Fe- FSM-16 at 600^{o} C 55
Figure 5.22 : CNTs growth over 2 wt % Fe- FSM-16 at 800^{o} C 56
Figure 5.23 : Iron - carbon binary phase diagram 57
Figure 5.24 : CNTs growth over: a) 4 wt % Fe-FSM-16 at 800^{o}C b) 4 wt % Ni-FSM-16 at 800^{o}C..... 58
Figure 5.25 : Carbon deposition change as a function of reaction temperature 60
Figure 5.26: Carbon conversion change as a function of reaction temperature 61
Figure 5.27 : Amounts and conversion of carbon with different flow rate of acetylene 62
Figure 5.28 : CNTs growth over 4 wt % Fe-FSM-16 with a) 60 ml/min acetylene flow rate, b) 80 ml/min acetylene flow rate 63

Figure 5.29 : CNTs growth over 4 wt % Fe-FSM-16 with a) 60 ml/min acetylene flow rate, b) 80 ml/min acetylene flow rate 64
Figure 5.30 : Raman spectra of carbon deposits on metal-FSM-16 at 700^{o}C 65
Figure 5.31 : Raman spectra of carbon deposits on 4 wt % Fe-FSM-16 at different temperatures 67
Figure 5.32 : Raman spectra of carbon deposits on 4 wt % Fe-FSM-16 produced with different acetylene flow rates at 700^{o}C 68
Figure 5.33 : TGA thermograms of CNTs grown over a) 4 wt % Fe-FSM-16, b) 4 wt % Co-FSM-16, and c) 4 wt % Ni-FSM-16 70
Figure 5.34 : DTA curves of CNTs grown over a) 4 wt % Fe-FSM-16, b) 4 wt % Co-FSM-16, and c) 4 wt % Ni-FSM-16 71
Figure 5.35 : TGA thermograms of CNT growth with various acetylene flow rate 73
Figure 5.36 : DTA curves of CNT growth with various acetylene flow rate 73

List of Tables

Table 2.1: Variation of Young's modulus found for different carbon nanotubes 9
Table 4.1: Optimization experiments for the growth of CNTs through CVD 32
Table 4.2: Flow rate experiments for 4 wt % Fe-FSM-16 at 700 ^{o}C 33
Table 5.1: d_{100} and *a* values for catalysts 36
Table 5.2: Results of specific surface area, pore size and pore volume of samples . 40
Table 5.3: EDS analysis of Fe, Co and Ni impregnated FSM-16 46
Table 5.4 : The yield of carbon deposition at 700^{o}C 49
Table 5.5 : Parameters of D and G band for carbon deposits on metal-FSM-16 at 700^{o}C 66
Table 5.6 : Parameters of D and G band for carbon deposits on 4 wt % Fe -FSM-16 at different temperature 68
Table 5.7 : Parameters of D and G band for carbon deposits on 4 wt % Fe -FSM-16 produced with different acetylene flow rates at 700^{o}C 69
Table 5.8 : Onset, inflection and end temperature obtained from DTG curve 72
Table 5.9 : Results of onset, inflection and end temperature with various acetylene flow rate obtained from DTG curve 72

CHAPTER 1

INTRODUCTION

Discovery of carbon nanotubes is an important stepping stone for the nanotechnological progress. Because of a strong knowledge on electrical and mechanical properties of CNTs, they find many application fields including polymer reinforcements for composites, energy storage, and electronics [1]. However, cost effective production of CNTs is an important issue. Generally, CNTs are synthesized by three different production methods. These are arc discharge, laser ablation and chemical vapor deposition methods. Both arc discharge and laser ablation method are very difficult to scale up. On the other hand, due to its simplicity, low cost, and easily controlled growth factors, CVD (chemical vapor deposition) method is the most promising method for industrial scale production of CNTs [2]. Basically, CVD process is dissociation of hydrocarbon molecules on the metal catalyst at high temperatures (500^{o}C-1000^{o}C) for certain period of time. Precipitation of carbon on metal particles leads to formation of CNTs. Working conditions of CVD such as temperature, hydrocarbon concentration, size and pretreatment of metallic catalyst, and time of the reaction effect the quality of final product. And single-wall carbon nanotubes (SWCNTs) and multi-wall carbon nanotubes (MWCNTs) can be produced depending on reaction conditions [3]. Because of CVD process depends on catalytic decomposition of hydrocarbon molecules, the role of catalyst is important for ability of CNT formation. Metal particle size is crucial for control of CNT diameter. Supported catalysts ensure the control of particle size for the growth process. Ordered mesoporous molecular sieves are preferred as a support material because of high specific surface area, large pore volume, uniform pore structure, and tunable pore size varying from 2 to 10 nm [4]. Among the mesoporous materials, FSM-16 is a good candidate because of its large and hexagonal pore structure with high specific surface area. Indeed, ordered structure of FSM-16 ensures the good dispersion of metal particles. When FSM-16 is modified with metal particles, it can be used as a catalyst for various reactions. Fe, Ni, and Co is the common preferred metals for CNT production by CVD method.

In this thesis work, Fe-FSM-16, Co-FSM-16, and Ni-FSM-16 catalysts were synthesized and characterized by X-ray diffraction measurements (XRD), ^{29}Si-NMR, surface analysis tests and scanning electron microscopy (SEM). These catalysts were used for CNTs production. The effect of Fe, Co, and Ni catalysts, metal concentrations, and CVD temperature on the CNTs production was investigated. During this study acetylene (C_2H_2) was used as a hydrocarbon source. The growth and structure of CNTs were optimized. The morphology and crystallinity of CNTs grown on Fe, Co, and Ni catalysts were investigated using scanning electron microscopy, Raman spectroscopy, and thermogravimetric analysis.

CHAPTER 2

2. Literature Review on Carbon Nanotubes

2.1. Discovery of Carbon Nanotubes

Carbon is unique and widely distributed in the nature, moreover, exists in variety of compound in the nature. Combination with nitrogen, hydrogen and oxygen provides sizeable compounds; many of them are vital organic and life processes, therefore, without carbon life would be impossible.

Carbon has 6 electrons and listed at the top of the column IV. Electronic configuration end up with $1s^2\ 2s^2\ 2p^2$, this means that outer shell electrons are especially important for forming covalent bond. 2s and 2p orbital's sub-shells take a role in covalent bonding. The energy difference between 2s and $2p_x$, $2p_y$, and $2p_y$ orbitals are very small compared to binding energy of chemical bond. In carbon three hybridization states occur: sp, sp^2, and sp^3. Hybridization comes about through a mechanism, whereby; the electronic wave functions for these four electrons mix and construct new electronic state which enhances the binding energy of the carbon with its neighboring atom.

Carbon has also three allotropes. Graphite, diamond, and fullerenes are the best known forms of carbon.

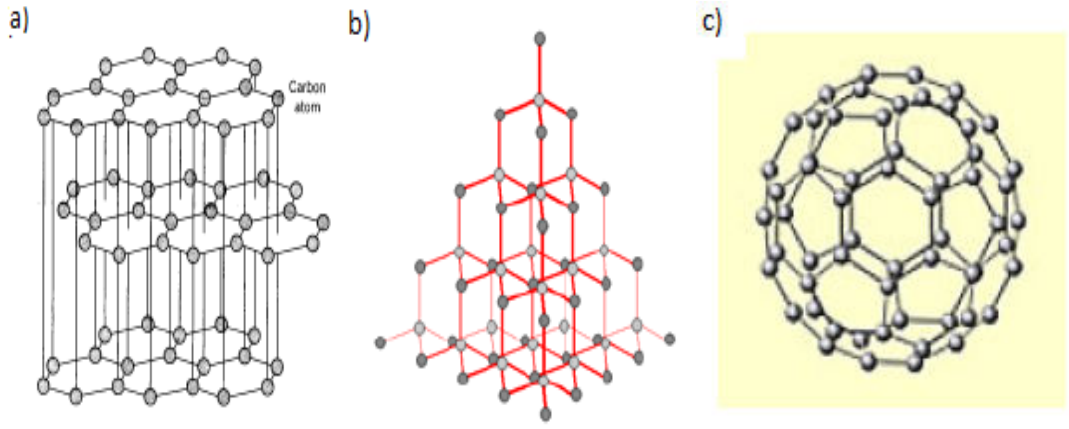

Figure 2.1: Carbon allotropes: a) graphite, b) diamond, d) fullerenes [5]

Graphite exists in a layered structure. Graphite is defined as hexagonal pattern of atoms arranged in a plane in which sp^2 hybridized C atoms are present with delocalized π electrons. Owing to delocalized π electrons makes graphite stronger than the other types of carbon allotropes. van der Waals forces hold the graphite layer together. Because of the weakness of this force, graphite layers can easily slide over one another. In diamond carbon atoms make sp^3 hybridization and tetrahedrally bonded to other carbon atoms. As a consequence of strong carbon-carbon bond, diamond is one of the hardest substances [6].

Fullerenes are the other type of carbon allotropes. Although, its structure is similar to graphite, they contain pentagonal rings. It has spherical, ellipsoid, and tubular forms. Spherical form are known as buckyballs, and cylindrical ones are described carbon nanotubes or buckytubes [7].

Carbon nanotubes are rolled graphene sheets into cylinders. Production and application of carbon nanotubes (CNTs) are new fields and emerge from new ideas. Due to their unique structural, mechanical, electronic, and optical properties, they attract more attention and continue to increase. The rapidly increasing ability of large scale production offers new opportunities in the design and application of CNTs. CNTs are part of the nanotechnological revolution. Most progress in CNTs production and applications are due to improvements in experimental techniques.

Clear CNTs evidence for discovery was first reported in 1991 by Iijima [8]. He synthesized carbon nanotubes by 'Arc-Discharge Evaporation' method and the tubes are depicted in Figure 2.2. Included at least two layers and their diameters varied from 5-20 nm. Although the Iijima's contribution created significant breakthroughs, he is not the first who published about carbon nanotubes. In 1952, Russian researchers Radushkevich and Lukyanovich achieved to illustrate some nano-sized carbon filaments by transmission electron microscopy. Unfortunately, this paper did not attract more attention because during the Cold War, it was difficult for Western scientists to reach Russian journals. However, in this early report, tube like image with the diameter in the range of 50 nm was observed, related images are shown in Figure 2.3.

Moreover, Oberlin in France published a paper in 1976 and showed carbon nanotubes by electron microscopy. He also succeeded to grow both double wall and multiwall carbon nanotubes by using vapor growth technique [9].

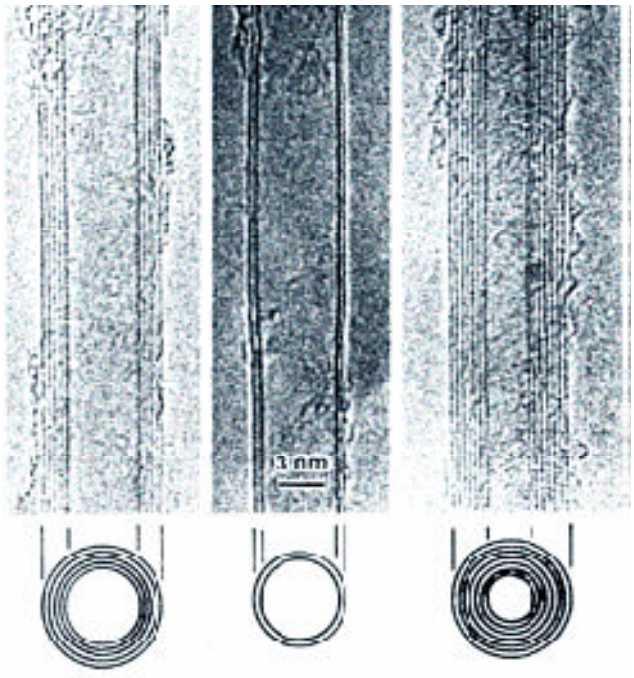

Figure 2.2: Iijima's TEM micrographs [8]

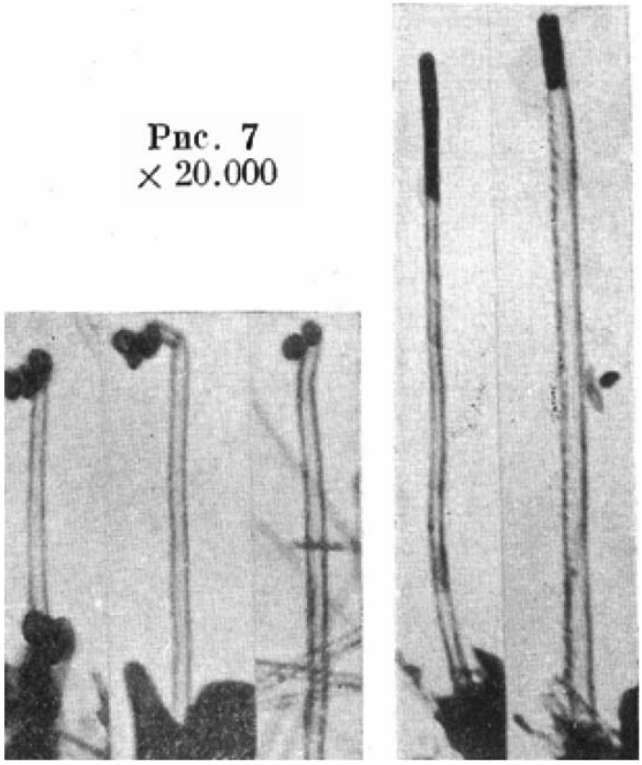

Figure 2.3: TEM images of carbon nanotubes published in 1952 [9]

2.2. Structure of Carbon Nanotubes

Carbon nanotubes are the curved form of the graphene sheets. Different microscopic structures and diameters of tubes are result of rolling type of the graphene sheet.

Structure of the carbon nanotubes is found by the help of chiral vector and chiral angle.Chiral vector are given by a formula;

$C_h = na_1 + ma_2$

where a_1 and a_2 are unit vectors and n,m are integers.

Figure 2.4 shows the chiral vector and angle. OA vector is the chiral vector of CNT that is perpendicular to nanotube axis. CNTs construction is governed by meeting equivalent sites O, A, B, and B' by rolling up the structure O and A points overlap with B and B'.

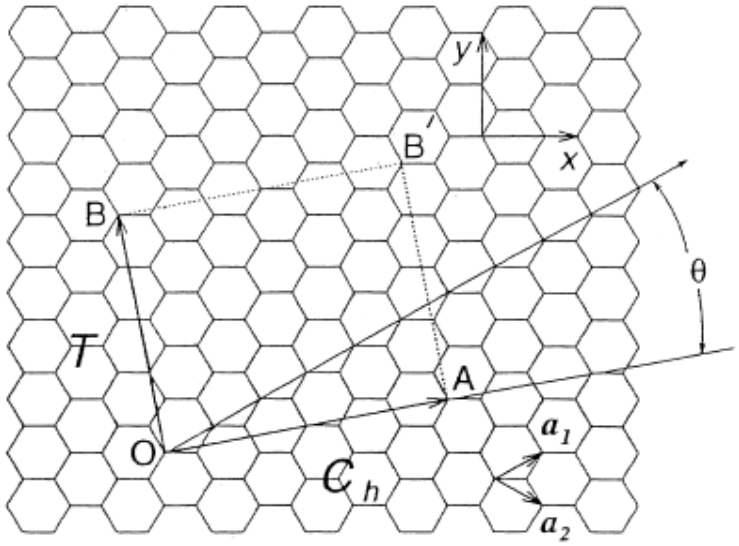

Figure 2.4: The unrolled honeycomb lattice of a nanotube [10]

Structure of CNTs draws much more interest because novel electrical properties are related to the structure of the tube. For a given (*n*,*m*) nanotube $n - m = 3p$,and where p is an integer; nanotube is metallic. If $n-m \neq 3p$, the nanotube is semiconducting

In addition to electrical properties, chiral vector also characterize the structure of the nanotube whether it is armchair, zigzag or chiral. Armchair nanotube (Fig 2.5.a) corresponds to the case of n=m is always show metallic character, and zigzag nanotube (Fig 2.5.b) corresponds the case of (n,0) which is metallic or semiconducting. All of the other (n,m) vectors are defined as chiral nanotube (Fig 2.5.c).

The chiral angle can be described as the angle between $\boldsymbol{C}_h$ and the unit vector $\boldsymbol{a}_1$, with values θ in the range between 0^o and 30^o. According to chiral angle, zigzag nanotubes has 0º, armchair nanotubes has 30º. Chiral angle which is greater than 0º and less than 30º corresponds to chiral nanotubes [11].

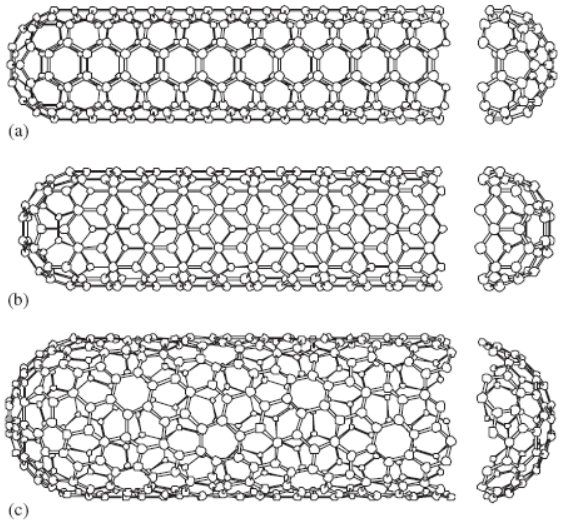

Figure 2.5: Schematic representation of three types of single-wall carbon nanotubes: (a) the "armchair" nanotube; (b) the "zigzag" nanotube; and (c) the"chiral" nanotube [12]

2.2.1. Types of Carbon Nanotubes

Carbon nanotubes classified according to number of graphene sheets rolled into a cylindrical shape. Single-wall carbon nanotube (SWCNT) can be described as a graphene sheet rolled into a cylinder, whereas, multiwall carbon nanotube (MWCNT) contains more than one layer.

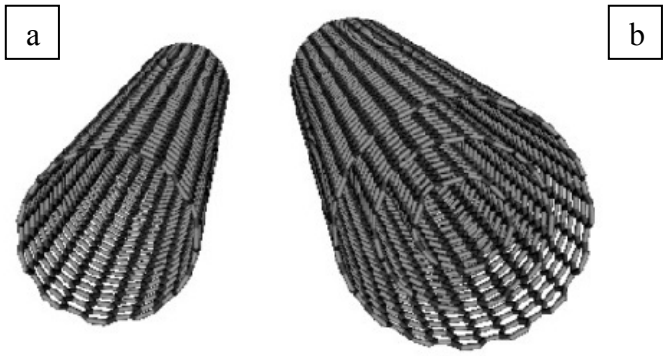

Figure 2.6: Structures of a) single-walled carbon nanotube (SWNT) and b) multi-walled carbon nanotube (MWNT) [13]

2.3. Properties of Carbon Nanotubes

2.3.1. Chemical Reactivity

Compared to a flat graphene sheet, carbon nanotubes are relatively higher chemical reactivity because of induce local strain due to curvature-induced pyramidalization and misalignment of the π-orbitals of the carbon atoms. Strain is directly related with pyramidalization of the conjugated carbon atoms, and π -orbital misalignment between adjacent pairs of conjugated carbon atoms. For that reason it is practical to consider carbon nanotube in two regions: the end caps and the side wall. End caps show higher chemical reactivity compared to side wall, because the carbon nanotubes resemble a hemispherical fullerene and it is difficult reduce pyramidalization angle. Therefore, it ensures the reactivity of end caps. Furthermore, its reactivity is irrespective of the diameter of the carbon nanotube. However, a smaller nanotube diameter has higher reactivity [14].

2.3.2. Electrical conductivity

Electronic structure and properties cannot be considered without ignoring the electronic properties of graphene sheet. As we discussed above, CNT is the folding form of graphene sheet. Therefore, chirality vector determines the CNT is whether conductor or semiconductor. CNTs show metallic behavior when $n=m$ or $(n-m) = 3p$, where p is an integer and n and m are defining the nanotube. While CNTs with $(n-m) \neq 3p$ are semiconducting. Moreover, band gap is inversely proportional to tube diameter [15].

2.3.3. Mechanical Properties

CNTs have important mechanical properties such as high Young modulus and strength. Like other properties, mechanical properties strongly depend on structure of nanotube, because high anisotropy of graphite. Therefore, composites will benefit from these great mechanical properties of CNTs [16]. Table 1 shows the variation of experimentally determined Young modulus and tensile strength.

Table 2.1: Variation of Young's modulus found for different carbon nanotubes [17]

Author	Young's modulus [TPa]	Nanotube type
Treacy *et al* [18]	1.8	$MWNT_{ARC}$
Krishnan *et al.*[19]	1.25	$SWNT_{LSR}$
Wong *et al.*[20]	1.28	$MWNT_{ARC}$
Salvetat *et al* [16]	0.81	$MWNT_{ARC}$
Salvetat *et al.*[21]	0.01-0.05	$MWNT_{CVD}$
Yu *et al.*[22]	0.27-0.95	$MWNT_{ARC}$
Demczyk *et al.*[23]	0.8	$MWNT_{ARC}$

2.4. Carbon Nanotube Synthesis Methods

There are number of methods for carbon nanotube production. Arc discharge, laser-ablation method, and chemical vapor deposition method are the most popular nanotube synthesis methods. Among these methods, CVD is the most suitable method for industrial scale carbon nanotube production.

2.4.1. Arc Discharge Method

Arc Discharge method is initially used for fullerenes production, however, now it is a common method is for nanotube production. This system includes two carbon rods and the method depends on applying a low voltage (20-40 V) and a DC current (nearly 50-100 Å) between cathode and anode. The discharge vaporizes the anode and form nanotubes deposit on the cathode surface.

Evaporation process is usually done in an inert atmosphere. Amount of argon and helium in the mixture affects nanotube diameter. During the arc discharge process, diffusions coefficients and thermal conductivities change affect the speed with which the carbon and catalyst molecules diffuse and cool on the cathode surface. As a result, tube diameter is affected. An arc-discharge apparatus is depicted in Figure 2.7 [24].

It is possible to synthesize both MWCNTs and SWCNTs with this method. If SWCNTs are desired, the anode has to be doped with metal catalysts such as Fe, Co, Ni, Y or Mo. Quality of the nanotube depends on the metal concentration, inert gas pressure, kind of gas, the current. The tube diameter is in the range of 1.2 to 1.4 nm. On the other hand, no catalysts are used in MWCNTs production, so both electrodes are graphite. The typical size for MWCNTs are an inner diameter of 1-3 nm and an outer diameter of approximately 10 nm [25].

The main disadvantage of this process is a lot of side products are formed such as fullerenes, amorphous carbon, and some graphite sheets and it needs purification [26].

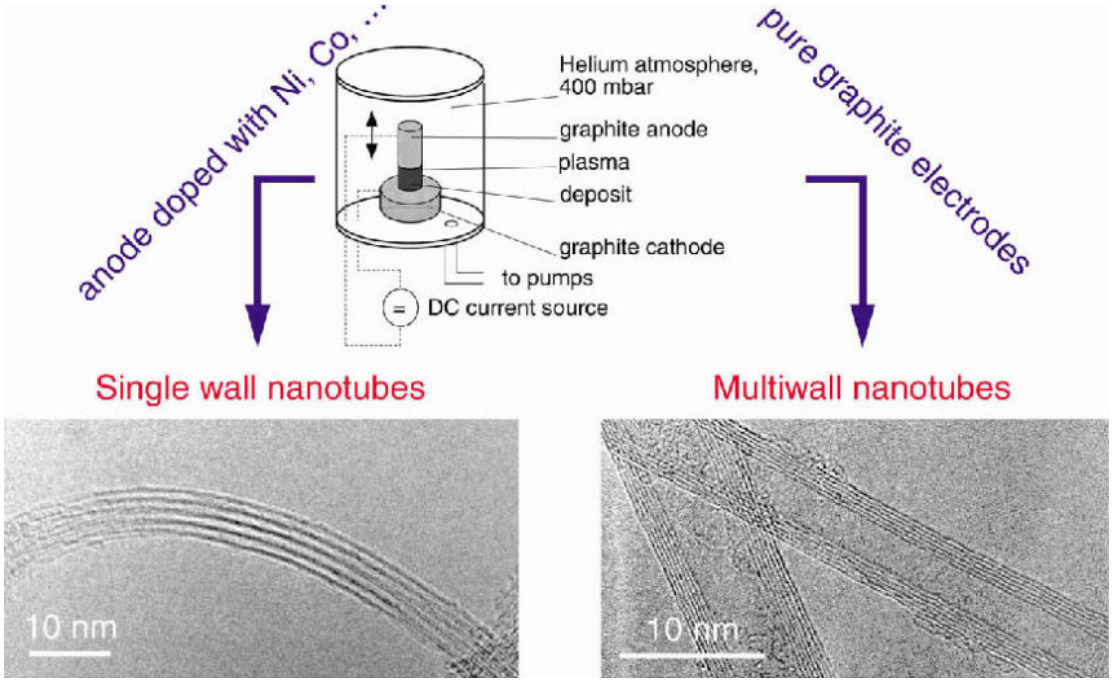

Figure 2.7: Experimental set-up of an arc discharge apparatus [25]

2.4.2. Laser-Ablation Method

Laser-ablation method is the efficient route for bundles of carbon nanotubes synthesis with narrow diameter distribution. Carbon nanotube synthesis with this method was first introduced by Smalley's group at Rice University in 1995 [27].

Like arc discharge method, laser-ablation method involves evaporation of solid carbon. Laser pulses are used to evaporate carbon under 1200 ^{o}C. Flowing argon through the tube removes the nanotube from high temperature zone to water collected Cu-collector [11]. Illustration of typical laser ablation system is depicted in Figure 2.8.

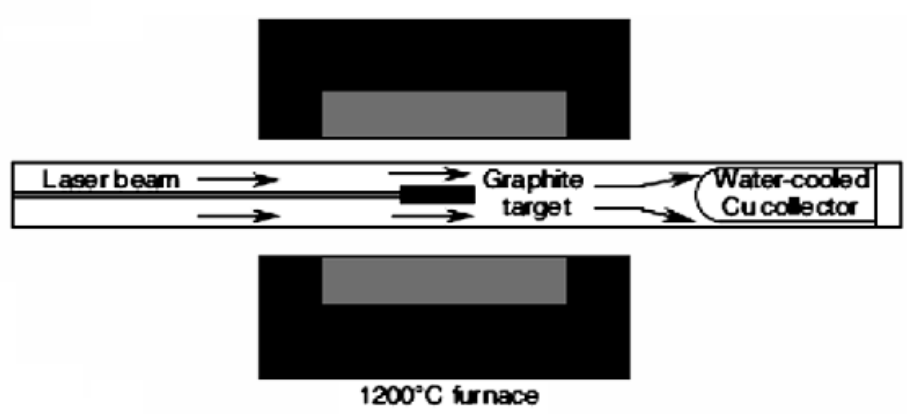

Figure 2.8: Schematic representation of laser ablation method [3]

MWCNTs would be produced with pure graphite electrodes. On the other hand, SWCNTs could be synthesized with a mixture of graphite with metal catalyst instead of pure graphite electrode. An image of SWNTs are grown by laser-ablation is illustrated in Figure 2.9. Nanotube produced with this method has high purity and the system can be scaled up, however but the technique is rather expensive due to the laser and the large amount of power required [25].

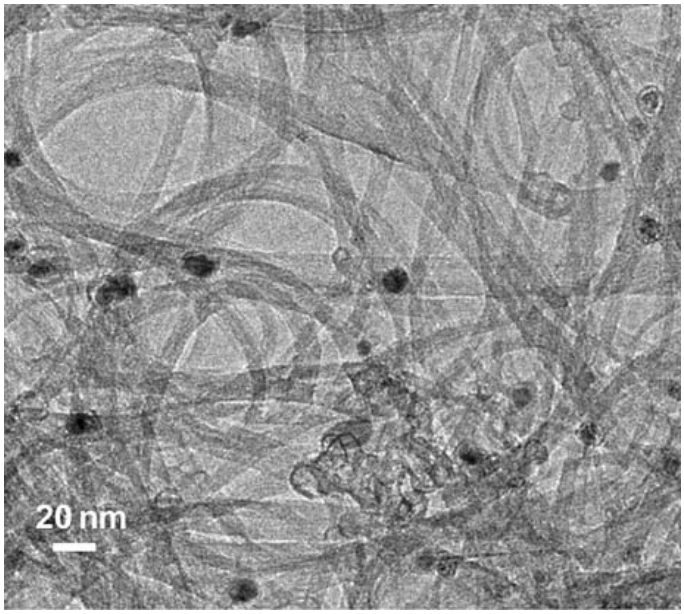

Figure 2.9: TEM images of SWCNTs are grown by laser ablation method [28]

2.4.3. Chemical Vapor Deposition (CVD) Method

Although, CVD is widely used in today for generating nanotube, catalyzed decomposition of hydrocarbon gas has been already known to generate carbon fiber. However, in 1993 Yacaman and his coworkers successfully synthesized MWCNT by this method. They reported nanotube production with using acetylene as a hydrocarbon gas and iron as a catalyst at 700 ^{o}C [29].

Development of CVD system for carbon nanotube production is an important stepping stone towards the high scalability and cost reduction because this system is being operated at low temperature compared to other methods. For that reason CVD exhibits significant performance for to control tube diameter and length. Therefore, among these methods, CVD has further advantages such as capability to control size, shape, and alignment of nanotubes. Typical CVD system is shown in Figure 2.10.

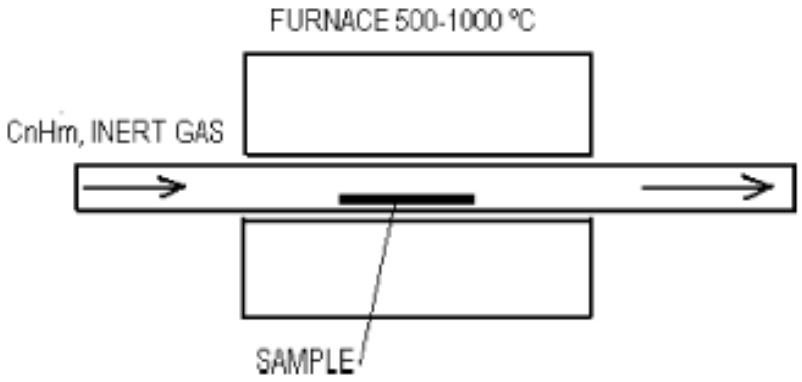

Figure 2.10: Schematic representation of CVD system [1]

This method based decomposition of hydrocarbon gas in the presence of catalyst at moderate temperature. There are four two main steps during the process:

i. Catalyst preparation: sputtering transition metal onto substrate and then forming catalyst particles by chemical etching or thermal annealling.
ii. Synthesis of carbon nanotube: sending hydrocarbon source to the furnace and then decomposition of the gas followed by nanotube growth.

To meet the demand for CVD operation, type of catalyst is critical. In previous reports, transition metals such as Fe, Ni, and Co are commonly used. In addition to these, Sc, Ti, V, Cr, Mn and combination of them are used as a catalyst. For CVD of CNTs, methane, acetylene, ethylene, carbon monoxide, benzene, and ethanol are preferred as a carbon

precursor [30]. The CNTs is seen in Figure 2.11 was synthesized over Ni-deposited Si substrate annealing with ammonia by pyrolysis of acetylene at 900 ^{0}C [31].

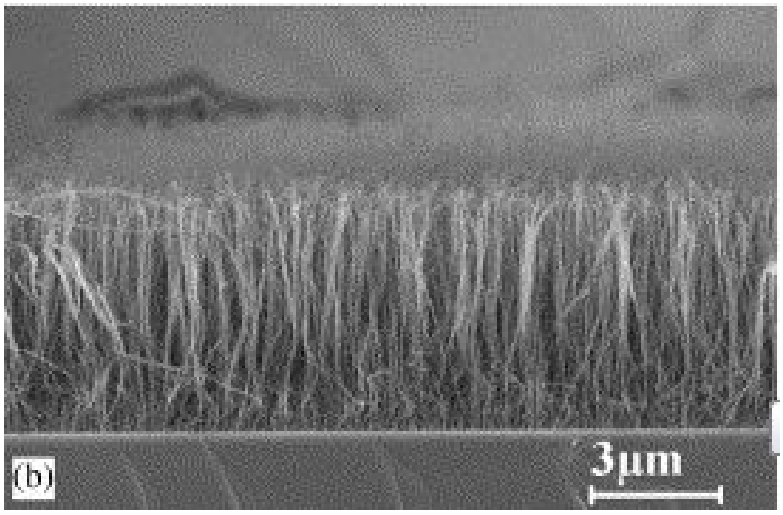

Figure 2.11: The SEM images of carbon nanotubes grown on Si substrate

2.5. The Growth Mechanism of Carbon Nanotubes

This part mainly focuses on the catalytic growth of carbon nanotube. Actually the growth mechanism is still debated. Because of this controversy, there are several theories to explain growth mechanism.

VLS (vapor–liquid–solid) theory developed by Wagner and Ellis [32], in general, can be defined as the liquid becomes supersaturated with vapor phase and then crystal growth initiate followed by precipitation at the solid-liquid interface. VLS is a process where, in a first step carbon precursor creates surface carbon on the metal particles form metal carbide by catalytic decomposition. This stage efficiency depends on reconstruction of catalyst surface; details of surface chemistry, chemical nature of catalyst. This mechanism may be carried out by solution–diffusion–precipitation process that generates graphite filaments. At this point, the carbon diffusion within the catalyst and temperature gradient due to exothermic decomposition and endothermic deposition of carbon are the driving forces. In fact carbon precursor exothermally decomposed on the metal particle and then diffuses to cooler part. Knowledge of thermodynamic, less carbon dissolved on the cooler part. So, the supersaturation on the cooler side leads to segregation of carbon atoms and form graphitic layer. Generation of more graphitic planes conclude as plane bending. Outcome of the bending is

overlapping sp^2 orbitals of graphitic layer with metal orbitals. As a result this contact serves as a seed for crystallization as well as nanotube growth [33-35].

The metal support adhesion is important to mention that because of leading to tip growth or base growth. Weak interaction between substrate and metal particles promote tip growth so catalyst particles are lifted off the substrate and located at the top of the CNTs. In tip growth, carbon diffuses around the catalytic particles and graphitization process begins. Conversely, carbon diffuses into the catalytic particle interior [36]. These processes are illustrated in Figure 2.12.

In terms of nanotube length, base growth promotes shorter nanotubes because cap formation is energetically favorable compared to base growth. In consequence, smaller tubes can accommodate with the base growth mode. Moreover, catalytic particle size influence tube diameter. It was emphasized that, CNTs grown in tip growth exhibits large diameters compared to those for base growth [37].

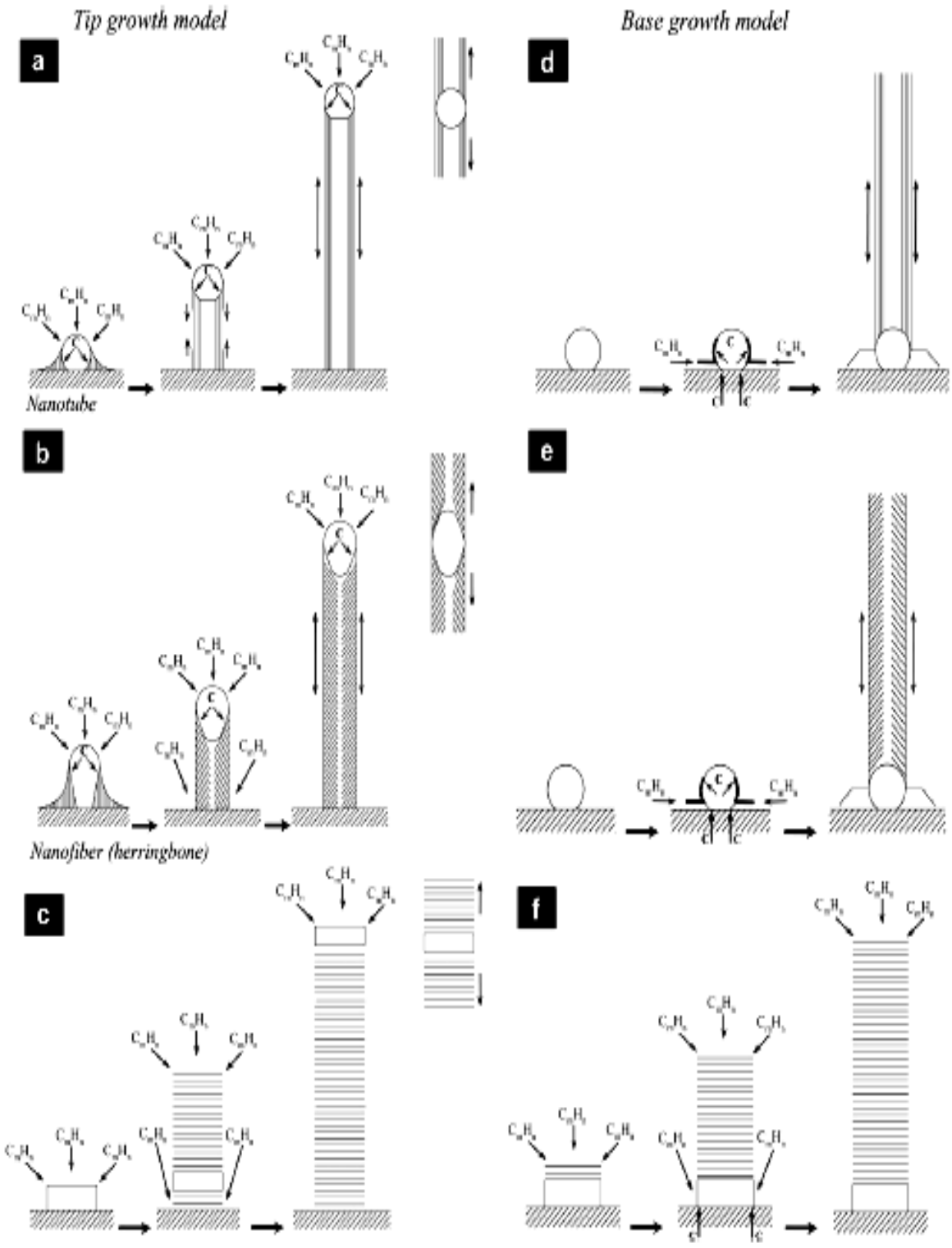

Figure 2.12: Schematic representation of tip growth (a-c) and base growth (d-f)

2.6. Application Fields of Carbon Nanotubes

At this time, there is an increasing understanding the carbon nanotube's unique properties, carbon nanotubes are extensively used in many fields such as composites, sensor and probes, field emission device and energy storage.

2.6.1. Composite

CNTs can generate inherently novel effects for development of high-strength and high-stiffness polymer composites. Indeed, unique mechanical and electrical properties of nanotubes makes them good reinforcing agent. Suitable environment should be established for transferring the mechanical load or electrical charge to individual nanotubes in a polymer composite component. Efficient dispersion can be created with covalent and non-covalent bonding. However, a primary difficulty is achieving a good dispersion of nanotubes in a composite. Without proper dispersion, nanotubes aggregates and then act as defect sites which limit the mechanical performance. Obviously, it is possible to enhance mechanical properties and electrical conductivity of polymer resin. In terms of tensile modulus, polymer composites with functionalized nanotube filler exhibit tremendous increase in mechanical properties as well as electrical properties [38].

2.6.2. Field Emission Devices

In the field emission devices, carbon nanotubes are used as emissive material which has low threshold emission fields and stable at high current density. Nanometer size diameter, structural integrity, high electrical conductivity, and chemical stability make them good candidate. Metals have already used as an emissive material; however their unstable behavior under high current density limits their application. Potential application field of nanotubes are: flat panel displays, lamps, gas discharge tubes providing surge protection, and X-ray and microwave generators [3].

2.6.3. Sensor

Carbon nanotubes are also preferred for sensing applications. Generally, vapour-sensitive polymers, semiconductor metal oxides and other porous structured materials such as porous silicon are preferred for gas sensing applications. The crucial parameters for gas sensors is high sensing, selectivity, stability, and fast response time. Carbon

nanotubes offer great applicability and cost reduction. Exposure to gas cause change in some properties of carbon nanotube. It has been demonstrated that, electrical properties are really sensitive exposed environment due to gas molecule adsorption. For instance, thermopower, resistance, and density of states of single SWNT or SWNT bundles show significant change after gas adsorption [39].

2.6.4. Hydrogen Storage

Carbon nanotubes represent a new way for solid-state hydrogen storage. The critical point is low ratio of stored hydrogen to carbon compared to hydrogen storage medium. However, researchers have made remarkable progresses. To reach desired storage capacity, and metals are introduced to increase hydrogen bonding capability as well as storage capacity [40].

CHAPTER 3

3. Literature Review on Catalyst

3.1. Mesoporous Materials

Porous materials are widely used because of their high surface area, large pore volumes and good thermal stability. New mesoporous templated materials are characterized by surfaces of more than 1000 m^2 g^{-1}. Due to their high surface area they are used in separation, adsorption and storage of gases, as catalyst and catalyst support material. According to the International Union of Pure and Applied Chemistry (IUPAC), porous materials are classified into three types;

1. Microporous Materials (< 2 nm)

2. Mesoporous Materials (2-50 nm)

3. Macroporous Materials (> 50 nm) depending on their pore size [41, 42].

Micropores material whose pore size less than 2 nm gathers more attention. Moreover, zeolites are highly crystalline aluminosilicates with a uniform pore structure has many promising applications. Its structural stability makes zeolites as a potential candidate for application in storage, as supports or as electrodes, and environmental technologies such as the removal of pollutants.

New type mesoporous materials were first discovered by Mobil researchers. The Mobil composite of matter (MCM) synthesize based on liquid crystal templating model with pore size greater than 2 nm and surface areas reaching 1000 m^2g^{-1}. Indeed, discovery of MCM type materials are crucial for the progress in the development of new mesoporous materials since they eliminate the limitations of zeolites. Fundamental difference between MCM family and zeolite is the amorphous pore wall structure.

MCM family has been classified into three groups: MCM-41(hexagonal), MCM-48 (cubic) (Figure 1), and MCM-50 (lamelar). Among all these members, MCM-41 is the most attractive one because of its unidirectional, hexagonal honeycomb like structure.

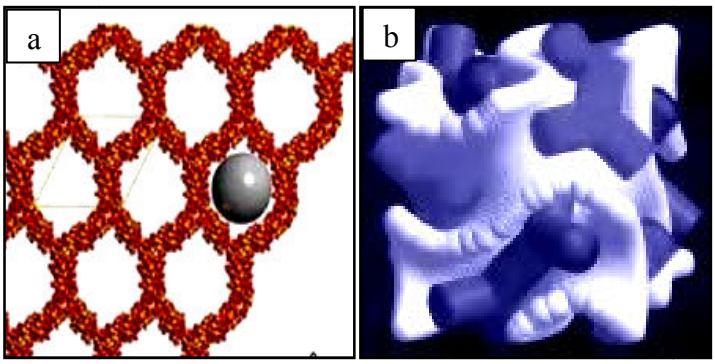

Figure 3.1: Structure of a) MCM-41[43], b) MCM-48 [44]

3.2. Folded Sheet Materials Derived From Layered Silicates

In parallel to MCM-41 studies, other Yanagisawa et all focused on mesoporous structure preparation by the reaction of layered silicates with aqueous solution of alkytrimethylammonium surfactant [45]. The progress for new mesopores material synthesis leading to current usage of layered silicates. In general, formation of perfect mesostructure primarily depends on electrostatic interactions of inorganic species and surfactant molecule, surfactant geometry, and relative concentration of surfactant [46]. Furthermore, relation between the packing parameter of structural molecules and mesostructure is responsible for the formation of these materials. The molecular packing parameter depends on the nature of the surfactant, the degree of polymerization of the silica framework, the interaction between the surfactant and the silica species. Moreover polymerization ability of silica framework and interaction between silica and surfactant influence the packing parameter*;* $g=V/a_0l$,where V is the total volume of the surfactant chains, a_0 is the effective head group area at the micelle surface, and l is the kinetic surfactant tail length [47].

3.2.1. Layered Silicates

Layered silicates are found in silicates layers form which composed of tetrahedral SiO_4 units. In tetrahedral sheets, each tetrahedrons share every three out of four oxygen [48]. Figure 2 shows various views of tetrahedral sheets.

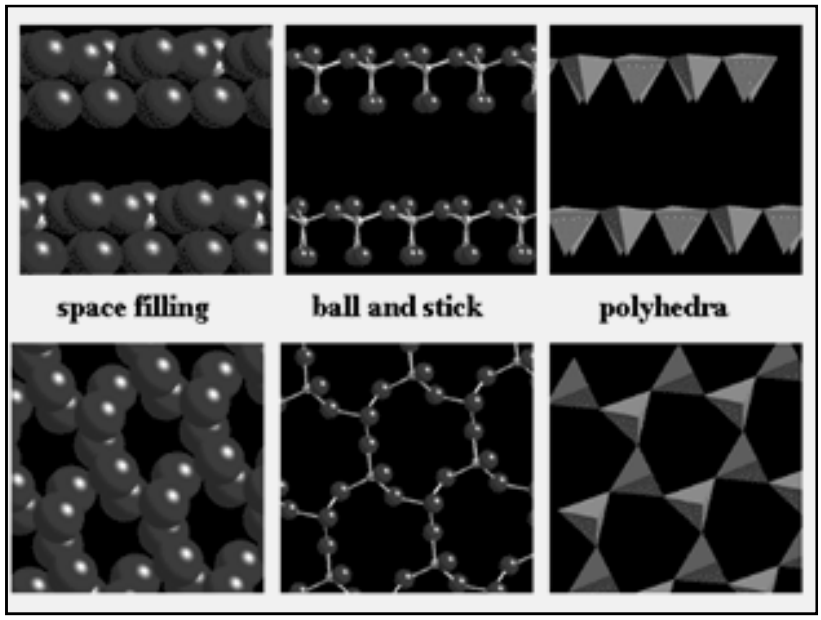

Figure 3.2: Graphical depiction of tetrahedra.

Magadiite, octosilicate, and kanemite are the major types of layered silicates. To manufacture mesoporous silicates, kanemite which is hydrated form of β and δ-$NaHSi_2O_5$ was preferred with C_nTMA surfactants. In addition to this, mesopores materials were constructed with silinaite ($NaLiSi_2O_5.3H_2O$) and $KHSi_2O_5$. But there are few reports about these layered silicates in the literature on successful synthesis. However due to structure similarity with kanemite, both of them are promising silicate source [49]. However, these layered materials are not as reactive as kanemite.

3.2.2. FSM-16

Among folded sheet materials, FSM-16 is the most common type because it possesses a large and hexagonal pore structure with highly specific surface area (1000 m^2/g). This type of materials are known with their narrow pore size distribution, however, pore diameter varies as a function of the alkyl chain length of the surfactant and synthesis conditions.

Although MCM-41 and FSM-16 are analogous, formation mechanisms of these two materials are different. Liquid crystal templating mechanism (LCT) gives the explanation of MCM-41 formation mechanism. In LCT, surfactant molecules provide a micelle/liquid crystal phase around that structure silica condense [50].

On the other hand, FSM-16 formation mechanism construct on folded sheet mechanism in which surfactant molecules exist in the layered silicate system. Unlike LCT, surfactant molecule swells and separates the layers [51].

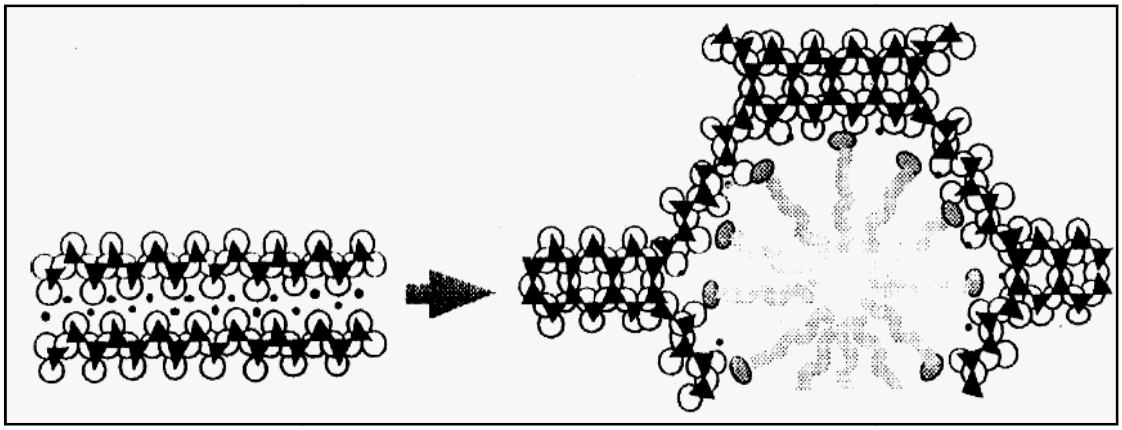

Figure 3.3: Schematic model for the formation of FSM-16 [52]

3.2.3. KSW-2

KSW-2 has squared 1D mesopores. Main components of KSW-2 are layered silicate, surfactant, a solvent and acid. Kimura et al., altered the formation of KSW-2 with rectangular arrangement of square under mild acid treatment of a layered alkyltrimethylammonium (C_nTMA)- kanemite ($NaHSi_2O_5.3H_2O$) complex.

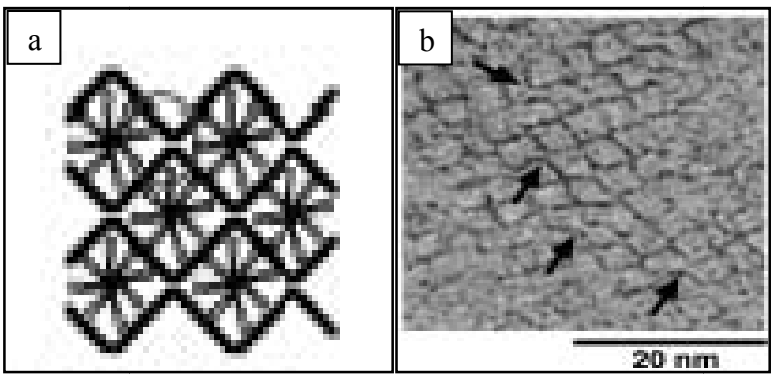

Figure 3.4: a) The schematic representation of proposed model of KSW-2 b) typical TEM image of KSW-2 [53]

3.3. Characterization Methods of Mesoporous Material FSM-16

3.3.1. X-Ray Diffraction

Powder X-ray diffraction is more frequently used for the characterization of the mesoporous materials. XRD pattern are recorded in order to detect the bulk structure of FSM-16 and dominated by the low angle peaks. High intensity and good resolution of (100) diffraction peak indicates well ordered hexagonal arrangement. Moreover, (110), (200), and (210) planes attribute to the long range order of the periodic structure [54]. The quality of the diffraction peaks change due to guest species presence within the mesopores. The intensity of the peaks decreases because guest species change the long range of the FSM-16.

3.3.2. N_2 Physisorption

N_2 physisorption provides an information about surface area, pore size, and pore size distribution. In combination with XRD data offers an estimate of the pore wall thickness. Accurate characterization of these properties is important for the structural improvement as well as optimizing the application field. Rather detailed information about surface area and pore architecture (pore diameter, pore volume, and pore size distribution) provides a powerful technique for determining the accessibility of active sites and thus is related to the catalytic activity.

Physical adsorption is one of the methods for the porous materials characterization. According to IUPAC classifications, mesoporous materials are classified by reversible type IV with H4 hysteresis loop [55]. Physisorption process of mesoporous materials includes three steps: monolayer adsorption, multilayer adsorption and capillary condensation. Monolayer adsorption occurs when all adsorbed molecules directly contact with surface area. In multilayer adsorption the adsorption space accommodate another layers, however, all molecules does not have direct contact with surface. In capillary condensation, the remaining adsorption sites after multilayered adsorption has occurred are filled with condensate and this part separated from the gas phase by menisci. Ghattas [56] stated well defined step at P/P_0 0.27-0.48 for FSM-16, representing the capillary condensation of N_2 gas and uniformity of the pores.

3.3.3. Electron Microscopy

Transmission Electron Microscopy (TEM) is the complementary characterization method of XRD and N_2 Physisorption. Because of pore size distribution plays a key role for advance applications of mesoporous molecular sieves, TEM offers direct visualization of hexagonal arrangement and pore openings.

Scanning Electron Microscopy (SEM) coupled with energy dispersive X-ray analysis allows understanding the morphology and identification and quantification of elemental composition.

3.3.4. ^{29}Si-NMR

Magnetic angle spinning (MAS) ^{29}Si-NMR is widely used as a characterization method of molecular sieves. ^{29}Si-NMR spectra gives typical two peaks at 100 and -110 ppm corresponding to Q^3 [$Si(OSi)_3OH$) and Q^4 [$Si(OSi)_4$]. Ratio of Q^3/ Q^4 refers the degree of polymerization of silica. The ratio decreases with calcination.

3.4. Studies from Literature about Catalytic Materials

Catalyst plays significant role in resulting nanotube growth because carbon bond to catalyst surface. At this point, hydrocarbon molecule has been adsorbate in order to transfer an amount of its electron density to the catalyst. Generally, catalyst non-occupied orbital's combined with anti-bonding orbitals of adsorbate molecule. Hydrocarbon molecules dissociate by reason of the electronic structure change of the adsorbate. Figure 3.5 show the combined electronic structure of the metal and adsorbate.

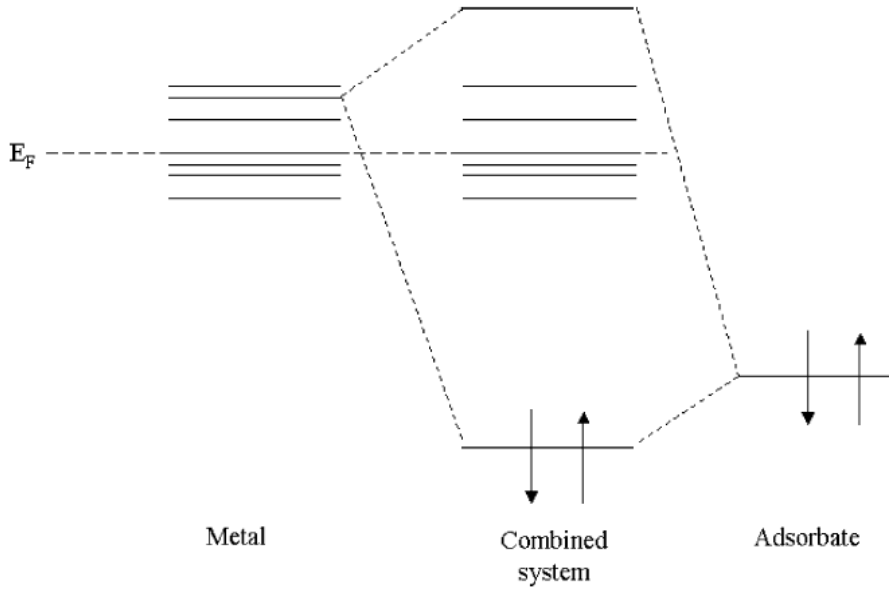

Figure 3.5: Schematic illustration of electronic interactions in chemisorption. A filled orbital on the adsorbate overlaps with an empty one on the metal [34]

Consequently, the selection of the suitable catalyst is the heart of nanotube growth. The performance of catalysis depends strongly on ability of catalyze dissociation of a hydrocarbon molecule. 3d metals have also been an attractive means of obtaining nanotube with better performance. However, the ability of adsorbate dissociation depends on,

- the center of the d-bands,
- degree of filling of the d-bands and
- the coupling matrix element between the adsorbate states and the metal d-states [57].

Fe, Ni and Co and their combination exist as a catalyst has been an attractive route for synthesis nanotubes with required properties since their 3d empty orbitals with carbon valence orbitals.

Many research groups started to focused on iron and have made remarkable progresses. Some of the current experiments results show that MWCNTs could grow on iron based catalyst. Kukovecz et al. obtained MWCNTs with Fe supported on mixtures of Al_2O_3-SiO_2 [58]. Sen et al. found iron-based catalysts concern formation of MWNTs and they also observed in the absence of any metal, monodispersed nanospheres of carbon grow instead of nanotubes [59]. Many researchers found that Fe loaded SiO_2 is a promising catalyst for MWCNTs synthesis [60-64]. Much previous work was oriented towards synthesis of MWCNTs on Fe supported silicon substrate [62, 65]. Zhao et al. [4] and Atchudan et al. [66] studied MWCNTs synthesis on Fe-MCM-41. Researchers also reported SWCNTs formation on Fe based catalysis [67-69].

There are many studies focused on Co catalyst. Different researchers applied different template for Co bases catalysis. They reported that interaction between metal particles and template affects the catalytic activity. Ago et al. [70], Klinke [62] et al., and Hernadi [60] et al. achieved to synthesize MWCNTs. On the contrary, a few paper found cobalt as a promising catalyst for SWCNTs [69, 71]. Other authors studied Ni based catalysis and mainly obtained MWCNTs [72-74].

Metal ability to form carbides and the possibility for carbon to diffuse through and over the metals has to be assessed in order to determine the catalytic activity. Therefore solubility of carbon in the metal catalyst plays important role during the formation of nanotube since high carbide content is required for the graphitic carbon nucleation [75]. Deck and his coworkers [76] performed experiments to understand why the catalytic ability of different elements varied. They stated that Fe, Co, and Ni exhibit significant carbon solubility (~0.5–1.0 wt. % carbon) in the solid solution within the temperature range between 800–900 ^oC. When these metals are used as catalyst, resulting in Fe_3C, Co_3C, Co_2C, and Ni_3C. These carbides were also compared in terms of catalytic activity. It indicated that catalytic activity for carbon nanotube growth rate was on the order of Ni>Co>Fe [77]. Moreover, Cu, Zn, Gd, and Cd could not catalyze the nanotube formation by reason of low solubility limit over the metal. For instance, only 0.0001 wt. % carbon can be soluble over Cu at 1100 ^oC [76, 78].

However, this is not sufficient enough to realize exact mechanism. The unfilled 3d-metal orbitals of Fe, Co, Ni have effect on both graphitization and growth process. Therefore, in addition to metastable carbide, electronic structure of the metal is also a key factor for dissociation of a hydrocarbon molecule. The other reason of amorphous carbon formation over copper catalyst is completely filled 3d shell [34, 79].

Among the metals; Fe, Co, and Ni are mostly used in CVD, laser ablation and arc-discharge methods for nanotube formation. However, Cr, Mn, Zn, Cd, Ti, Zr, La, Cu, V, and Gd, were able to successfully catalyze carbon nanotube's formation [76].

CHAPTER 4

4. Experimental

This chapter contains experimental processes used in this thesis work. This part covers the catalyst preparation, catalyst characterization (XRD, BET surface analysis, Si^{29}-NMR, SEM combined with energy dispersive spectroscopy) CNTs were synthesized by CVD method, and finally characterized by SEM, Raman Spectroscopy, and Thermogravimetric Analysis (TGA).

4.1. Materials

Through the FSM-16 preparation eight main components were required.

- Sodium silicate solution (27 wt. % SiO_2, 14 wt. % NaOH) from Applied Chem as a source of silica
- NaOH from Carlo Erba as a source of Na for kanemite synthesis
- Hexadecyltrimethylammonium bromide (HDTMABr, 99 % pure powder) from Merck as a source of surfactant
- Deionized water from Millipore Ultra-Pure Water System as a source of solvent
- Sulfuric acid (H_2SO_4) from Merck as a source of acid
- Nickel (III) nitrate hexahydrate ($Ni(NO_3)_3 \cdot 6H_2O$, 98 % pure) from Alfa Aesar
- Iron (III) nitrate nonahydrate ($Fe(NO_3)_3.9H_2O$, 96 % pure) from Riedel-de Haen
- Cobalt chloride hexahydrate ($CoCl_2.6H_2O$, 98 % pure) from Alfa Aesar

For CNTs experiments high purity acetylene was used as a hydrocarbon gas and high purity argon as a carrier gas.

4.2. Catalyst Preparation

In this study Fe, Co, and Ni type FSM-16 were prepared by impregnation method [56].

4.2.1. Preparation of Kanemite

For the kanemite preparation 80 ml of 0.27 M sodium hydroxide aqueous solution was added to 40 g sodium silicate solution. The mixture stirred at room temperature for 3h followed by drying at 423 K over night to remove water. The dried sample was calcined at 873K for 6h. White porous appearance δ-$Na_2Si_2O_5$ (12 g) was suspended in deionized water (120 ml) to obtain kanemite ($NaHSi_2O_5.3H_2O$) [80].

4.2.2. Synthesis of FSM-16

FSM-16 synthesis was performed with stirring 120 ml of 0.1 M HDTMABr aqueous solution with kanemite suspension at 70^oC for 3 hours. 2 M HCl aqueous solution was added dropwise to the stirred mixture to adjust pH value of the suspension to 8.5. The reaction mixture was stirred 3 hours at 70^oC then cooled to room temperature. The suspension was filtered and the paste washed with distilled water several times. The filtrates dried at 80^oC. After drying, as synthesized FSM-16 was calcined at 550^oC for 6 hours to remove the surfactant from silicate-organic complex.

4.2.3. Synthesis of Fe-FSM-16, Co-FSM-16, and Ni-FSM-16

The dried powder of as synthesized FSM-16 was impregnated with Iron (III) nitrate nonahydrate, Cobalt chloride hexahydrate, and Nickel (III) nitrate hexahydrate solutions with different metal loadings (2 and 4 wt %). Metal salt solution and as synthesized FSM-16 mixture were stirred at room temperature for 1 hour and then the excess water was removed by stirring at 70^oC. After impregnation, metal loaded catalysts were dried at 80^oC. The materials were calcinated at 550^oC for 4 hours.

4.3. Catalyst Characterization

To understand the structure of the FSM-16 materials and chemical nature of the host species, combination of characterization techniques were used. X-ray diffraction measurements (XRD), ^{29}Si-NMR, surface analysis tests, and scanning electron microscopy (SEM) are necessary to prove how metal species affect the FSM-16 structure.

4.3.1. X-ray Diffraction Measurements (XRD)

X-ray diffraction pattern were recorded with a Bruker AXS advance powder diffractometer equipped with a Siemens X-ray gun and Bruker AXS Diffrac PLUS software, using Cu Ka radiation (k = 1.5418 Angstrom). All samples scanned from 2θ = 2^o to 10^o and 2θ =10^o to 90^o.

4.3.2. NMR Measurements

Structural properties of the resultant samples were studied with ^{29}Si-NMR an Inova 500 MHz NMR Varian spectrophotometer.

4.3.3. Surface Analysis Tests

Specific surface areas, pore diameters and pore volume was determined by Quantachrome NOVA 2200 series Surface Analyzer. The nitrogen adsorption/desorption isotherms were recorded at 77 K. Prior to physisorption measurements, the samples were outgassed at 423K for 4h. The specific surface area was calculated from the BET equation in the relative pressure range of between 0.05 and 0.3 depending on number of appropriate points for linear fitting. Pore size distributions were determined using BJH method.

4.3.4. Scanning Electron Microscopy (SEM)

Morphological characterization of samples were performed using the a Gemini scanning electron microscope equipped with Leo 32 Supra 35VP field emission scanning system and electron dispersive spectrometer. An accelerating voltage between 2-5 kV was used during the measurements.

4.4. Carbon Nanotube Production

Carbon nanotube production was performed by using CVD system is depicted in Figure 4.1. The synthesized catalyst system was placed into a quartz tube (~900 mm in length, 30 mm diameter). Crucible onto which accommodate the catalyst were placed in the middle of the tube furnace in order to ensure the isothermal conditions. First the furnace was set to 300 ^{o}C before CNTs growth. At this temperature, the system was purged with 1000 ml/min Ar for 30 minutes in order to stabilize the catalyst and have a clean atmosphere. Afterwards, the system was set to desire temperature for CNTs growth and then acetylene and 1200 ml/min Ar were introduced into the system. The growth was restricted with 30 min for all experiments. The samples were cooled down to room temperature in Ar atmosphere (1000 ml/min) after the growth.

Throughout the CNTs synthesis 4 control parameters were studied.

1. Temperature (500-800^{o}C)
2. Metal type (Fe, Co, Ni)
3. Metal amount (2 % wt and 4 % wt)
4. Acetylene flow rate (between 40 ml/min-120 ml/min).

All the growth conditions are listed in the Table 4.1, Table 4.2.

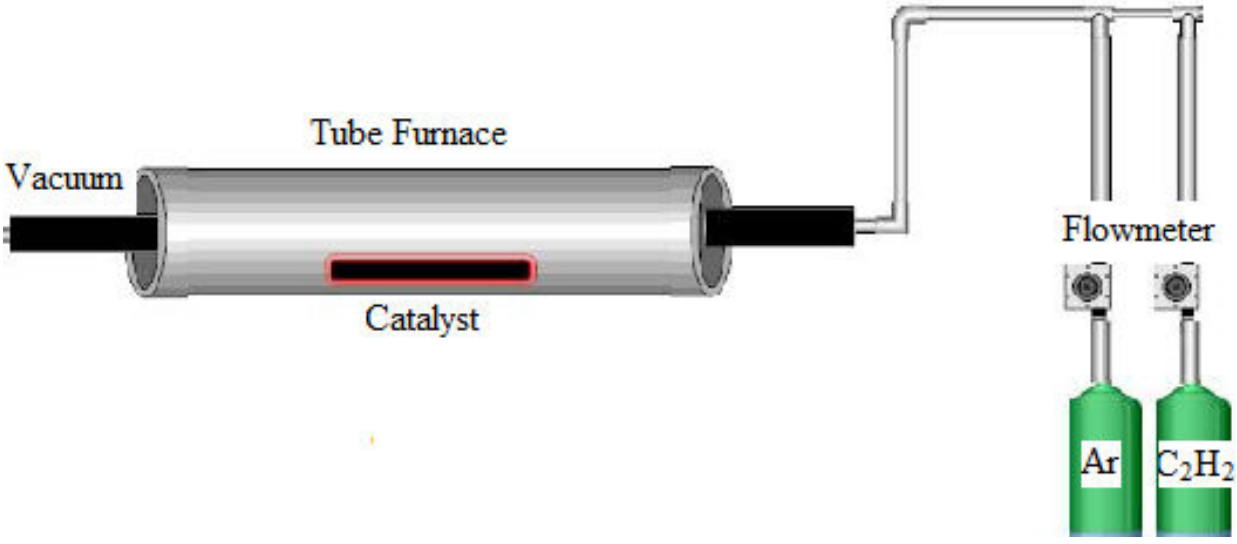

Figure 4.1: CVD set-up for CNTs production

4.5. Carbon Nanotube Characterization

Different characterization techniques were carried out to examine the CNTs growth on catalyst particles was examined with SEM to measure the diameter and uniformity of carbon nanotubes, Thermogravimetric Analysis (TGA), and Raman Spectroscopy were also used to recognize the crystallinity and the quality of CNTs as well as amount of defects. Raman spectra of CNT samples were recorded on a Renishaw InVia Reflex Raman Microscopy System (Renishaw Plc.; New Mills, Wotton-under-Edge Gloucestershire, UK) with a 514 nm argon ion laser in the range of 100 to 3200 cm^{-1}. TGA measurements were performed on a Netzsch STA 449 C Jupiter differential thermogravimetric analyzer (precision of temperature measurement $\pm 2^{o}C$, microbalance sensitivity <5 μg) under air atmosphere with a flow rate 50 ml/min, at a linear heating rate of $5^{o}C$/min.

Carbon nanotube yield based on deposition on catalyst was calculated as,

Carbon Deposition = m_{Total}- $m_{Catalyst}$

Carbon conversion was calculated as,

$$\text{Carbon Conversion} = \frac{m_{Total} - m_{Catalyst}}{Flowrate(l/\min) \times Time(\min) \div 22.4(l/\min) \times 24(g/mol)} \times 100$$

where m_{Total} is the weight of carbon product and catalyst; $m_{Catalyst}$ is the weight of catalyst used for CNTs growth.

Table 4.1: Experiments for CNTs production

Catalyst Type	Temperature (^{o}C)	Flow Rate of Acetylene
2 wt % Fe-FSM-16	500 ^{o}C	40 mL/min
2 wt % Co-FSM-16	500 ^{o}C	40 mL/min
2 wt % Ni-FSM-16	500 ^{o}C	40 mL/min
4 wt % Fe-FSM-16	500 ^{o}C	40 mL/min
4 wt % Co-FSM-16	500 ^{o}C	40 mL/min
4 wt % Ni-FSM-16	500 ^{o}C	40 mL/min
2 wt % Fe-FSM-16	600 ^{o}C	40 mL/min
2 wt % Co-FSM-16	600 ^{o}C	40 mL/min
2 wt % Ni-FSM-16	600 ^{o}C	40 mL/min
4 wt % Fe-FSM-16	600 ^{o}C	40 mL/min
4 wt % Co-FSM-16	600 ^{o}C	40 mL/min
4 wt % Ni-FSM-16	600 ^{o}C	40 mL/min
2 wt % Fe-FSM-16	700 ^{o}C	40 mL/min
2 wt % Co-FSM-16	700 ^{o}C	40 mL/min
2 wt % Ni-FSM-16	700 ^{o}C	40 mL/min
4 wt % Fe-FSM-16	700 ^{o}C	40 mL/min
4 wt % Co-FSM-16	700 ^{o}C	40 mL/min
4 wt % Ni-FSM-16	700 ^{o}C	40 mL/min
2 wt % Fe-FSM-16	800 ^{o}C	40 mL/min
2 wt % Co-FSM-16	800 ^{o}C	40 mL/min
2 wt % Ni-FSM-16	800 ^{o}C	40 mL/min
4 wt % Fe-FSM-16	800 ^{o}C	40 mL/min
4 wt % Co-FSM-16	800 ^{o}C	40 mL/min
4 wt % Ni-FSM-16	800 ^{o}C	40 mL/min

Table 4.2: Flow rate experiments for 4 wt % Fe-FSM-16 at 700 ^{o}C

Catalyst Type	Temperature (^{o}C)	Flow Rate of Acetylene
4 wt % Fe-FSM-16	700 ^{o}C.	40 mL/min
4 wt % Fe-FSM-16	700 ^{o}C.	60 mL/min
4 wt % Fe-FSM-16	700 ^{o}C.	80 mL/min
4 wt % Fe-FSM-16	700 ^{o}C.	100 mL/min
4 wt % Fe-FSM-16	700 ^{o}C.	120 mL/min

CHAPTER 5

5. Results and Discussion

5.1. Catalyst Characterization

FSM-16 and metal impregnated materials were analyzed by XRD, Si^{29} NMR, N_2 physisorption, SEM- EDS characterization techniques.

5.1.1. XRD Analysis

Figure 5.1 shows the XRD pattern of the kanemite. It was found that kanemite with high crystallinity was successfully synthesized and X-ray pattern identical to those in pervious works [81]. Additionally, it should be noted that X-ray diffraction peaks belonging to α-$Na_2Si_2O_5$ (27°), β-$Na_2Si_2O_5$ (30° and 37°), and δ-$Na_2Si_2O_5$ (22.4° and 37°) (Fig 5.1).

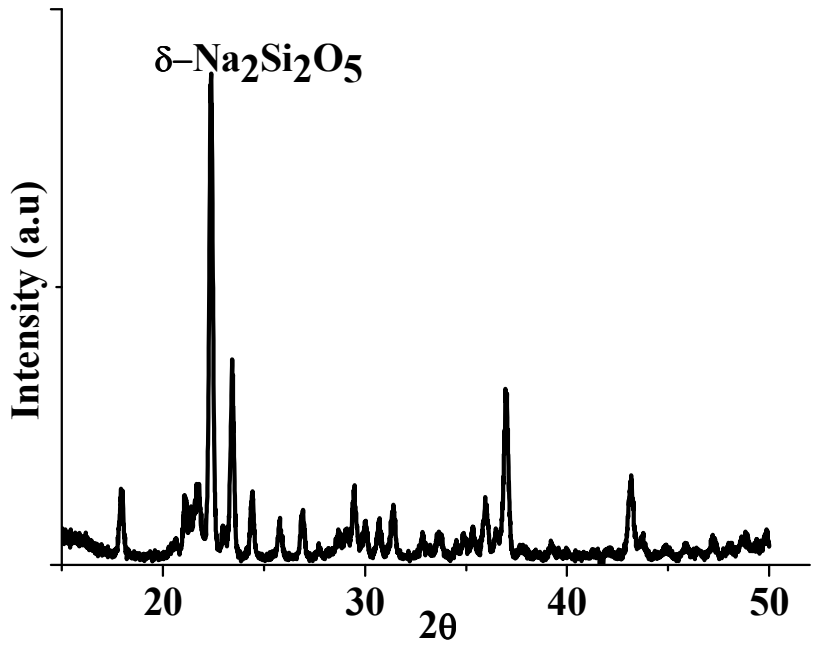

Figure 5.1: XRD pattern of kanemite

Powder X-ray diffraction is an important characterization method for the mesoporous materials. XRD pattern of the FSM-16 samples were recorded in order to detect the changes in bulk structure due to guest species presence within the mesopores. The low angle XRD pattern of FSM-16 and Fe, Co, and Ni containing FSM-16 are shown in Figure 5.2, and 5.3. Three diffraction peaks corresponding to (100), (110), and (200) planes, indicated well ordered hexagonal arrangement, were observed. FSM-16 exhibited high intensity and good resolution of (100), (110), and (200) diffraction peaks [54]. The quality of the peaks attributed to the long range order of the periodic structure. It was found that metal impregnation had significant effect on the intensity of the reflection peaks. The intensity decreased due to introduction of metal into mesopores. This behavior was the result of scattering difference from pore wall and pore region [82]. Therefore, the high metal amount was expected to cause increase the degree of phase cancellation between pore and framework wall. When 4 wt % Ni and 4 wt % Co were impregnated on FSM-16, the resultant catalyst did not completely vanish the long range order. On the other hand, considerable decrease in the (110), and (200) reflection peaks was observed for 4 wt % Fe modified FSM-16. It was noted that, higher Fe content led to broad (100) peak. These finding implies that Fe probably deteriorated the periodic structure due to apparent change of Si-O-Si bond angle by Fe ions compared to Ni and Co.

In fact, no additional peaks belong to metal oxide was observed in the higher 2θ range. The same behavior was observed for cobalt nitrate impregnated FSM-16 [56] , nickel and copper oxide impregnated MCM-48 [83]. Only, 4 wt % Fe exhibited Fe_2O_3 reflection peaks. This result indicated that metal species exhibited high dispersion inside the pores and no crystalline metal particles formed ouside the pores.

Moreover, metal impregnation is known to has effects on average unit cell parameter. Mainly, lattice parameter was calculated from

$$a = \frac{2}{\sqrt{3}} d_{(100)}$$

The general observation is metal incorporation into silica framework significantly extent the α_0 parameter. Table 5.1 indicates the variation of unit cell parameter with metal impregnation. It was concluded that unit cell parameter extent from 4.00 nm up to 4.50 nm with metal impregnation. These can be regarded as the reason of metal

incorparation into siliconeous matrix. However, the unit cell parameter did not significantly increase with 4 wt % Co impregnation. This behavior attribute to more cobalt ions prefer to situated at the Si-OH matrix compared to those for Fe and Ni [56].

Table 5.1: d_{100} and *a* values for catalysts

Sample	d_{100}	*a*
FSM-16	3.46	4.00
4 % Fe-FSM-16	3.77	4.35
4 % Co-FSM-16	3.59	4.15
4 % Ni-FSM-16	3.90	4.50
2 % Fe-FSM-16	3.82	4.41
2% Co-FSM-16	3.77	4.35
2 % Ni-FSM-16	3.77	4.35

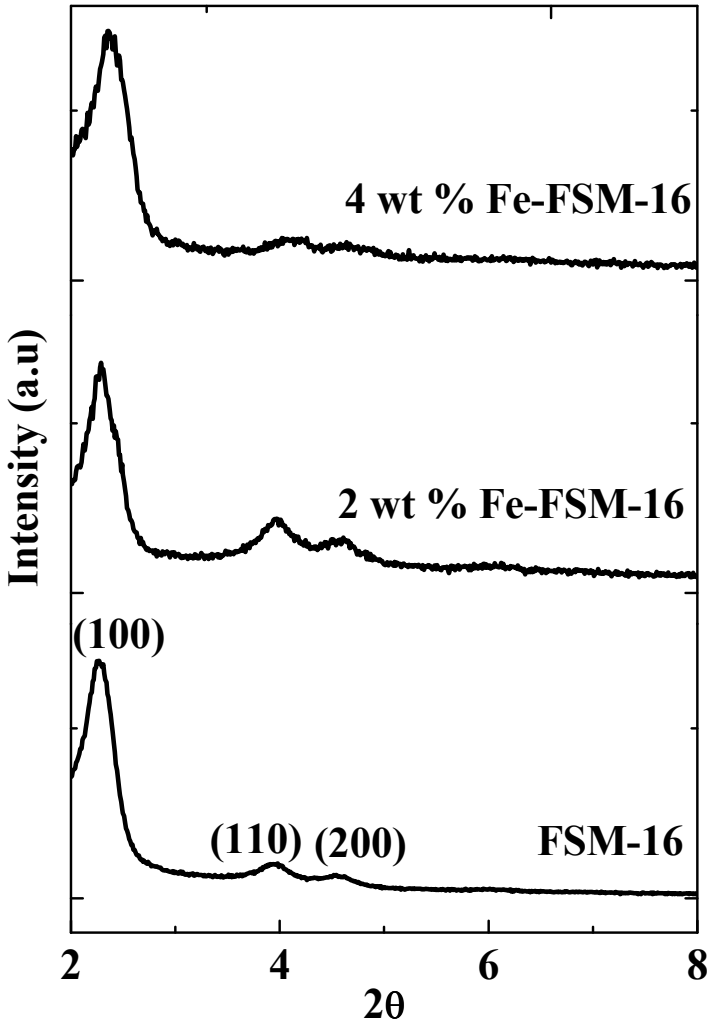

Figure 5.2: XRD pattern of FSM-16 and Fe impregnated FSM-16

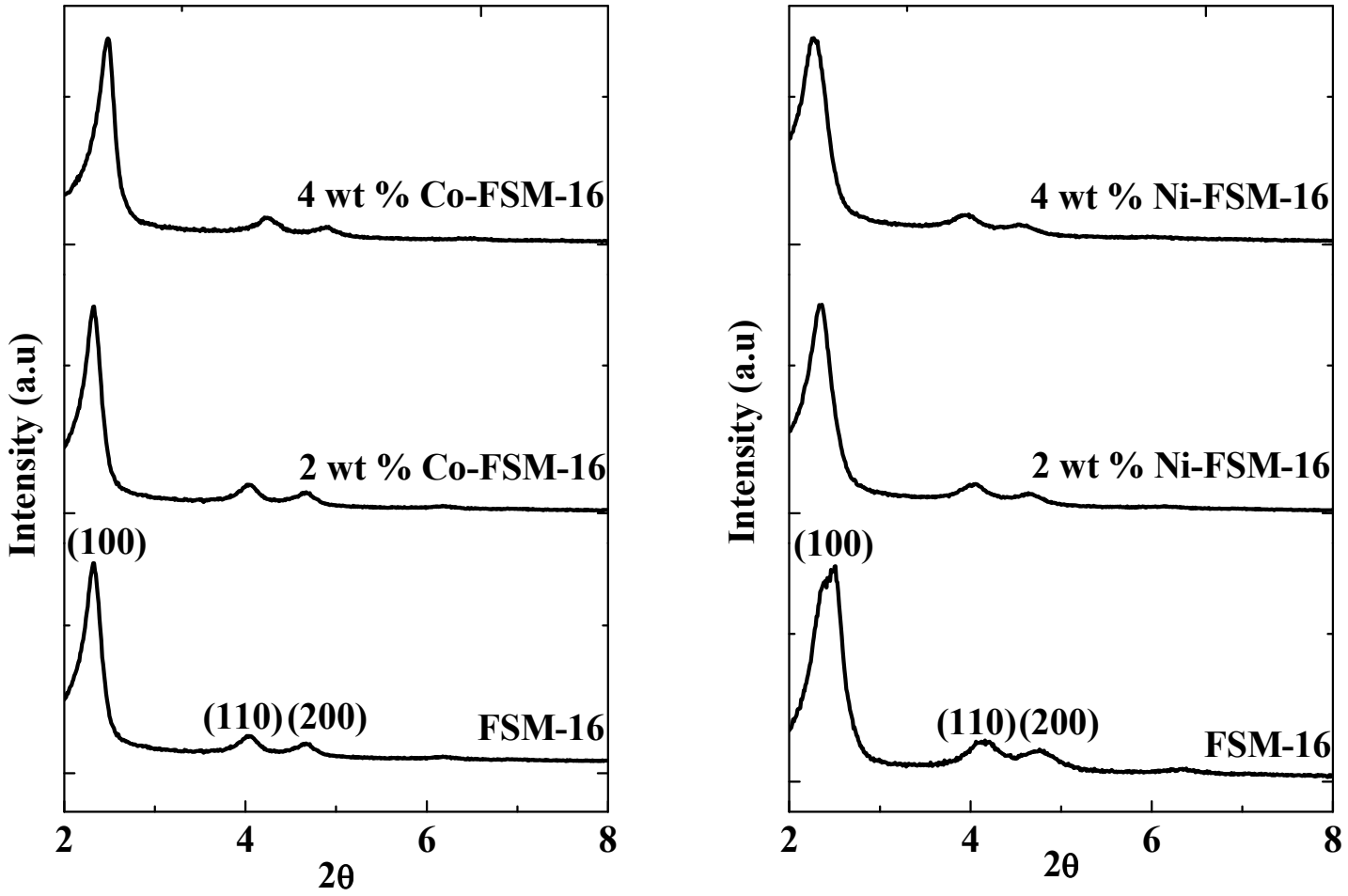

Figure 5.3: XRD pattern of FSM-16, Co and Ni impregnated FSM-16

5.1.2. ^{29}Si-NMR Analysis

^{29}Si-NMR is the choice to characterize FSM-16 and it provides structural information about silicate framework. In general, as synthesis FSM-16 shows three ^{29}Si NMR peaks correspond to Q^2 [Si*$(OSi)_2(OH)_2$], Q^3[Si*$(OSi)_3(OH)$] and Q^4 [Si*$(OSi)_4$] silicon species [54, 84]. The Q^n silicate species are expressed as $Si(OSi)_n,(OH)_{4-n}$, and *n* is a measure of the degree of condensation of the silicate. The ^{29}Si-NMR spectra of as synthesized FSM-16 and calcinated FSM-16 is shown in Figure 5.4. As synthesized FSM-16 consisted of three resonances at -90 ppm, -100 ppm, and -109 ppm corresponds to Q^2, Q^3, and Q^4 in geminal silanol [Si*$(OSi)_2(OH)_2$], silanol [Si*$(OSi)_3(OH)$], and siloxane [Si*$(OSi)_4$] groups, respectively. After calcination, Q^4 sites increased, a broadened Q^4 signal with small Q^3 signal was observed in NMR spectrum. Calcination increased the Si-O-Si network by partial condensation of Si-OH groups. Moreover, absence of Q^2 signal pointed high degree of condensation.

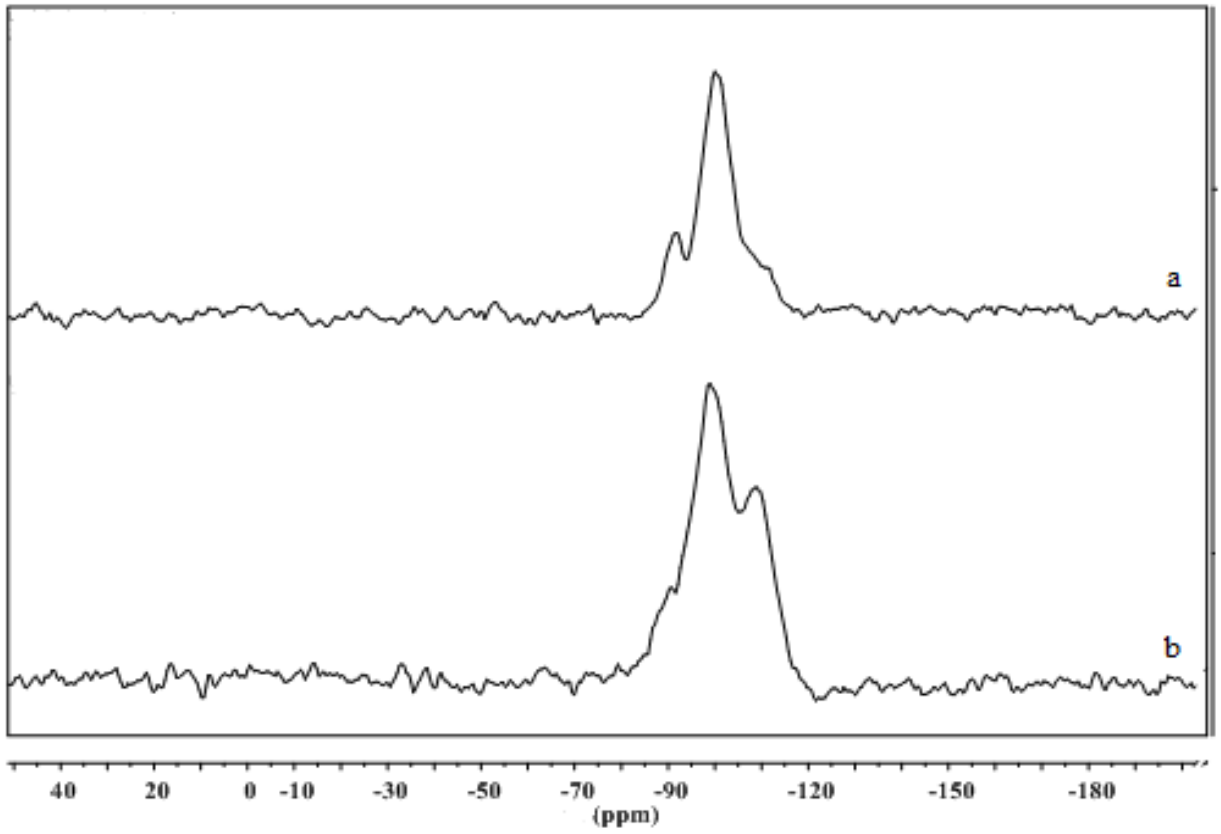

Figure 5.4: NMR spectra of a) FSM-16 after calcination,b) FSM-16 before calcination

^{29}Si-NMR spectra of metal impregnated FSM-16 mesoporous materials are illustrated in Figure 5.5. Metal impregnation caused decrease in Q^3 signal. As the concentration of

metal amount increased, intensity of silanol group decreased and became absence. Only 2 wt % Co-FSM-16, 4 wt % Co-FSM-16, and 2 wt % Fe-FSM-16 exhibited Q^4 signal with small-shoulder Q^3 signal. This proved that there was interaction between metal ions and hydroxyl groups. Moreover, Chao et al. [85] reported remarkable decrease in Q^3 intensity of vanadium-substituted MCM-41. They found that substitution of vanadium into MCM-41 promoted vanadium ions and hydroxyl group's interactions and resulted decrease in the number of Si-OH species.

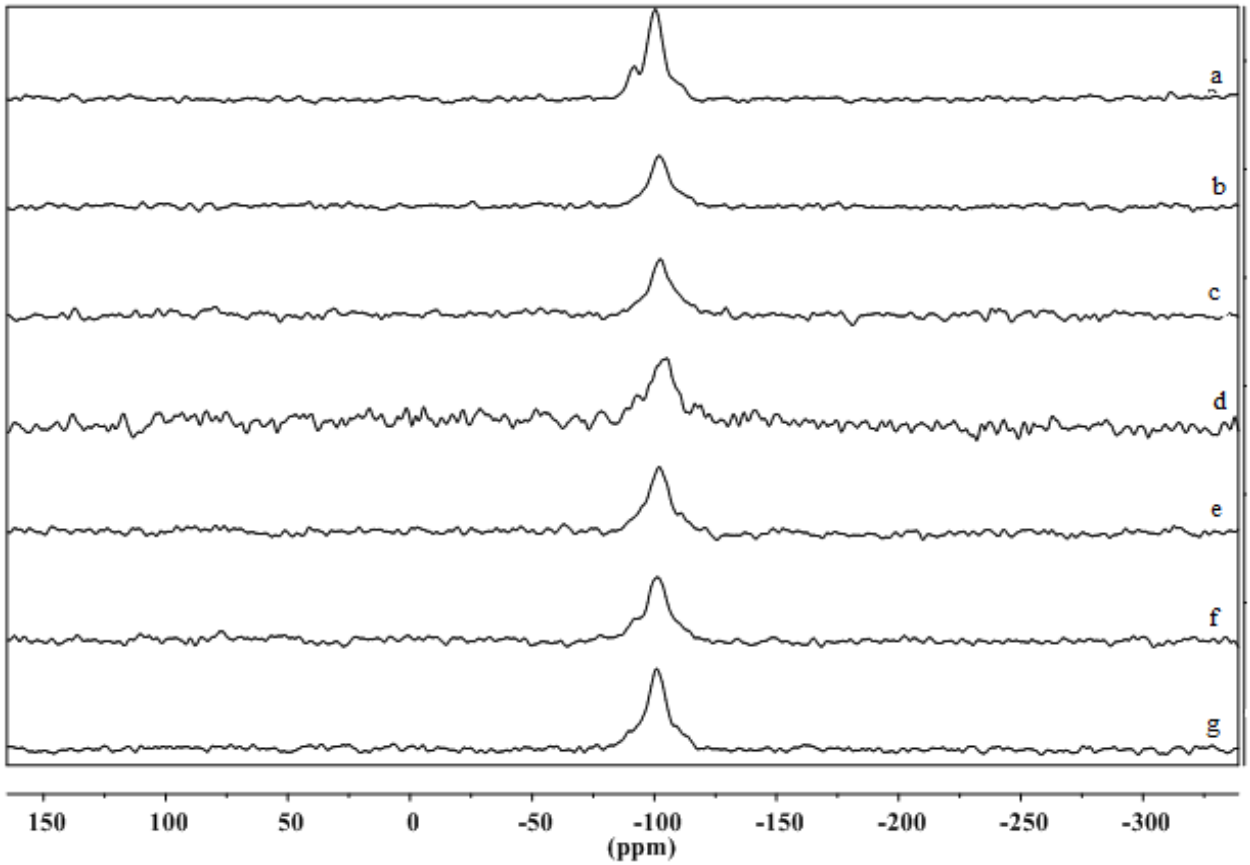

Figure 5.5: ^{29}Si NMR spectra for (a) FSM-16, (b) 2 wt % Ni-FSM-16, (c) 4 wt % Ni-FSM-16, (d) 2 wt % Fe-FSM-16, (e) 4 wt % Fe-FSM-16, (f) 2 wt % Co-FSM-16, (g) 4 wt % Co FSM-16

5.1.3. N_2 Physisorption Analysis

N_2 adsorption measurements are necessary for evaluation of porosity. Therefore, BET and BJH is preferred method for specific surface area, pore size distribution and pore volume estimations. Table 5.2 demonstrates specific surface areas, pore size distributions and pore volumes of samples.

Table 5.2: Results of specific surface area, pore size and pore volume of samples

Sample	Specific Surface Area (m^2/g)	Average Pore Size (nm)	Total Pore Volume (cc/g)
FSM-16	755.1	3.6	1.43
2 wt % Fe- FSM-16	591.1	2.61	0.633
4 wt % Fe- FSM-16	581.5	2.46	0.548
2 wt % Co- FSM-16	608.1	2.62	0.779
4 wt % Co- FSM-16	607.3	2.46	0.688
2 wt % Ni- FSM-16	625.4	2.63	0.785
4 wt % Ni- FSM-16	610.5	2.61	0.781

N_2 adsorption-desorption isotherms are depicted in Figure 5.6- Figure 5.8. All samples showed typical type IV isotherms with hysteresis loop caused by capillary condensation for mesoporous materials. Comparison on the basis of surface area, FSM-16 revealed 755.1 m^2/g, it was slightly lower than in other published works [56, 86, 87]. FSM-16 had larger surface area when compared with metal impregnated samples. It was observed that increasing metal amount resulted decrease in surface area due to intrapore formation of metal oxides.

Amount of physisorbed N_2 compared for FSM-16 and metal modified FSM-16, respectively. It was concluded that, amount of physisorbed N_2 decreased with increasing metal loading. This implied that metal ion low sorption capacity was the result of metal occupancy of metal ion in the pore system. Only for 4 wt % Ni- FSM-16 exhibited slightly higher amount of N_2 adsorption than 2 wt % Ni- FSM-16.

A step increase was observed at P/P_0 between 0.3-0.5 for FSM-16 corresponding to capillary condensation. It was found that; impregnation influenced the inflection point and shifting it to lower values of P/P_0. Thus, it was expected for smaller pores. Additionally, pore diameter of samples decreased with metal impregnation. This was because of interaction between metal ions and FSM-16 framework.

Figure 5.9 and Figure 5.10 represent the pore size distribution curves of the samples. Additionally, as the Fe and Ni content increased, the intensity of pore size distribution peak decreased in which turn affect mesoporous ordering. In contrast, cobalt impregnated samples behavior was different. Peak intensity of 2 wt Co % FSM- 16 was reasonably lower than 4 wt Co % FSM-16. The reason was less cobalt ion interact with

silica framework for 4 wt Co % FSM-16. Dependence of mesoporous ordering was important to explore, thus, combined with XRD and ^{29} Si-NMR data, it could be concluded that mesoporous ordering gradually decreased with increasing amount of Fe, Co and Ni.

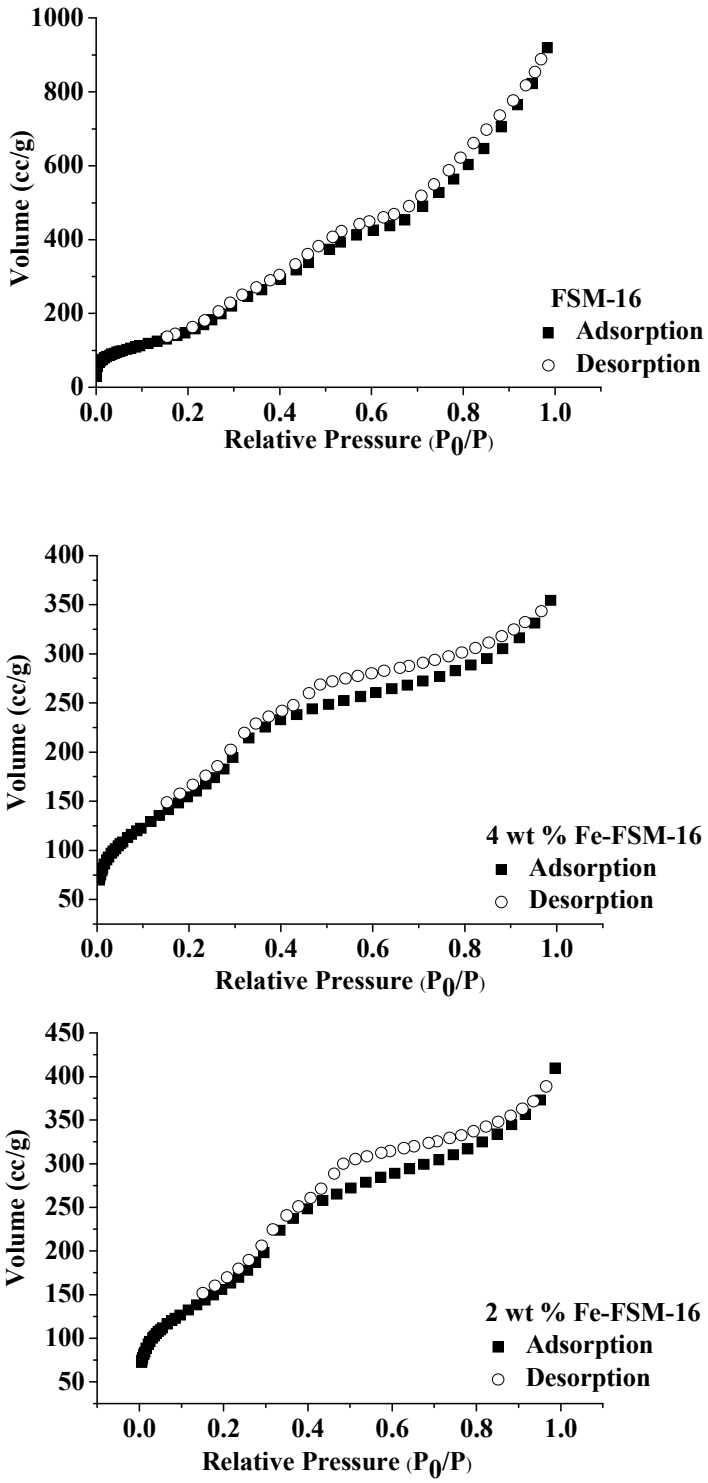

Figure 5.6: Adsorption-desorption isotherms for FSM-16 and iron modified FSM-16

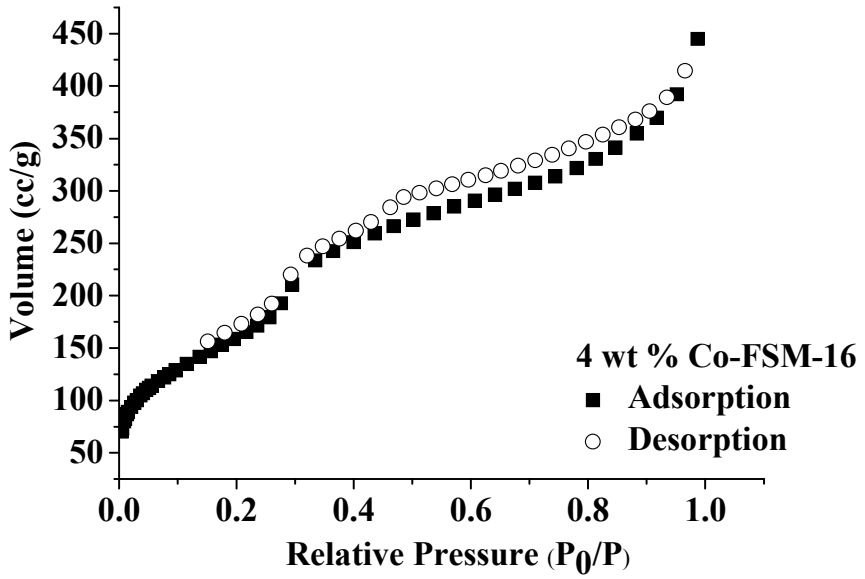

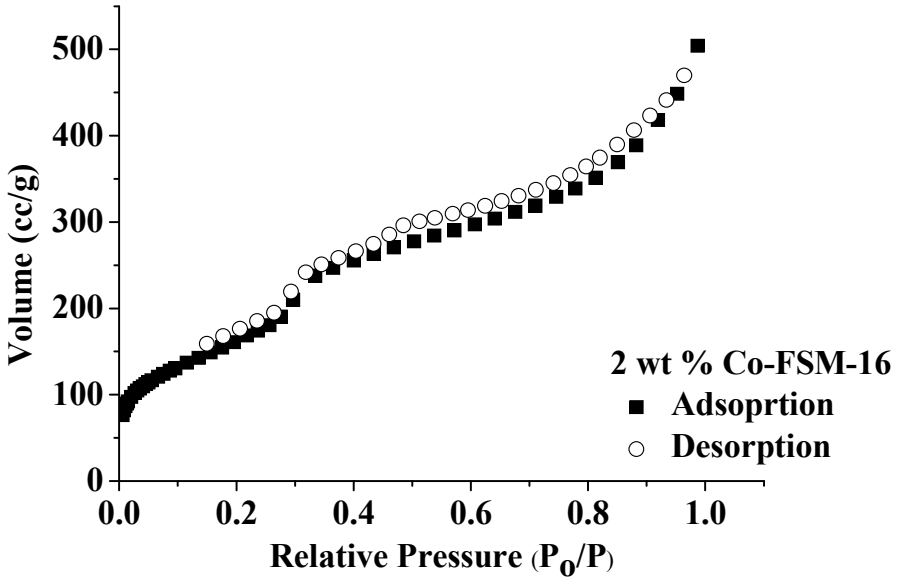

Figure 5.7: Adsorption-desorption isotherms for cobalt-modified FSM-16

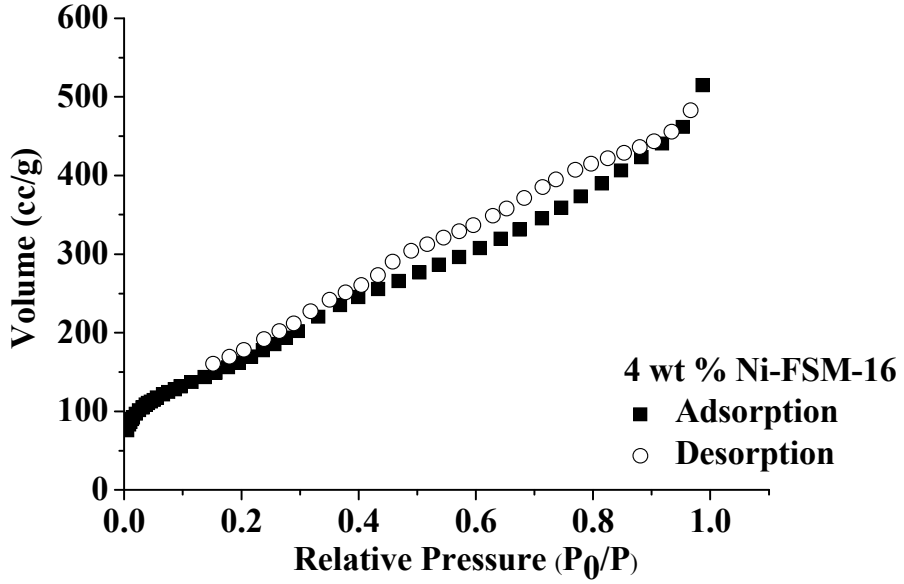

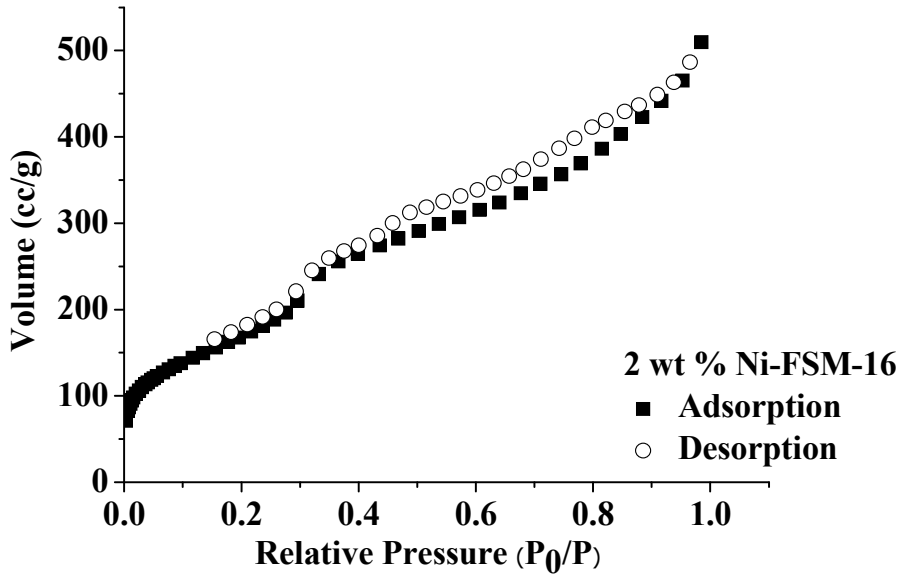

Figure 5.8: Adsorption-desorption isotherms for nickel-modified FSM-16

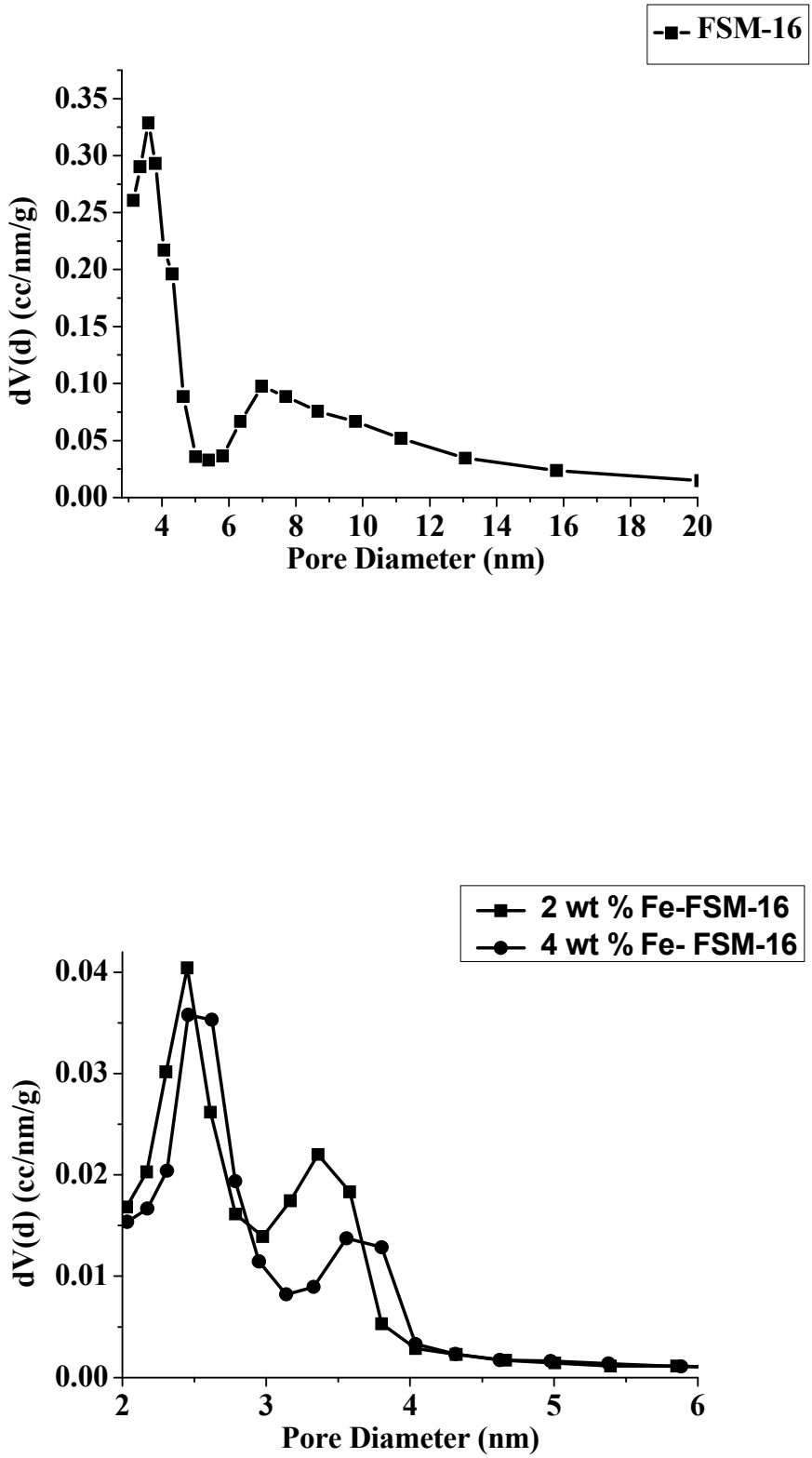

Figure 5.9: Pore size distribution of FSM-16 and Fe modified FSM-16

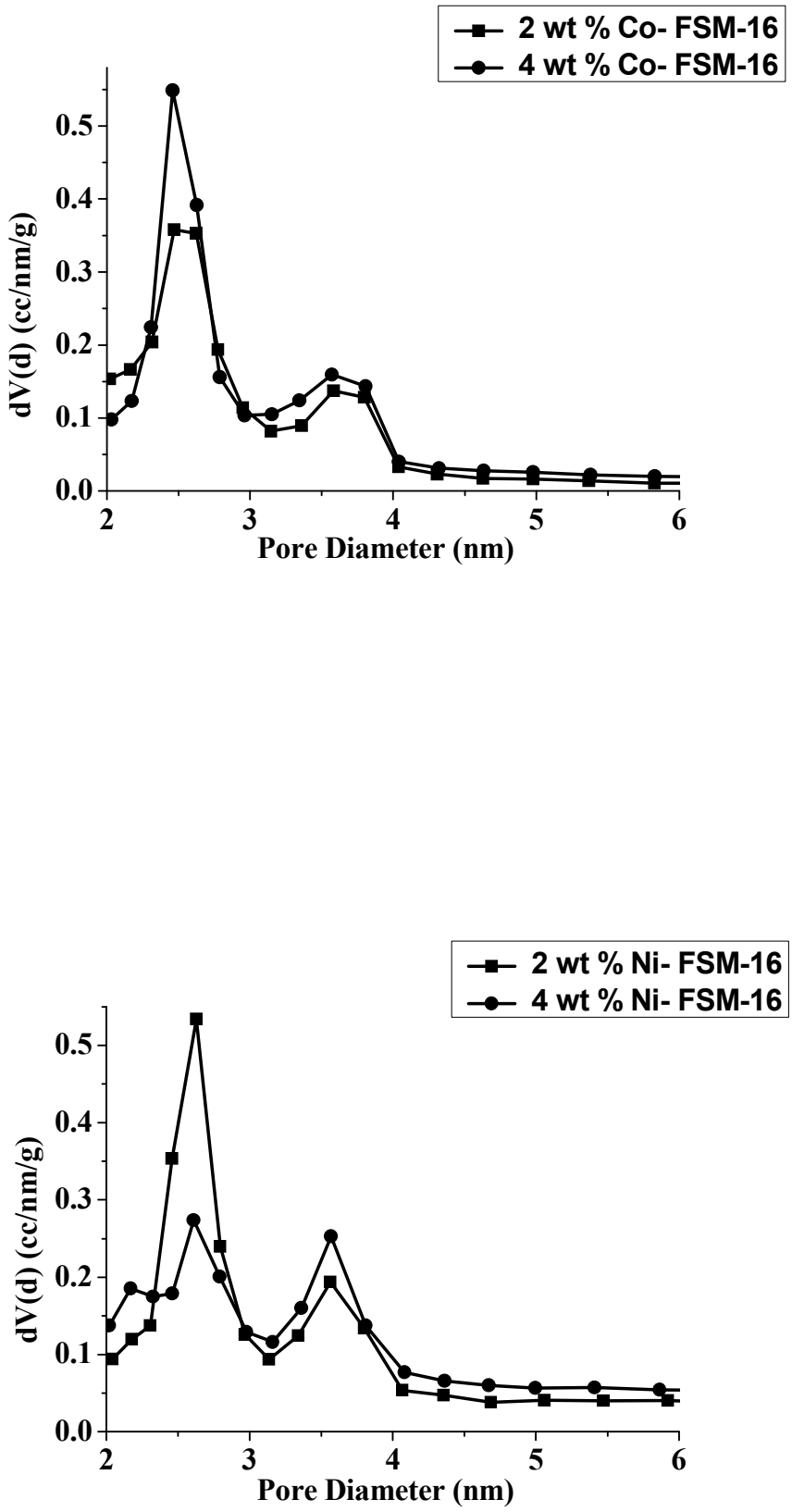

Figure 5.10: Pore size distribution of Co and Ni modified FSM-16

5.1.4. SEM-EDS Analysis

EDS measurements were performed to clarify composition of the samples. EDS results are shown in Table 5.3. EDS results indicated that the Fe, Co, and Ni were present in the silica framework. Indeed, higher weight percentage of cobalt in the silica framework was the consequence of loss of some silica during the impregnation procedure.

Table 5.3: EDS analysis of Fe, Co and Ni impregnated FSM-16

Sample	Initial Metal/FSM-16 Weight Percentage	Metal /Si Weight Percentage (EDS)
Fe- FSM-16	2	1.80
Fe- FSM-16	4	3.46
Co- FSM-16	2	2.50
Co- FSM-16	4	4.35
Ni- FSM-16	2	1.93
Ni- FSM-16	4	3.83

SEM is a method of choice to characterize the morphology of mesoporous materials. This method proved the impregnation of transition metal nanoparticles.

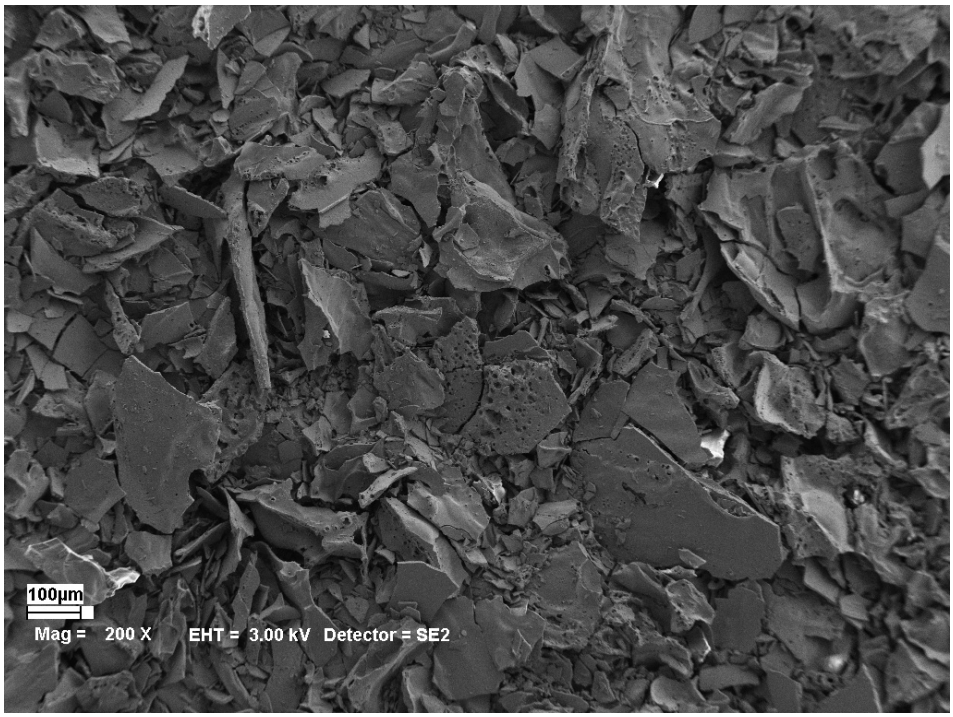

Figure 5.11: SEM images of kanemite

Figure 5.11 illustrates SEM photograph of kanemite. The SEM image of kanemite crystals clearly indicated that it had irregular plate type morphology. The morphology of FSM-16 seen in Figure 5.12 proved that FSM-16 had porous structure. The pore formation came about due to intercalation chemistry of kanemite during FSM-16 synthesis. Moreover, it was clearly seen that kanemite sheets were present in structure of FSM-16.

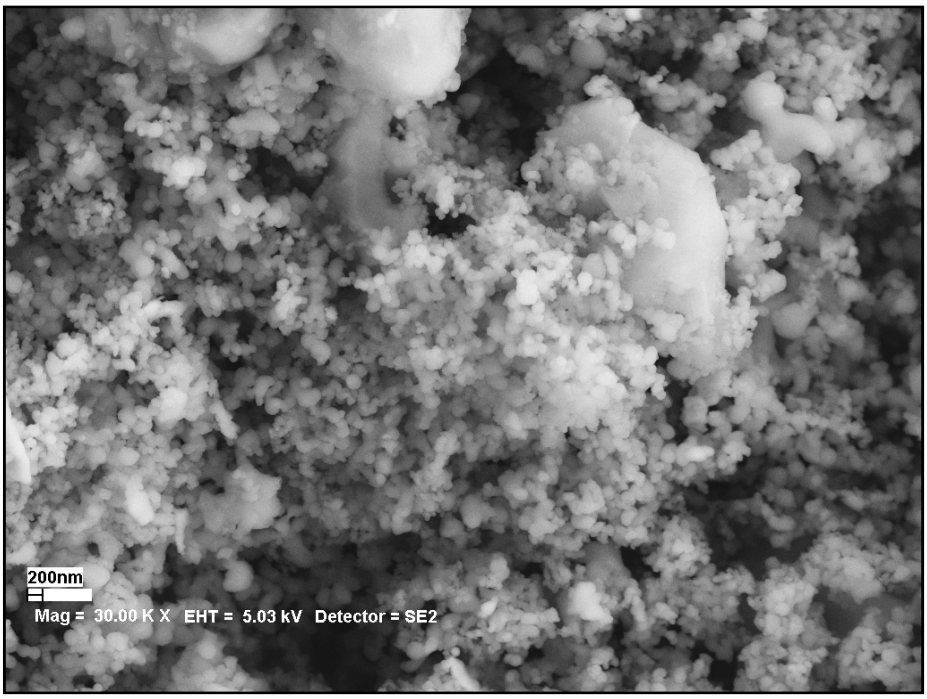

Figure 5.12: SEM images of FSM-16

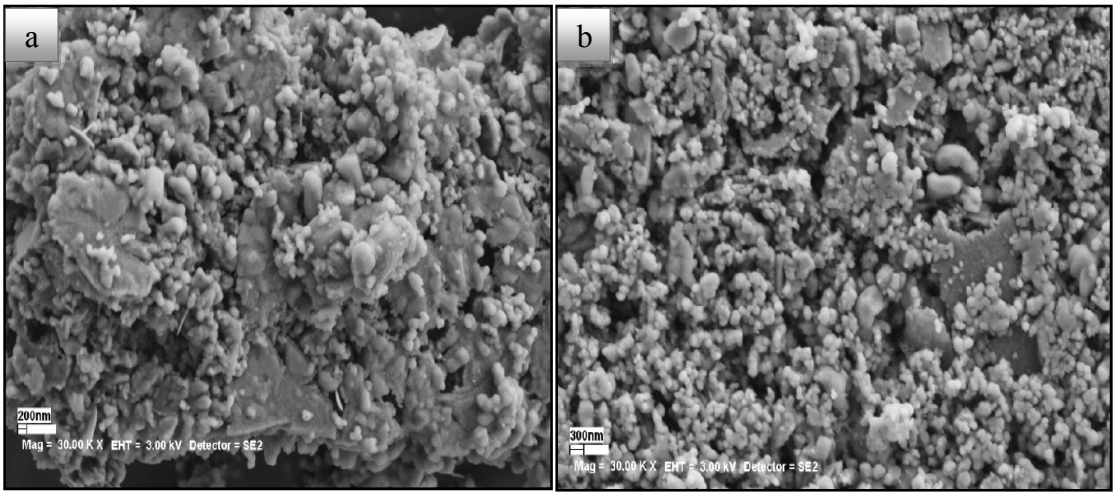

Figure 5.13: SEM images of a) 4 wt % Fe-FSM-16 and b) 2 wt % Fe-FSM-16

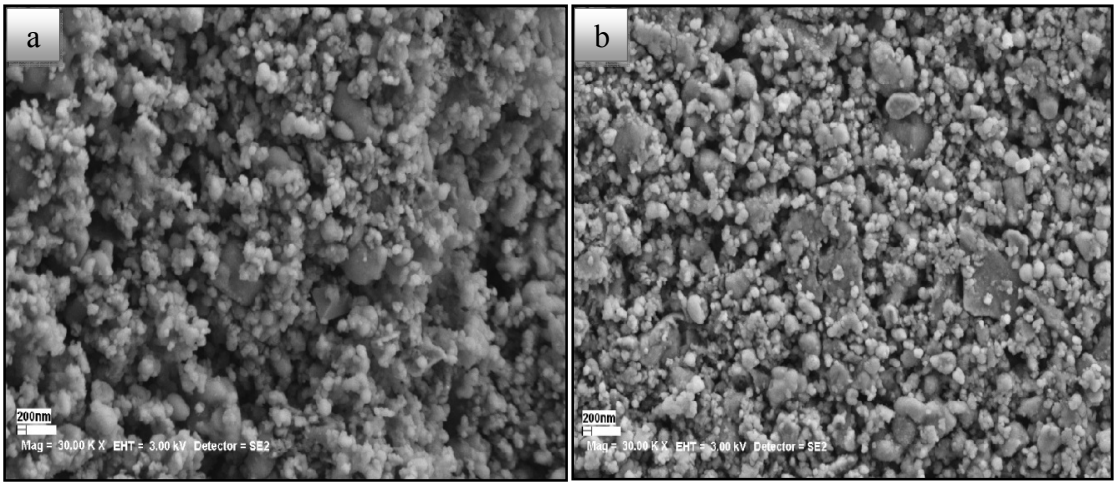

Figure 5.14: SEM images of a) 4 wt % Co-FSM-16 and b) 2 wt % Co-FSM-16

Fe, Co, and Ni impregnated FSM-16 showed similar features with FSM-16 (Fig 5.13-15). Kanemite sheets were still observable and covered with metal nanoparticles. It revealed the successful impregnation of metals. EDS results also verified these observations. From the observations, it had to be concluded that metal samples morphology was indeed not same with FSM-16. As the metal amount increased, the porous and spherical structure of FSM-16 was partially loose.

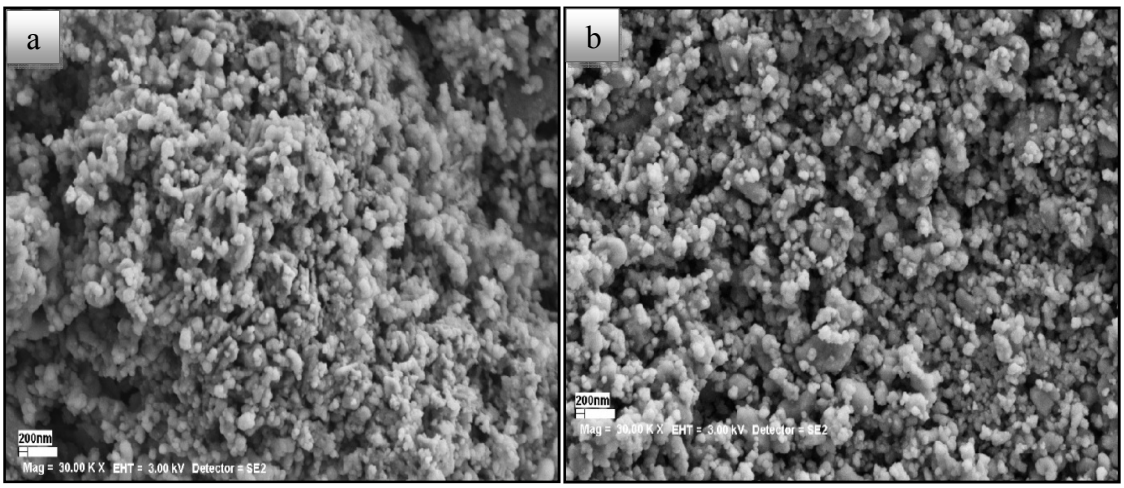

Figure 5.15: SEM images of a) 4 wt % Ni-FSM-16 and b) 2 wt % Ni-FSM-16

5.2. Carbon Nanotube Characterization

In this part different characterization techniques were used examine carbon nanotube growth on catalyst; namely SEM, Raman Spectroscopy, and Thermogravimetric Analysis (TGA).

5.2.1. Effect of Catalyst

Initially, carbon nanotube growth of 2 wt % Fe,Co,Ni- FSM-16 and 4 wt % Fe,Co,Ni-FSM-16 were carried out under using CVD of acetylene –argon atmosphere for 30 min at 700 ^{o}C. The experiments were performed with using different catalysts keeping all other parameters constant in order to understand metal type and amount effect. The morphology of CNTs growth varied at constant temperature and acetylene flow rate which is shown in Figure 5.13-5.15. SEM images show that CNTs formation occurred under acetylene flow at this temperature. Moreover, CNTs growth on Fe, Co, and Ni-FSM-16 were different. It was found that metal type had a considerable effect on CNTs growth. For Fe catalyzed CNTs related image depicted in Figure 5.16, thicker and longer CNTs growth was observed on catalyst. Diameter of CNTs growth over Fe modified FSM-16 changed between 15-40 nm. On the other hand, Ni and Co catalyzed CNTs images depicted in Figure 5.17 and Figure 5.18 had smaller (10-20 nm) and narrower diameter distribution compared with Fe catalyst.

Table 5.4: The yield of carbon deposition at 700^{o}C

Catalyst	Weight of catalyst before reaction (mg)	Weight of catalyst after reaction (mg)	Carbon Deposition (mg)	Carbon Conversion (%)
4 wt % Fe-FSM-16	100.3	170.0	69.7	5.46
2 wt % Fe-FSM-16	100.4	171.1	70.7	5.49
4 wt % Co-FSM-16	100.5	146.7	46.2	3.60
2 wt % Co-FSM-16	100.6	170.3	69.7	5.42
4 wt % Ni-FSM-16	100.2	140.1	39.9	3.10
2 wt % Ni-FSM-16	100.0	155.0	55.0	4.28

Obviously, catalyst particles initiated the CNTs growth and tube diameters strongly depended on particle size. Moreover, mobility of metal particles along the surface of the

support was critical, tube diameters were also found to be governed by the mobility of particle.

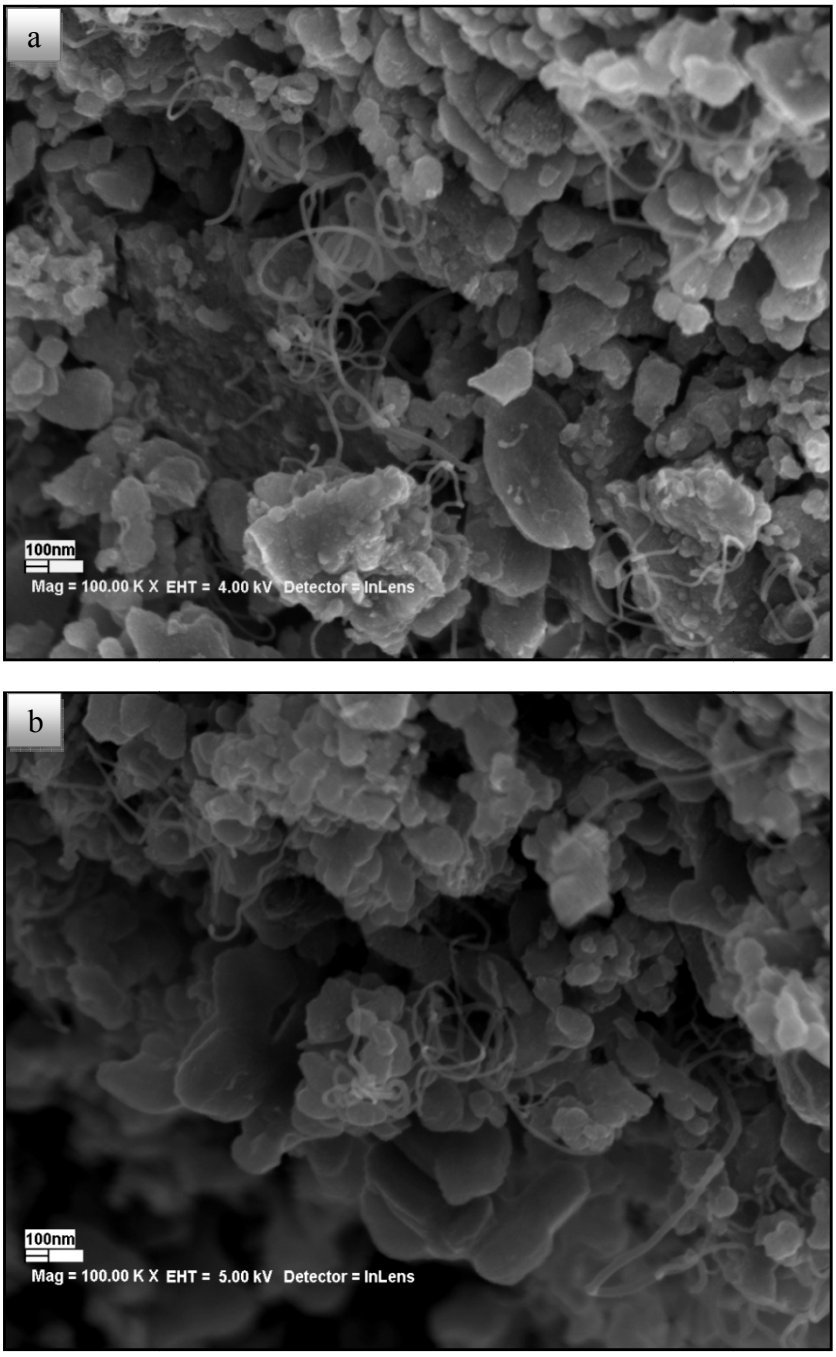

Figure 5.16: A set of SEM micrographs of Fe catalyzed CNTs: a) 2 wt % Fe-FSM-16, b) 4 wt % Fe- FSM-16

As the metal amount was increased from 2 wt % to 4 wt % no significant change was observed for Fe catalyzed reactions. However, weight percentage increase of the Co and Ni metals affected the particle mobility as well as mean particle size. Therefore, CNTs

diameter became larger. Mobility was critical because metal particles started agglomeration. Size of the metal nanoclusters changed. Therefore, agglomerated metal particles resulted in CNTs with large diameters. When these two parameters were taken into account, SEM images rationalized the effective catalyst particle size was larger for Fe catalyst compared with Ni and Co.

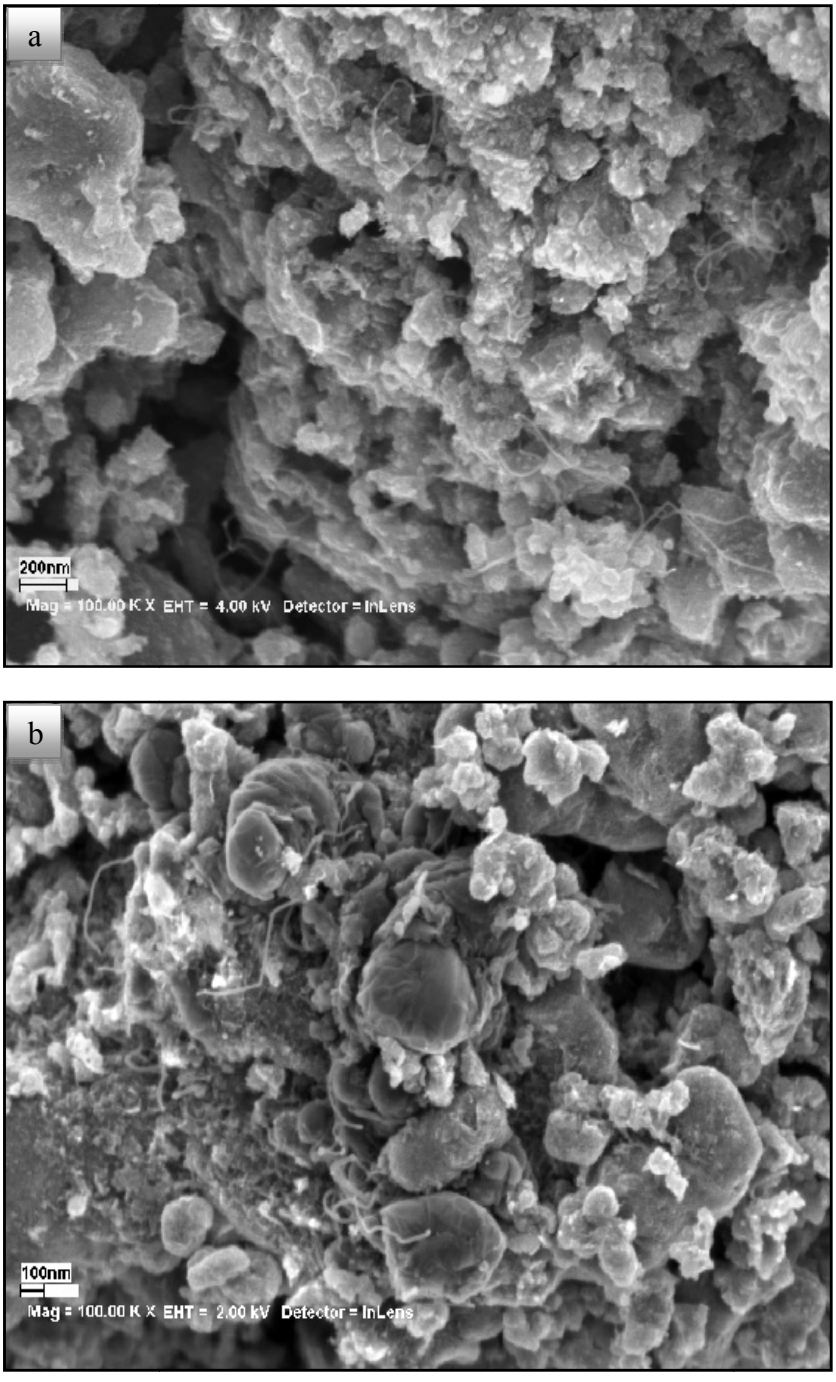

Figure 5.17: A set of SEM micrographs of Co catalyzed CNTs: a) 2 wt % Co-FSM-16, b) 4 wt % Co- FSM-16

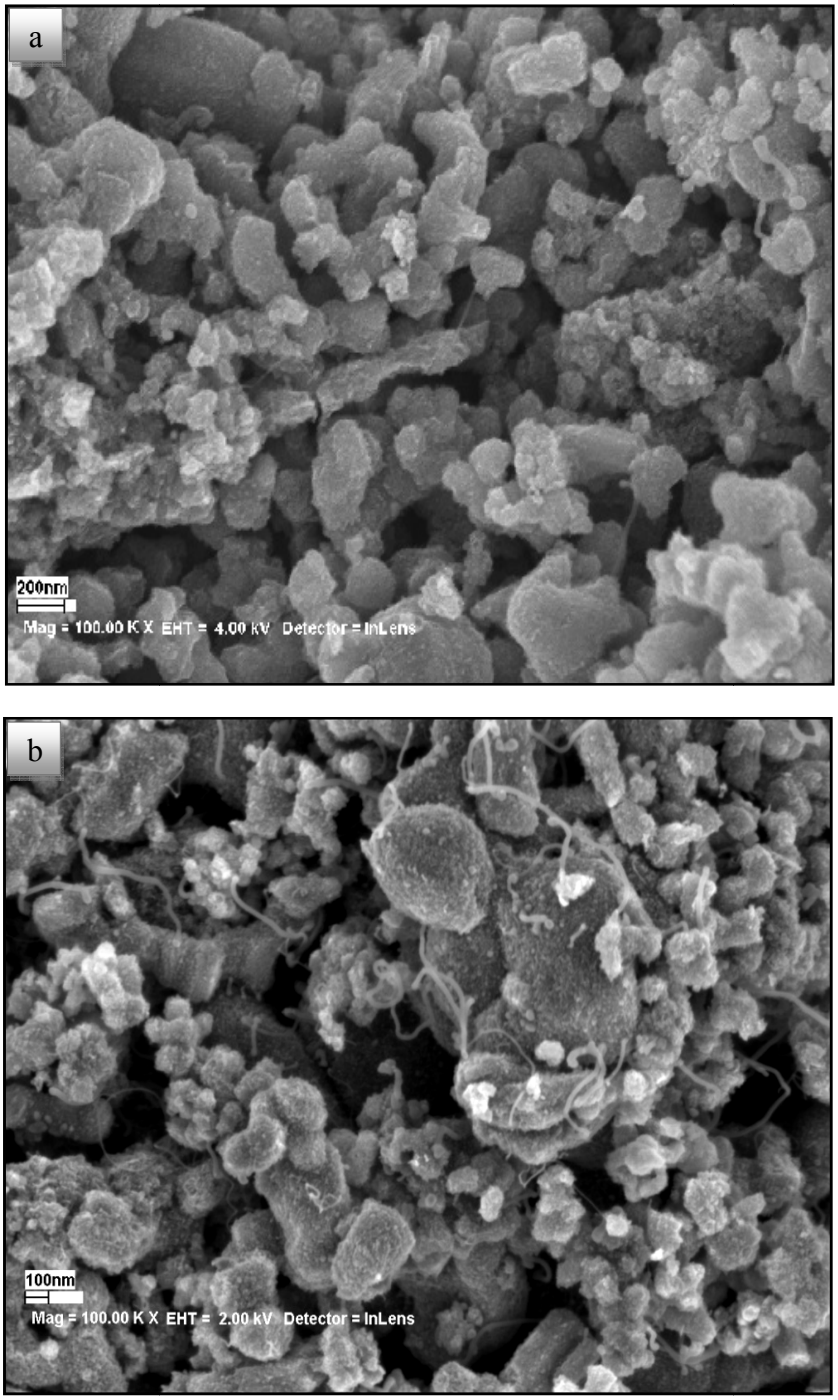

Figure 5.18: A set of SEM micrographs of Ni catalyzed CNTs: a) 2 wt % Ni-FSM-16, b) 4 wt % Ni- FSM-16

CNTs growth over Ni modified FSM-16 was illustrated in Figure 5.18. The metal type on growth was predominantly affected the morphology and density of CNTs. These results pertained to Ni catalyst, showed that CNTs growth depended on degree of filling of the d- orbitals. d-orbitals occupancy decrease in order of Ni, Co, and Fe. Because of CNTs are built by interaction between unoccupied d-orbitals of catalyst and sp^2 hybrid

orbital of carbon. For that reason, Ni exhibited the lowest activity. The important point that was dealing with here was the ability of catalysts to initiate the CNTs growth as they reached their active state. There was evidence that, CNTs growth was not possible for 2 wt % Ni- FSM-16.

Table 5.4 represents the catalyst efficiencies for CNTs growth at 700^{o}C. Carbon deposition on catalysts increased with increasing metal amount. For Fe catalyzed reaction, as the weight percentage of Fe increased, no significant change in carbon conversion was observed. Although, increase of the iron weight percentage represented an increase of active metal species, more metal particles agglomerated easily. So, large metal particles had weaker ability for carbon nucleation. That result was also valid for Ni and Co based catalysts. Furthermore, carbon deposition and carbon conversion over 2 wt % Ni- FSM-16 was higher than 4 wt % Ni- FSM-16. However, it was amorphous carbon.

5.2.2. Effect of Temperature

Temperature was an important parameter for growth process, since the ability of a catalyst to dissociate hydrocarbon was linked to reaction temperature. Indeed, raising the reaction temperature increased the carbon formation over the catalysts. In order to investigate the temperature effect, experiments were performed between 500^{o}C to 800^{o}C.

Hydrocarbon molecules broke, carbon diffused through the catalyst particles, and then led saturation level. During this process, rate determining step was diffusion of carbon from gas/metal interface to metal/carbon interface. As a result, mass flux originated from the solubility difference of carbon at gas/metal interface and metal/carbon interface. For low temperatures carbon solubility in solid solutions was very low. Therefore, CNTs structure was not observed at 500^{o}C.

Figure 5.16, and Figure 5.19- 22 illustrates the CNTs growth over 4 wt % Fe- FSM-16 and 2 wt % Fe- FSM-16 at 600^{o}C, 700^{o}C and 800^{o}C. It was obvious that temperature had predominant effect on CNTs growth. Raising the temperature affected the morphology of nanotubes. The effect of increasing the temperature of CVD was to increase diameter of CNTs. Because of the particle size effect, CNTs growth over 2 wt % Fe- FSM-16 showed smaller diameter distribution compared those for 4 wt % Fe-

FSM-16. However, diameter distribution at 800^{o}C was very broad. Because, at higher temperatures, more iron particles migrated on FSM-16 surface, so agglomeration was possible. Moreover, Zhao et al [4] suggested possibility of acetylene pyrolysis on CNTs sidewalls, leading to tube diameter thickening.

Additionally, increasing temperature created tendency to increase growth rate and carbon solubility due to enhanced diffusion. For the CNTs growth over Fe- FSM-16, the most important parameter was providing carbide particles. For that reason, carbon solubility in solid solution and rapid carbon diffusion were critical. Indeed, for the iron system, it was specifically to be noted that formation of iron carbide depended on temperature. At temperatures below 500^{o}C rate of carbide formation was greater than that of the decomposition rate. There was a remarkable change in the rate of iron carbide decomposition at temperature between 500^{o}C- 725^{o}C. Following this, presence of graphite phase changes iron carbide ratio, therefore, metal phase gradually existed. For temperatures higher than 725^{o}C, carbide decomposition was pronounced and the iron phase was stable. There was an evidence that, after certain temperature considerable amount of α-Fe formed and catalyst arrived its active state [63]. Requirement of α-Fe for graphite precipitation, at 500^{o}C explained why carbon nanotube could not exist over Fe- FSM-16.

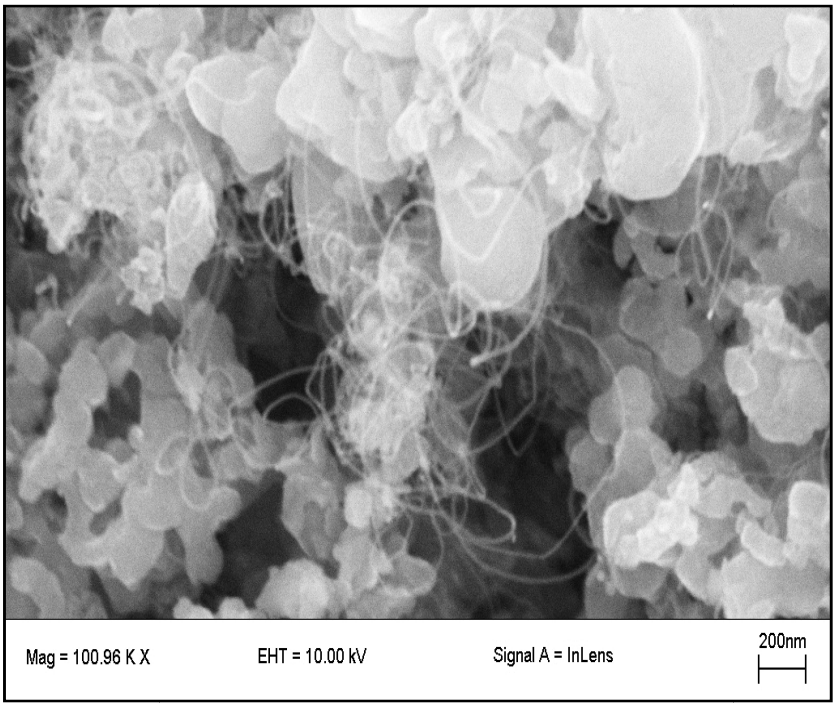

Figure 5.19: CNTs growth over 4 wt % Fe- FSM-16 at 600^{o}C

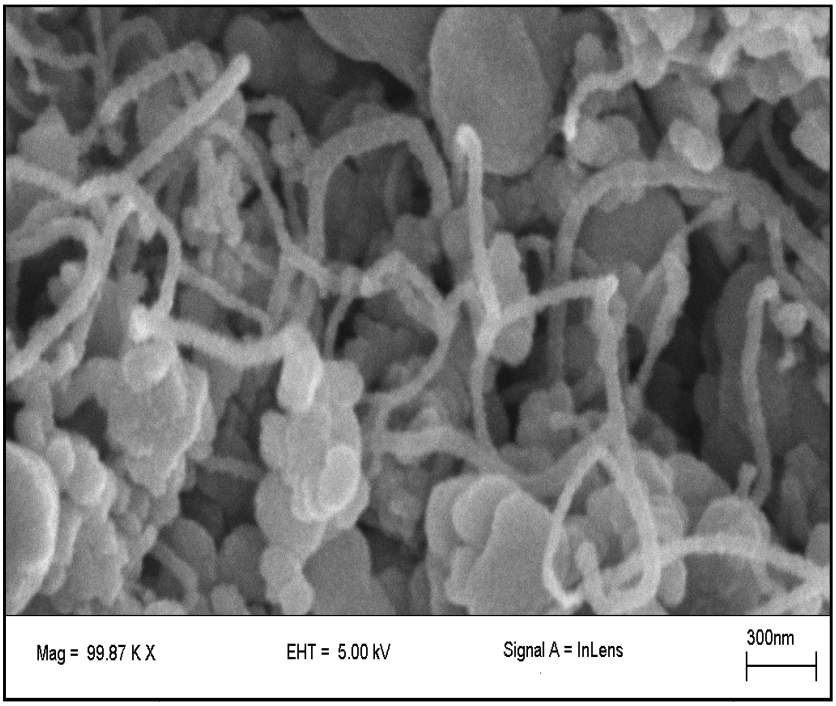

Figure 5.20: CNTs growth over 4 wt % Fe- FSM-16 at 800^{o}C

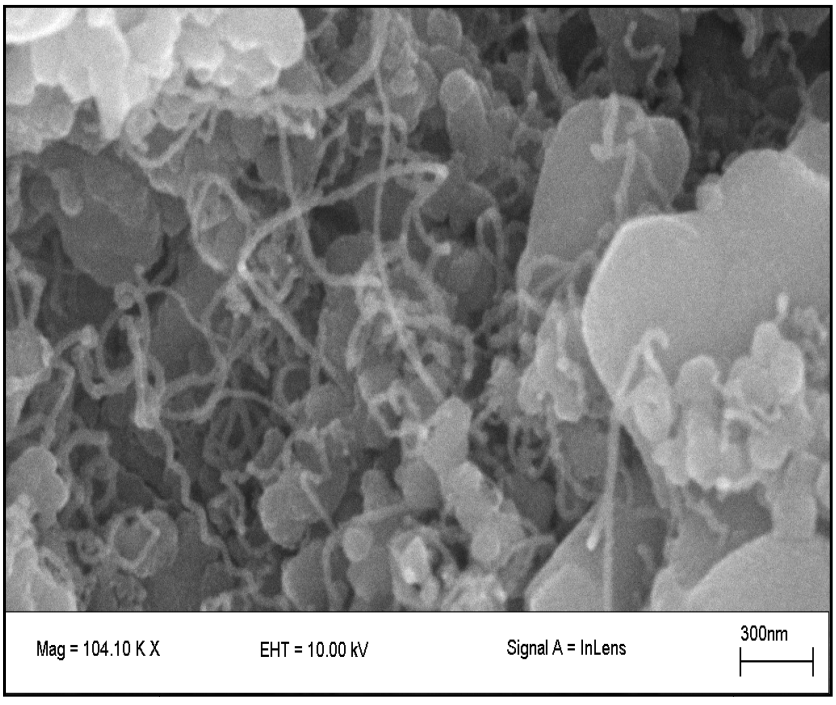

Figure 5.21: CNTs growth over 2 wt % Fe- FSM-16 at 600^{o}C

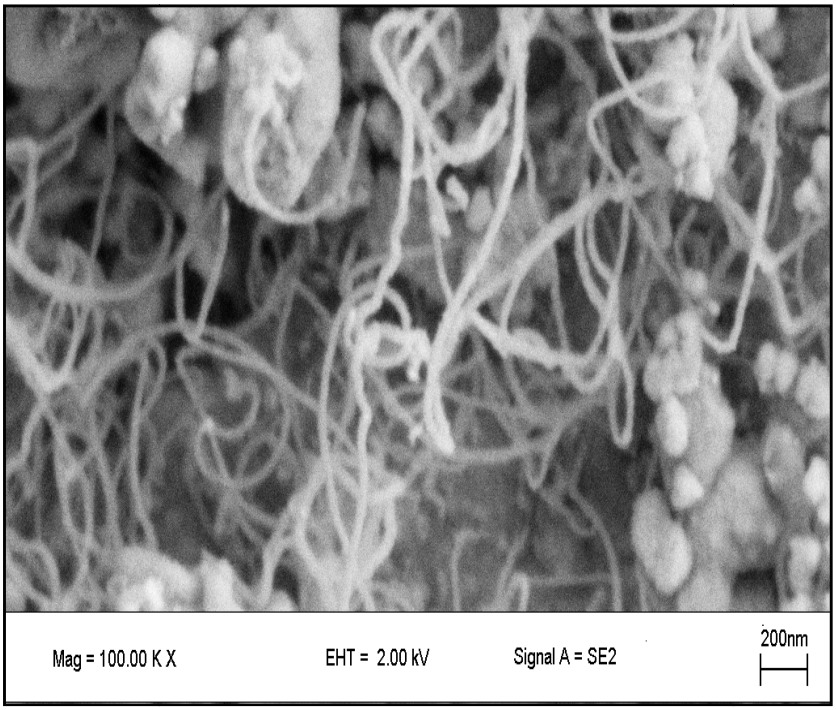

Figure 5.22: CNTs growth over 2 wt % Fe- FSM-16 at 800^{o}C

The phase diagram for iron-carbon is also shown in Figure 5.23. From the diagram, 723^{o}C is threshold temperature, above this temperature only Fe_3C phase can exist. For graphite precipitation, Fe_3C phase is completely saturated with carbon (6.67 wt % C). As a result, increasing temperature led to reach saturation level and excess carbon interacted with α-Fe precipitated as graphite.

From SEM images, it was clear that, growth mechanism of carbon nanotubes was tip growth. It was obviously observed from the results, metal particles were present at the top of the nanotube. Due to weak interaction between metal particle and support, diffused carbon lifted metal particles to top of the nanotube.

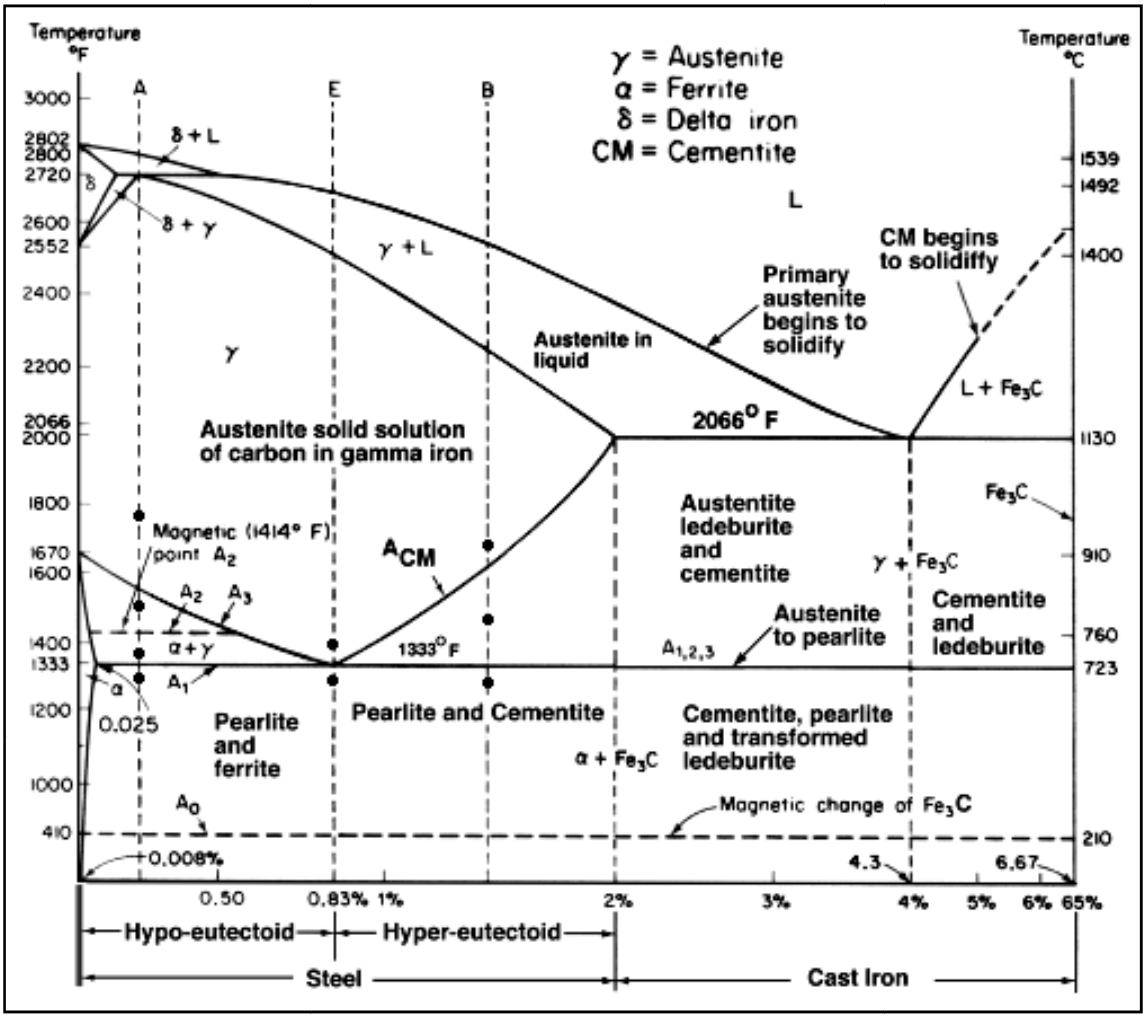

Figure 5.23: Iron - carbon binary phase diagram [88, 89]

CNTs growth was also performed on Co and Ni modified FSM-16. Growth on Co and Ni catalysts at 800^{o}C are shown in Figure 5.24. It was observed that no nanotube structure grown at 500^{o}C. This was due to the fact that the solubility of carbon was very low at 500°C. The temperature was then increased to 600^{o}C, there was not any CNT structure observed for 2 wt % Ni and Co FSM-16 and less CNT structures were observed at 4 wt % Ni and Co FSM-16. It was useful to point out that, at low temperatures Co and Ni solubility in carbon and carbon diffusion were low. As demonstrated in Figure 5.17 and Figure 5.18, CNTs could grow at temperature 700°C. These results demonstrated that Co and Ni particles reached their active state at this temperature. Figure 5.25 and 5.26 gives the evaluation of carbon deposition and carbon conversion with respect to temperature for all type of catalyst. The results for Fe, Ni and Co-FSM-16 showed that Fe-FSM-16 was a promising candidate. It was clear that, carbon conversion increased with increasing temperature. However, amount of CNTs

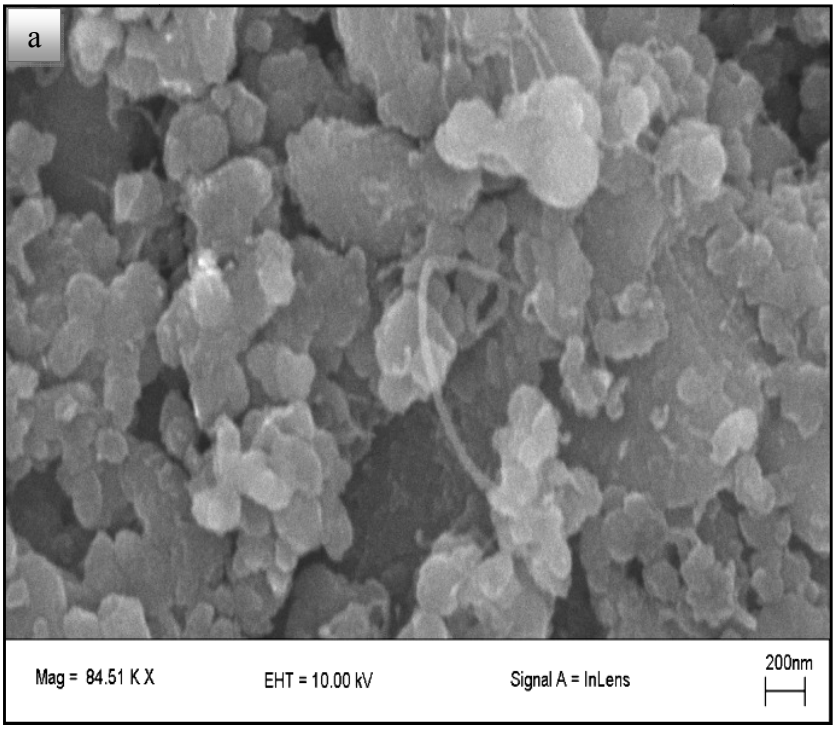

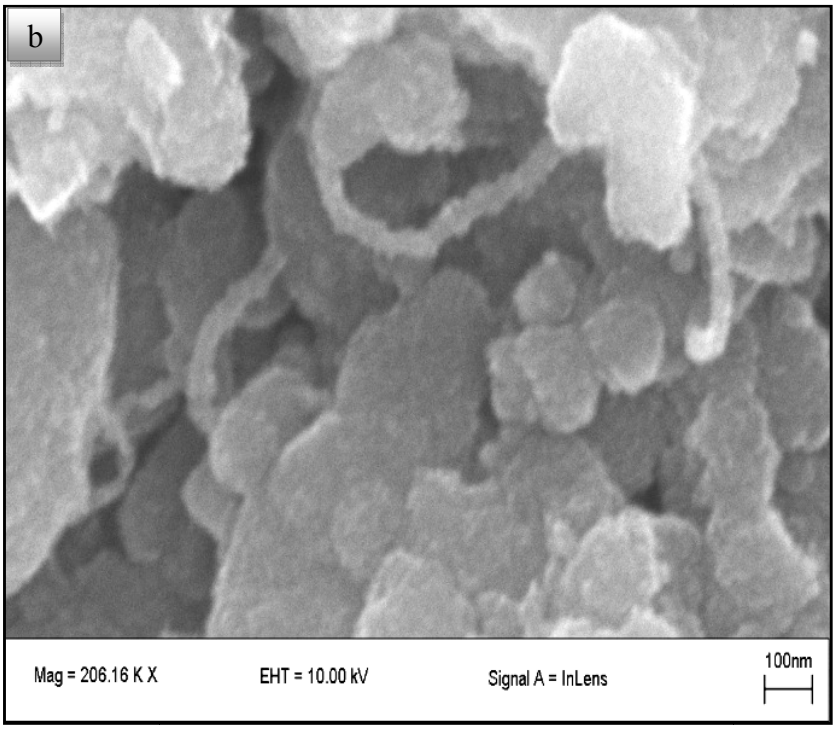

Figure 5.24: CNTs growth over a) 4 wt % Co- FSM-16 at 800^{o} C b) 4 wt % Ni- FSM-16 at 800^{o} C

formed over Ni-FSM-16 and Co-FSM-16 were less than Fe-FSM-16 for all temperatures. At 600°C, the rate of carbon nucleation was low compared to rate of diffusion. Under this condition, low affinity for carbon decomposition and slow nucleation rate of carbon made nanotube formation much more difficult. At 800°C, Co-FSM-16 and Ni-FSM-16 lost their activity compared to Fe-FSM-16. When the temperature was 800°C, the decomposition rate of hydrocarbon molecules and solubility of carbon at the gas/metal interface increased. But, diffusivity of carbon in metal particle became more crucial. Zang et al. reported that carbon diffusivity in Fe is 2.7×10^{-6} cm^2 s^{-1} at 900°C. On the other hand, for the same temperature, diffusivity in Co is 6.94×10^{-12} cm^2 s^{-1} [90]. It was found that, low amounts of CNTs over Co- FSM-16 associated with diffusion limitation. Because, rapid formation of carbon at the metal/gas surface caused encapsulation of active surface and blockage of catalysts pores [91]. Deactivation of catalyst led to amorphous carbon formation instead of carbon nanotube formation.

Within these results, Fe was found to be most effective catalyst for all temperatures. Although temperature increase led to high CNTs yield, enhanced diffusion of carbon and carbon solubility contributed to increase of average diameter of CNTs. For appropriate CNTs yield, the reaction temperature and the catalyst were chosen to be 700^{o}C and 4 wt % Fe- FSM-16.

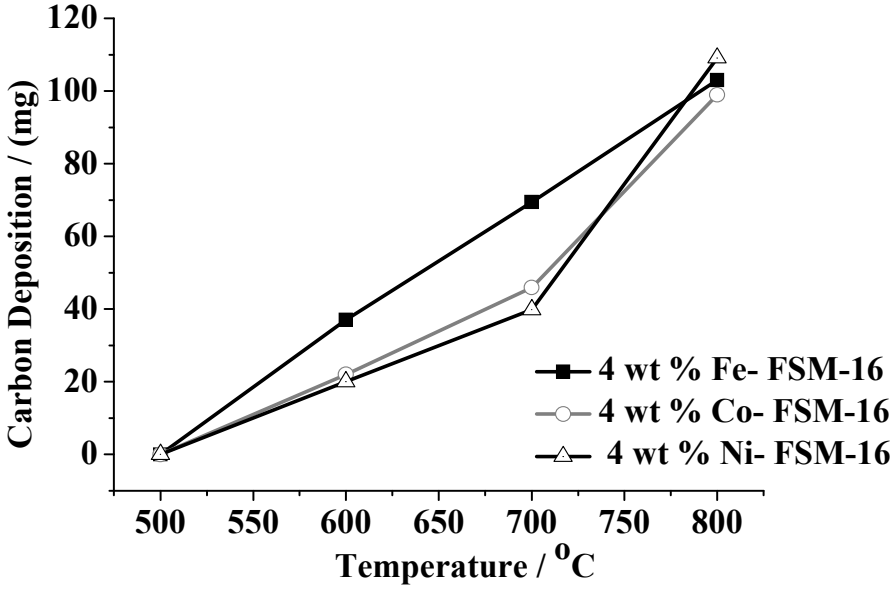

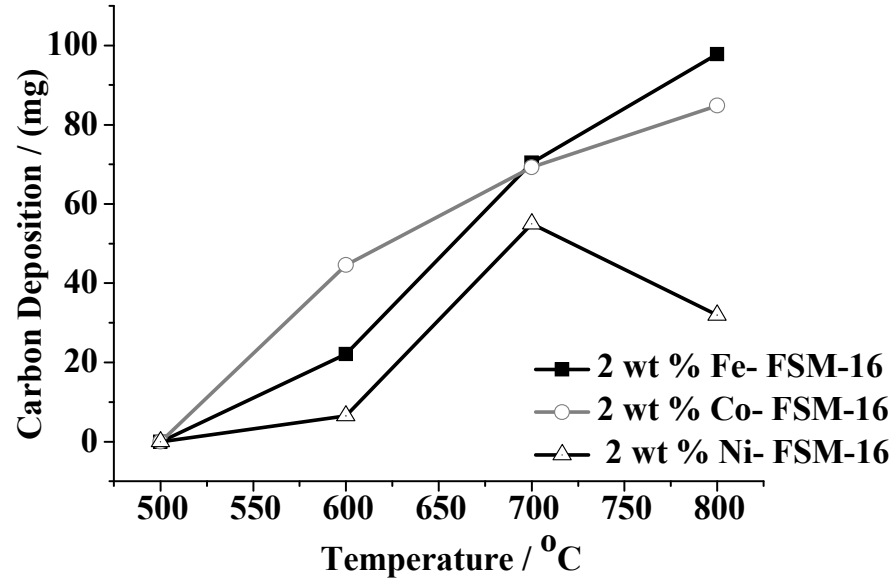

Figure 5.25: Carbon deposition change as a function of reaction temperature

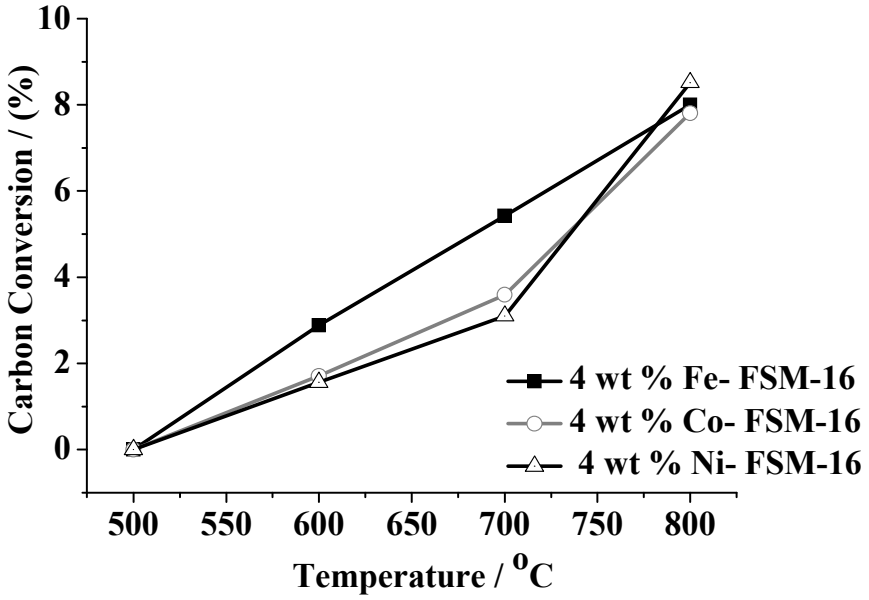

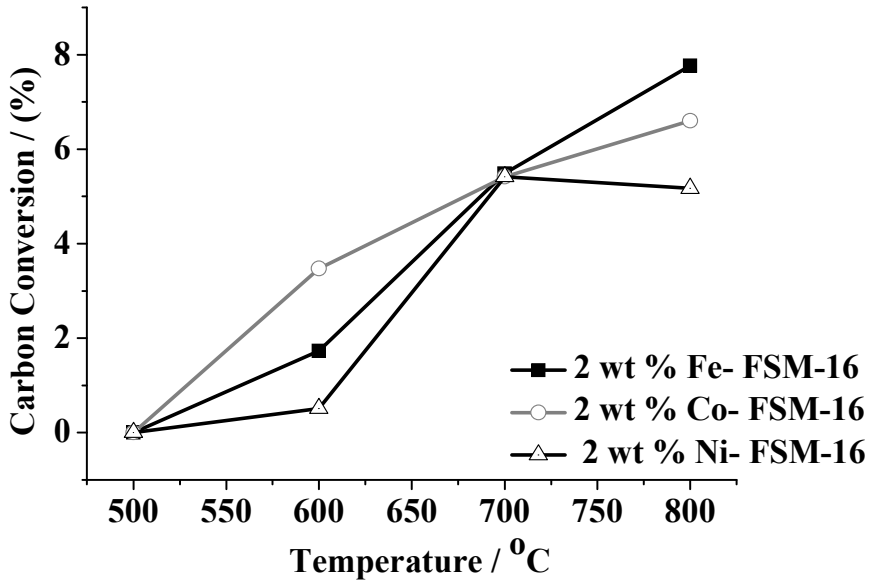

Figure 5.26: Carbon conversion change as a function of reaction temperature

5.2.3. Effect of Acetylene Flow Rate

In order to investigate the effect of hydrocarbon precursor on amount of carbon nanotube formation, the experiments were carried out at 700^{o}C with 30 min reaction time.

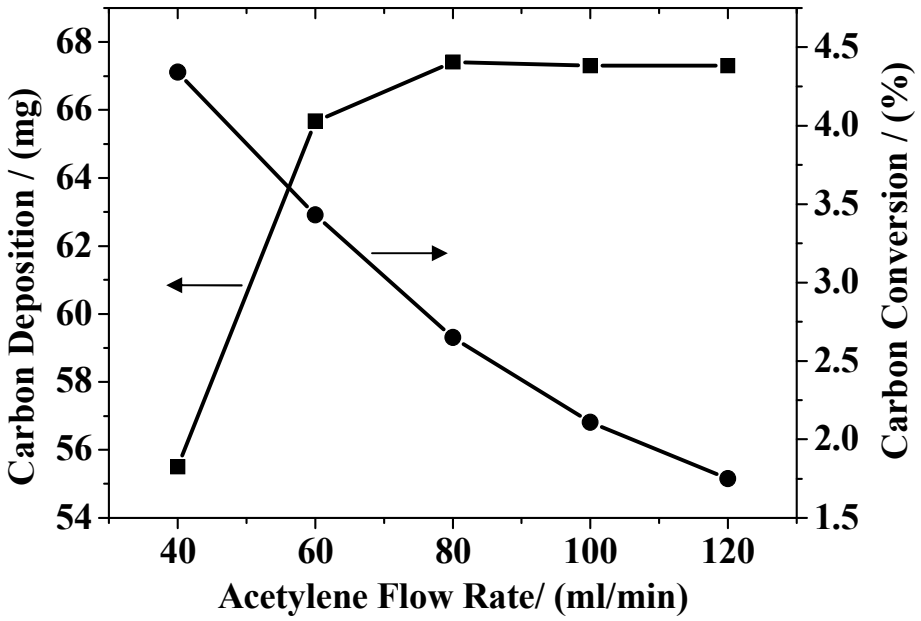

Figure 5.27: Amounts and conversion of carbon with different flow rate of acetylene

According to above analysis (Figure 5.27), carbon amount on the catalyst increased with increasing acetylene flow rate from 40 to 120 mL/min. Carbon deposition reached to a constant amount when acetylene flow rate was between 80-120 mL/min. Up to 80 mL/min, acetylene flow rate increment directly promoted decomposition of acetylene and consequently carbon accumulated on 4 wt % Fe-FSM-16. For flow rate was greater than 60 mL/min, it was found that there was no mass flux between acetylene/metal interface since they reached equilibrium. Excess carbon deposited as an amorphous carbon on the wall of quartz tube. Due to carbon transfer limitation between hydrocarbon source and metal interface, carbon conversion decreased with increased flow rate of acetylene.

Acetylene flow rate did not have significant effect on the morphology of the resulting CNTs. The resulting CNTs are shown in Figure 5.28 and Figure 5.29. It was observed that CNTs diameter was almost same and it changed in the range of 20-35 nm.

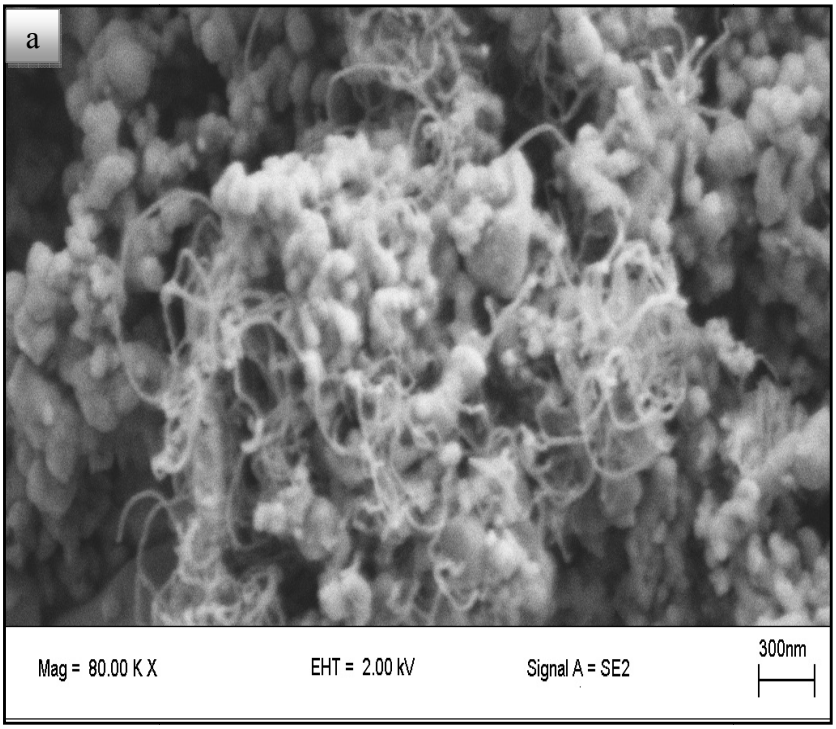

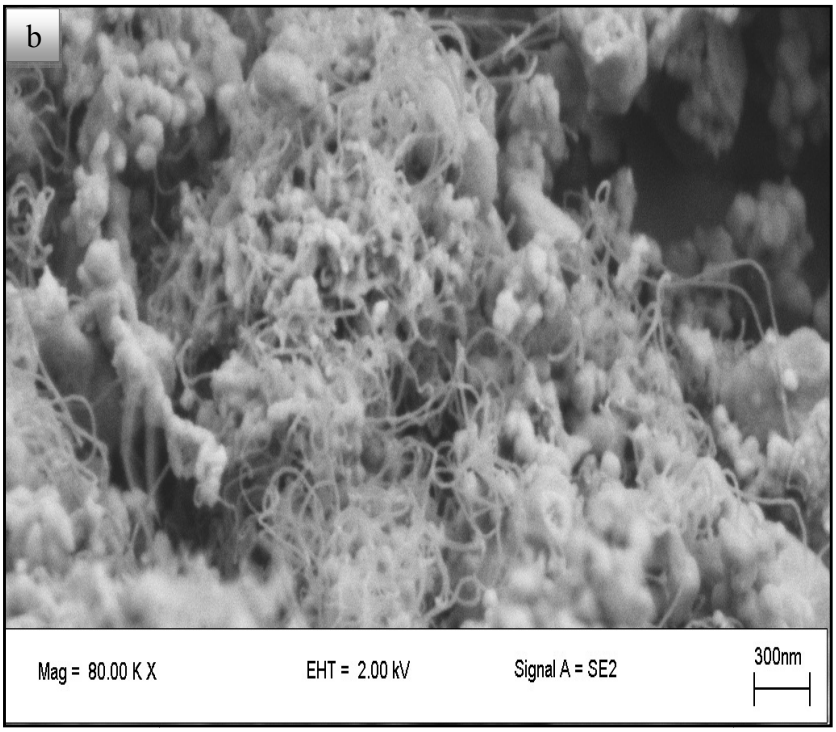

Figure 5.28: CNTs growth over 4 wt % Fe- FSM-16 with a) 60 ml/min acetylene flow rate, b) 80 ml/min acetylene flow rate

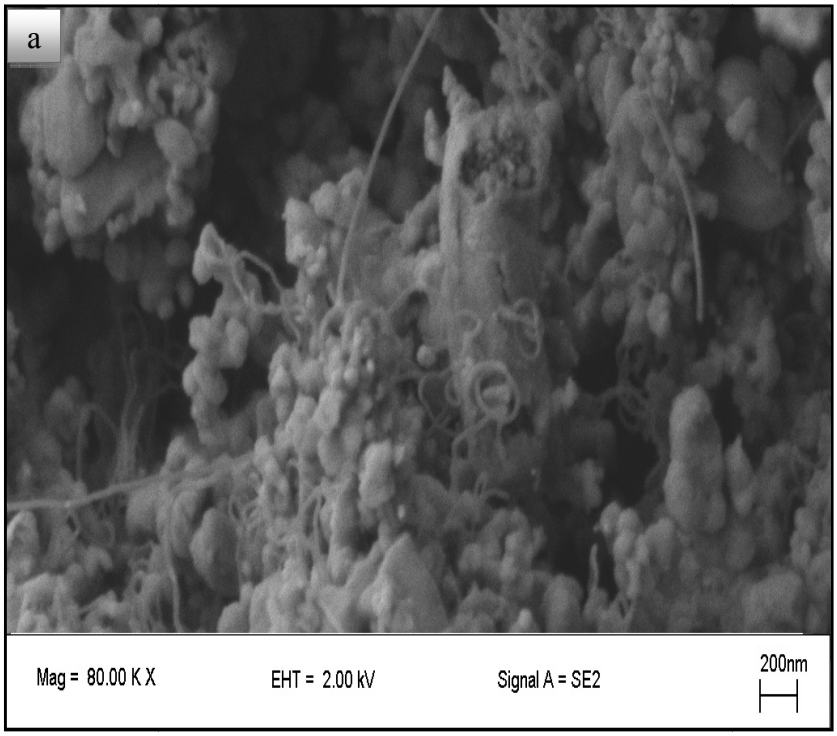

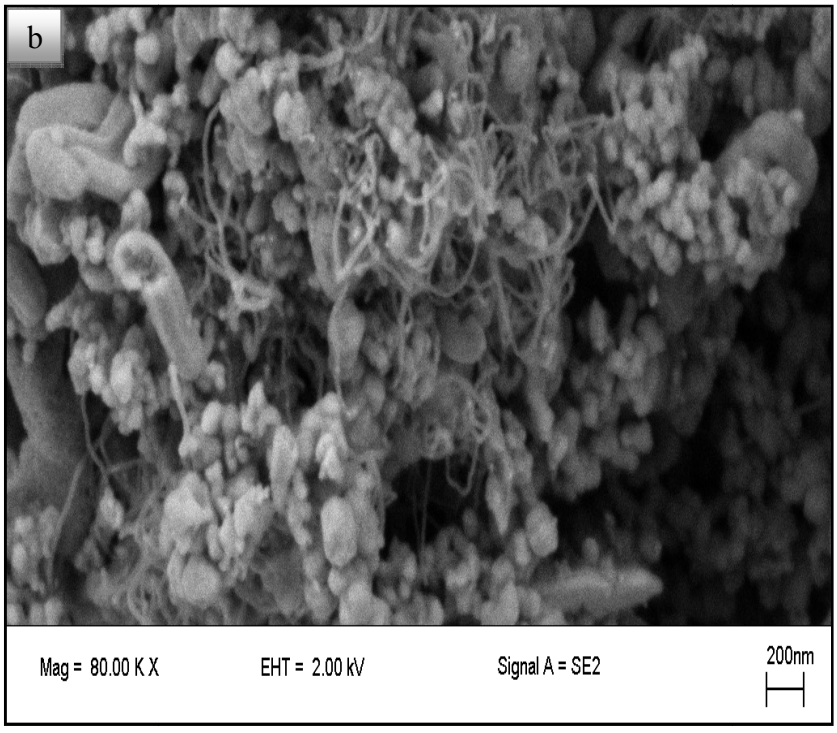

Figure 5.29: CNTs growth over 4 wt % Fe- FSM-16 with a) 100 ml/min acetylene flow rate, b) 120 ml/min acetylene flow rate

5.2.4. Raman Spectroscopy Analysis

Raman spectroscopy is a powerful tool for characterization as-synthesized CNTs with respect to diameter and quality of nanotubes. The Raman spectra present different features being sensitive to diameter of carbon nanotubes. It is possible to distinguish SWCNTs and MWCNTs from each other. Owing to recognizable bands make Raman spectra unique for SWCNTs. Raman spectra is dominated by higher and lower wavenumber region. Radial breathing mode (RBM) features appear over lower wavenumber region. RBM modes corresponds coherent vibration of C atoms in radial direction. Raman bands appearing between 120 cm^{-1}-350 cm^{-1} are related to the SWCNTs for diameters in the range of 0.7-2 nm [92, 93]. The Raman bands at higher wavenumber region are both characteristic for SWCNTs and MWCNTs. The band in the range of 1500-1605 cm^{-1} is referred G band (Graphite Band). G band correspond to vibration of C-C bond of graphene sheet. D band (Disorder Band) is usually observed at in the range 1250-1450 cm^{-1}. D band is the result of disordered-induced vibration of C-C bond. *D/G* peak intensity ratio is an index for determining the CNTs structure [92].

Results of Raman spectra of CNTs produced over Fe, Co, Ni with different metal amount is represented in Figure 5.30. Clearly, D and G bands were present in the spectra.

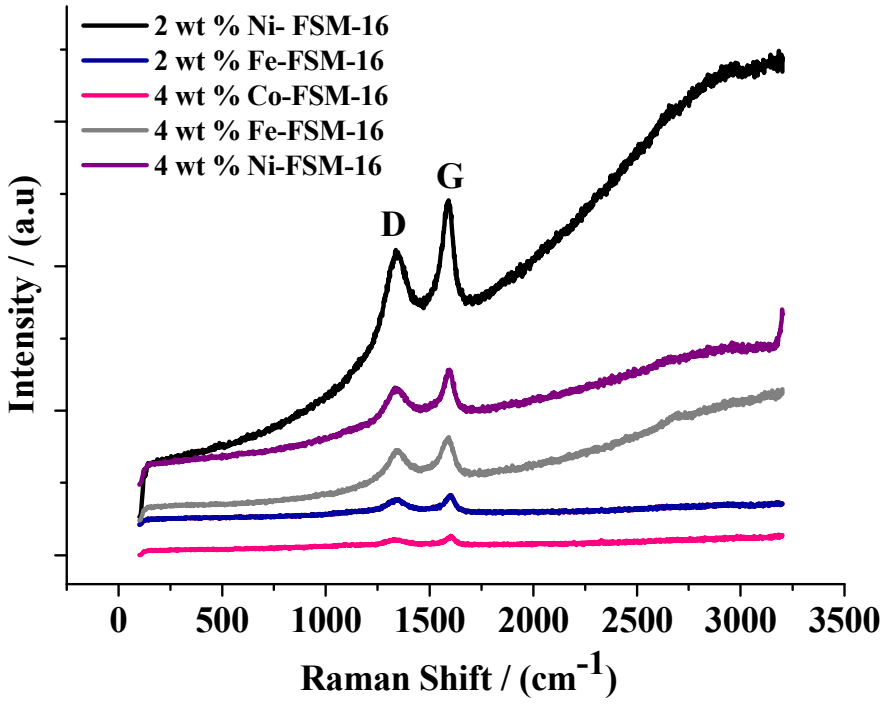

Figure 5.30: Raman spectra of carbon deposits on metal-FSM-16 at 700°C

Presence of D and G band indicating that graphitic carbon was obtained. No peak observed in the RBM region. Therefore, CNTs growth was to be MWCNTs. As the metal amount and metal type changed, Raman spectra became different for each sample. It was concluded that the quality of CNTs was different for each sample. Raman spectra of CNTs had a G band at 1592 cm^{-1} and D band at 1341 cm^{-1} and 1336 cm^{-1}. As the metal amount increased, position of G band was similar; however, D band had small shift from 1336 to 1341 cm^{-1}. Moreover, among as-synthesized CNTs, Raman spectra of CNT growth over 2 wt % Ni- FSM-16 had a strong G band at 1592 cm^{-1}.

Table 5.5: Parameters of D and G band for carbon deposits on metal-FSM-16 at 700^{o}C

Sample	Raman Shift (cm^{-1}) (D-Band)	Raman Shift (cm^{-1}) (G-Band)	Absolute Intensity (D-Band)	Absolute Intensity (G-Band)	I_D/I_G
4 wt % Fe-FSM-16	1341	1592	2426	2880	0.84
4 wt % Co-FSM-16	1341	1592	563	642	0.88
4 wt % Ni-FSM-16	1341	1592	3332	3970	0.84
2 wt % Fe-FSM-16	1336	1592	877	972	0.90
2 wt % Ni-FSM-16	1336	1592	9256	10978	0.84

Table 5.5 presents the absolute intensity of the bands and I_D/I_G ratio. The intensity ratio D band to G band is the measure of amount of disorder in the nanotube. The intensity ratio of the D to the G band was almost 0.84; the corresponding value was 0.88 for CNTs growth over 4 wt % Co- FSM-16 and it was 0.90 for 2 wt % Fe- FSM-16. This showed that, these nanotubes had lower crystallinity compared to others because higher ratio of I_D/I_G attributed to presence of amorphous carbon.

Additionally, the effect of CVD temperature on the formation of CNTs over 4 wt % Fe-FSM-16 were demonstrated in Figure 5.31. Clearly seen from the spectra, there was no band around RBM region meaning that CNTs were MWCNTs. Although temperature of the CVD was changed, SWCNTs production did not achieve.

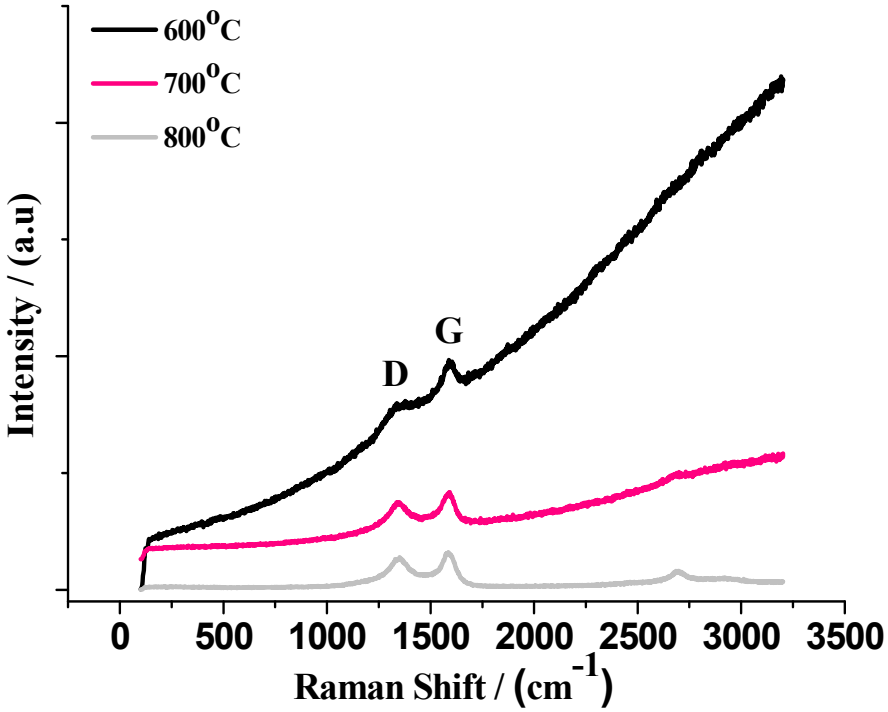

Figure 5.31: Raman spectra of carbon deposits on 4 wt % Fe-FSM-16 at different temperatures

The G and D band were observed only in the Raman spectra of 4 wt % Fe-FSM-16. While the G band was seen at 1589 cm^{-1} at 600°C, band appeared at 1592 cm^{-1} at 700°C and 800°C. The D band position changed from 1341 cm^{-1} (600°C and 700°C) to 1350 cm^{-1} (800°C). Moreover, as the CVD temperature increased, both G and D band intensity decreased.

The comparison of the intensity ratios of these two peaks were given in Table 5.6. It was observed that increasing temperature resulted decrease in intensity of G and D band. In the temperature range 600-700°C, *D/G* peak intensity ratios were 0.81, 084, and 0.87. These indicated the morphology changes of MWNTs. It was concluded that, structure of CNTs depend on CVD temperature. At higher growth temperatures (700 and 800°C), D band became stronger and degree of crystalline perfection of the CNTs decreased. As previously mentioned, decomposition of acetylene was very rapid at higher temperatures. This rapid decomposition resulted in excess carbon on the catalyst surface. As a result, excess carbon deactivated the Fe particles and CNTs growth with a worse graphite structure.

Table 5.6: Parameters of D and G band for carbon deposits on 4 wt % Fe -FSM-16 at different temperature

Temperature	Raman Shift (cm^{-1}) (D-Band)	Raman Shift (cm^{-1}) (G-Band)	Absolute Intensity (D-Band)	Absolute Intensity (G-Band)	I_D/I_G
600°C	1341	1589	7981	9824	0.81
700°C	1341	1592	2426	2880	0.84
800°C	1350	1592	1378	1589	0.87

Effect of the acetylene flow rate on the structure of CNTs was also investigated. Raman spectra of CNTs growth over 4 wt % Fe- FSM-16 with 40 mL/min, 80 mL/min, 100 mL/min, and 120 mL/min acetylene flow rate is shown in Figure 5.32. There was no trace of SWCNTs formation so this spectrum proved that the as-grown CNTs were MWCNTs.

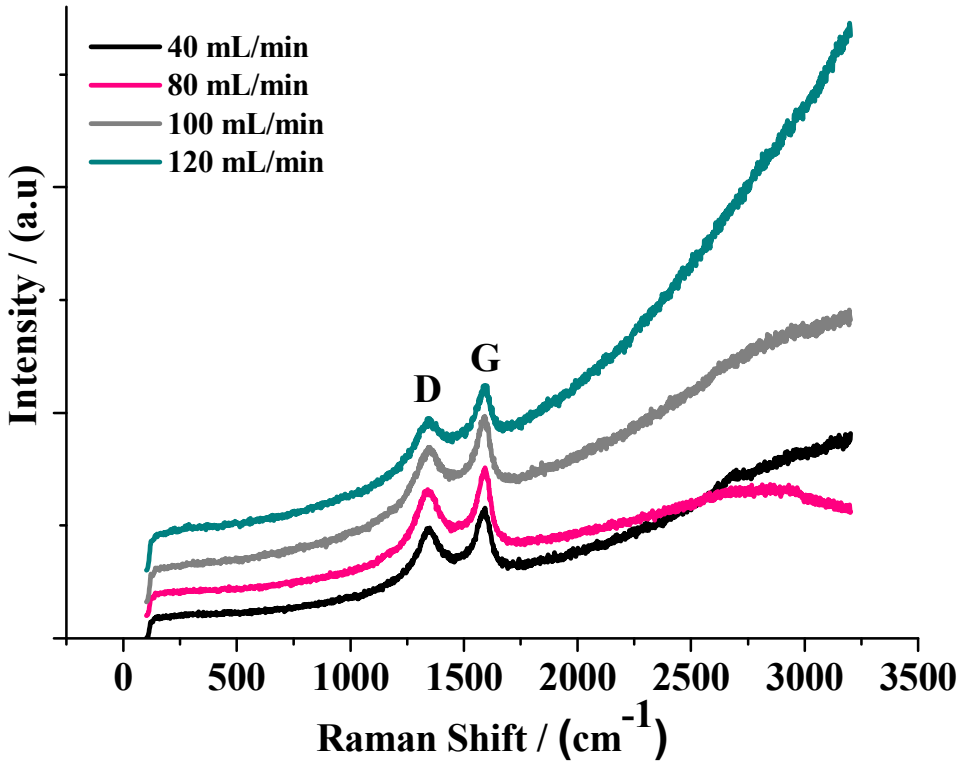

Figure 5.32: Raman spectra of carbon deposits on 4 wt % Fe-FSM-16 produced with different acetylene flow rates at 700°C

Table 5.7: Parameters of D and G band for carbon deposits on 4 wt % Fe -FSM-16 produced with different acetylene flow rates at 700^{o}C

Flow Rate	Raman Shift (cm^{-1}) (D-Band)	Raman Shift (cm^{-1}) (G-Band)	Absolute Intensity (D-Band)	Absolute Intensity (G-Band)	I_D/I_G
40 mL/min	1341	1592	2426	2880	0.84
80 mL/min	1356	1579	2550	3060	0.83
100 mL/min	1358	1585	3380	4093	0.83
120 mL/min	1356	1595	3335	4004	0.83

The ratio of the D band intensity to G band intensity was given in Table 5.7. G band and D band intensities increased with increasing acetylene flow rate, however, the ratio of these two band was almost same. This result indicated that flow rate of acetylene did not significant effect on quality of CNTs.

5.2.5. TGA Analysis

Both Raman measurements and SEM images showed that 4 wt % metal impregnated FSM-16 was better for CNTs growth than 2 wt % metal impregnated samples. Therefore, TGA measurements for CNTs growth over 4 wt % Fe, Co, and Ni impregnated FSM-16 were performed in order to investigate the quality of CNTs. Measurements performed under air atmosphere with a flow rate 50 ml/min, at a linear heating rate of 5^{o}C/min. Thermal behavior of CNTs growth over Fe, Co, and Ni modified FSM-16 were compared, respectively. As temperature increased, weight loss due to burning of amorphous carbon and CNTs.

TG and DTA curves of samples are shown in Figure 5.33 and Figure 5.34. It was noted that increasing temperature resulted in weight loss due to burning out of carbon. TG curve exhibited one sequential zone between 375- 817^{0}C. Approximately, 60 wt % of the total mass burned out at temperature below 817^{0}C. According to literature, mass loss over the range 300-400^{0}C corresponds to combustion of amorphous carbon and burning of CNTs takes places at 400-650^{0}C [94, 95]. Residual mass corresponded to 40 wt % of the total mass was composed of metal oxides. Residual mass was approximately 75 wt % of the total mass for CNTs grown at 600^{o}C. This behavior was the result of low carbon deposition at this temperature.

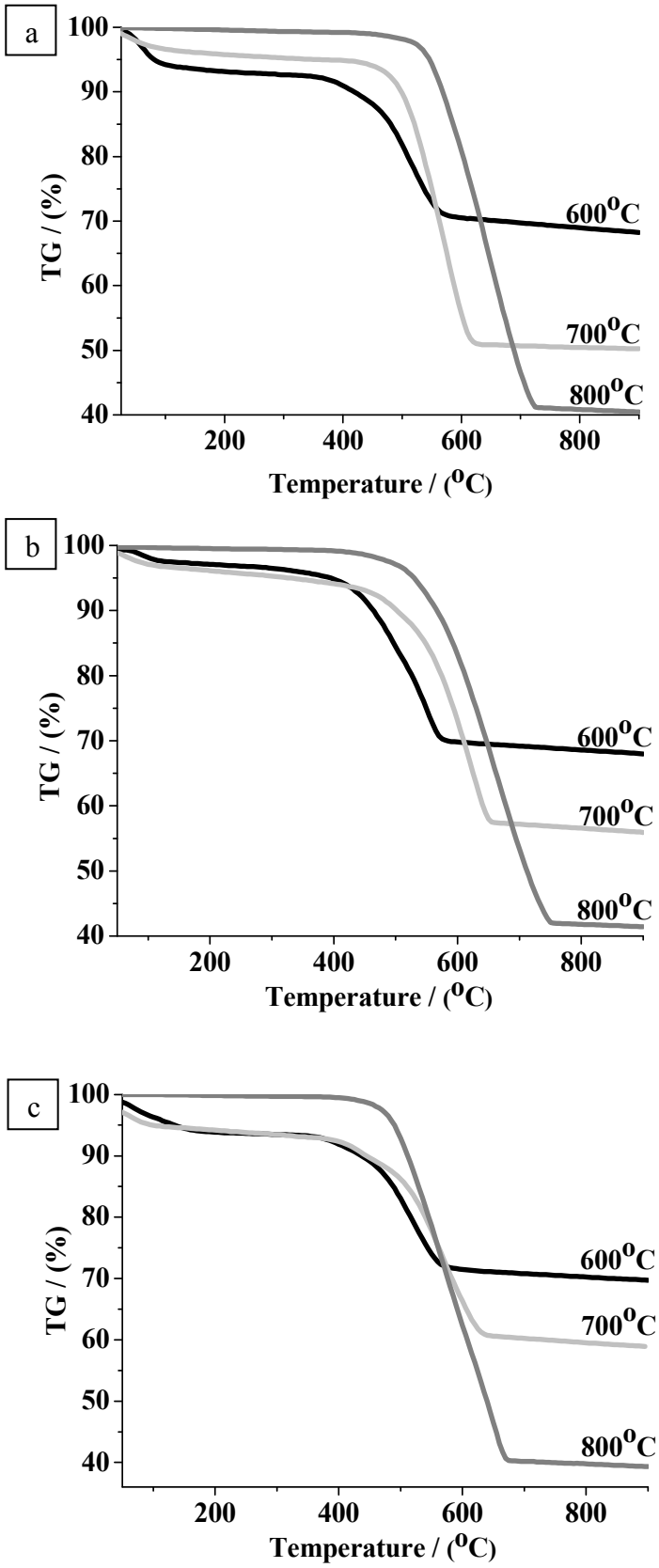

Figure 5.33: TGA thermograms of CNTs grown over a) 4 wt % Fe-FSM-16, b) 4 wt % Co-FSM-16, and c) 4 wt % Ni-FSM-16

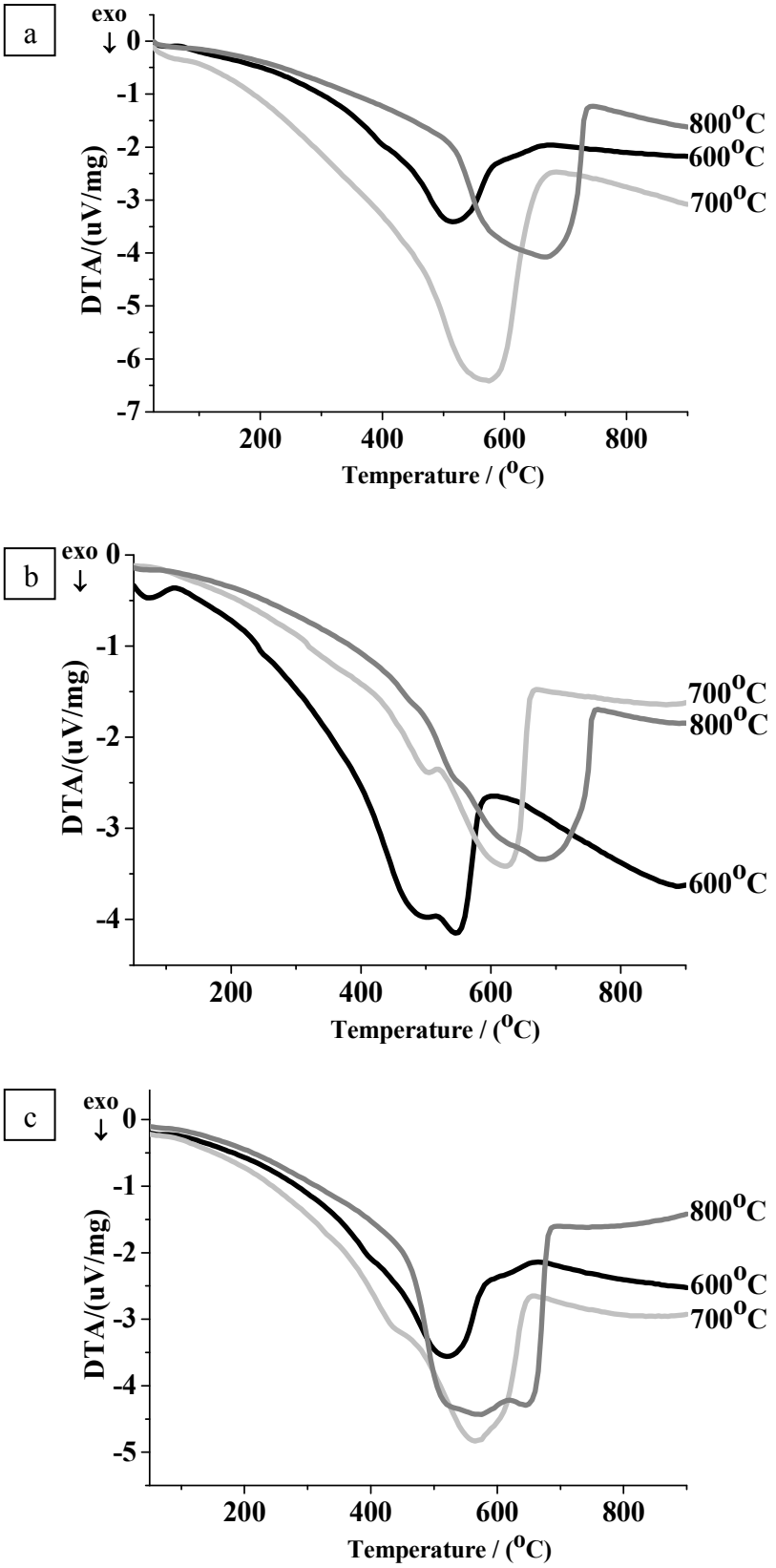

Figure 5.34: DTA curves of CNTs grown over a) 4 wt % Fe-FSM-16, b) 4 wt % Co-FSM-16, and c) 4 wt % Ni-FSM-16

Table 5.8: Onset, inflection and end temperature obtained from DTG curve

Sample	Onset Temperature	Inflection Temperature	End Temperature
CNTs-4 wt % Fe- FSM-16-600^{o}C	375	513	666
CNTs-4 wt % Fe- FSM-16-700^{o}C	436	573	686
CNTs-4 wt % Fe- FSM-16-800^{o}C	518	666	817
CNTs-4 wt % Co- FSM-16-600^{o}C	371	547	731
CNTs-4 wt % Co- FSM-16-700^{o}C	377	619	736
CNTs-4 wt % Co- FSM-16-800^{o}C	473	684	827
CNTs-4 wt % Ni- FSM-16-600^{o}C	345	520	706
CNTs-4 wt % Ni- FSM-16-700^{o}C	376	565	716
CNTs-4 wt % Ni- FSM-16-800^{o}C	406	573	724

The onset, inflection and end temperature listed in Table 5.8. CNTs grown over 4 wt % Fe- FSM-16 at 600^{o}C, 700^{o}C, and 800^{o}C started to burn at 375^{o}C, 436^{o}C, and 518^{o}C, respectively. For CNTs grown over 4 wt % Co-FSM-16 at 600^{o}C, 700^{o}C, and 800^{o}C, inflection temperatures were 371^{o}C, 377^{o}C, and 473^{o}C. And also inflection temperatures were 345^{o}C, 376^{o}C, and 406^{o}C for CNTs grown over 4 wt % Ni-FSM-16. Weight losses below 400^{o}C indicated that amorphous carbon was present. Graphite particles are more stable compared to amorphous carbon and burned at higher temperatures. With increasing temperature, inflection temperature shifted to higher temperatures. TG-DTA data proved that CNTs grown at higher temperature had better crystalline structure compared to low temperature grown [92]. Furthermore, CNTs grown over Fe modified FSM-16 showed better crystalline structure because it started to burn at higher temperatures compared to those for others.

Table 5.9: Results of onset, inflection and end temperature with various acetylene flow rate obtained from DTG curve

Sample	Onset Temperature	Inflection Temperature	End Temperature
CNTs-4 wt % Fe- FSM-16-40 mL/min	375	513	666
CNTs-4 wt % Fe- FSM-16-60 mL/min	449	591	700
CNTs-4 wt % Fe- FSM-16-80 mL/min	431	578	726
CNTs-4 wt % Fe- FSM-16-100 mL/min	443	597	724
CNTs-4 wt % Fe- FSM-16-120 mL/min	446	573	713

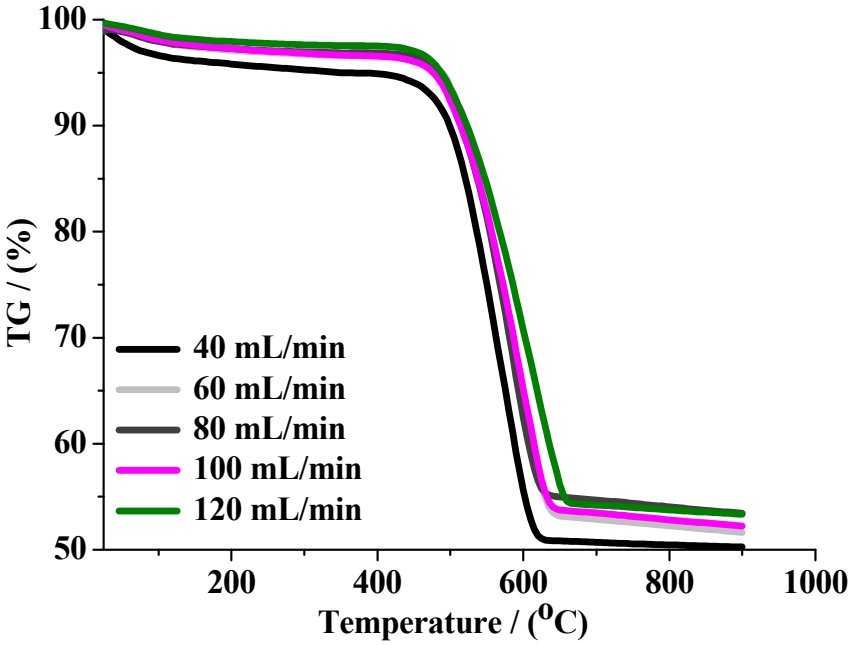

Figure 5.35: TGA thermograms of CNT growth with various acetylene flow rate

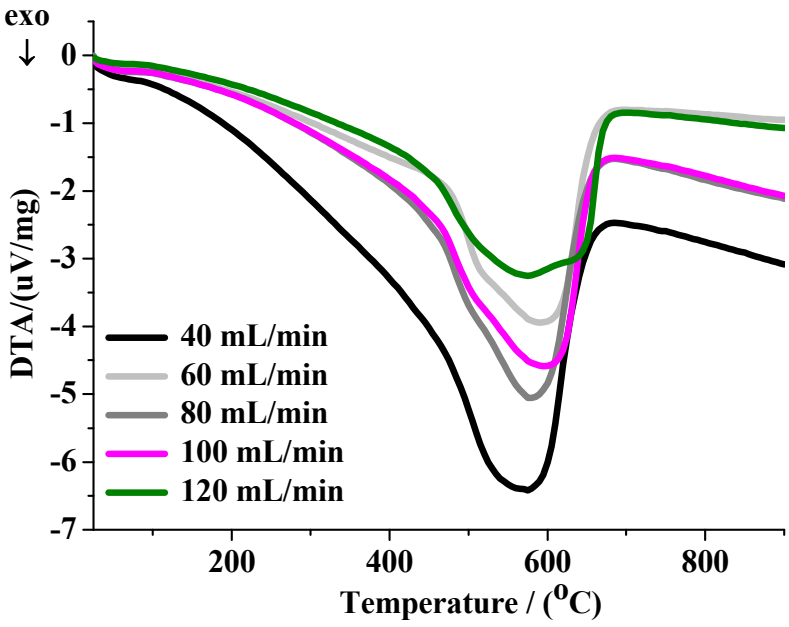

Figure 5.36: DTA curves of CNT growth with various acetylene flow rate

Effect of acetylene flow rate on graphitization of CNTs grown over 4 wt % Fe-FSM-16 at 700^{o}C was investigated. TG and DTA curves of samples are illustrated in Figure 5.35 and Figure 5.36. In the case of flow rate increased from 40 mL/min to 120 mL/min, TG curves exhibited one sequential zone. Furthermore, residual mass was 50 wt % of the total mass. Table 5.8 revealed the decomposition temperature of as-synthesized CNTs. It was noted that, the peak of maximum weight loss and inflection temperature shifted toward to higher temperatures with increasing acetylene flow rate. With increasing flow rate above 60 mL/min, inflection temperature was almost same. It was found that, for flow rate above 60 mL/min, CNTs had better crystalline structure and the optimum flow rate was in the range of 60-120 mL/min.

CHAPTER 6

6. Conclusion

In this study, CNTs grown over catalytic metals such as Fe, Co, and Ni impregnated FSM-16 were examined. Effect of metal concentrations and CVD temperature were investigated in the production of CNTs. After determining the optimum metal percentage, promising metal type and CVD temperature, effect of acetylene flow rate was investigated. Fe, Co, and Ni-FSM-16 catalysts were prepared by wet impregnation method. They were used for CVD reactions and following observations were concluded;

- Ordered hexagonal FSM-16 molecular sieve with high specific surface area were successfully synthesized with using kanemite and hexadecyltrimethylammonium bromide were used as a starting material. As-synthesized FSM-16 was calcinated 550^{o}C for 6h to remove the surfactant from silicate-organic complex. Fe, Co and Ni modified FSM-16 were synthesized via wet impregnation method and surfactant removed after 6h calcination at 550^{o}C.

- XRD results showed that, metal impregnation on the FSM-16, led to partial loss of long range order of hexagonal arrays. Both XRD and ^{29}Si-NMR proved that as the metal amount increased, degree of deterioration of hexagonal array was increased. Therefore, unit cell parameter was extending due to presence of metal particles in the siliconeous matrix. N_2 physisorption results were in good agreement with XRD and ^{29}Si-NMR results. Metal impregnation into matrix resulted in reducton of the surface area, pore volume and pore diameter. It was concluded that mesoporous ordering decreased with increasing amount of Fe, Co and Ni.

- In order to understand the effect of metal impregnation on morphology of FSM-16, both FSM-16 and Fe, Co and Ni impregnated FSM-16 were analyzed by SEM. SEM images demonstrated that metal impregnation caused partial loss of

spherical and porous structure of FSM-16. But, kanemite sheets were present in the structure.

- To optimize CVD conditions, the catalyst effect on CNT growth and structure at 700^{o}C was investigated. It was found that catalyst performance due to amount of carbon deposition and carbon conversion was in the order of Fe > Co > Ni. In addition to this, size and number of active catalytic particles were also important. SEM images showed that The CNTs grown on Fe catalyst revealed maximum density of CNTs among the three catalysts and Ni exhibited the lowest activity. Moreover, as the metal amount decreased 4 wt % Fe to 2 wt % Fe, number of CNTs on the catalyst was also decrease.

- Four different temperatures (500^{o}C, 600^{o}C, 700^{o}C, and 800^{o}C) were examined for CNT growth. At 500^{o}C, no CNTs grown were observed because of low carbon solubility in metal particles. At 600^{o}C, significant CNTs formation was observed for Fe-catalyst. Higher reaction temperatures contributed to significant amount of carbon deposited on the catalyst and carbon conversion due to enhance diffusion of carbon through the metal particles. It was known that, at higher temperatures, large Fe particles formed and diameter of the CNTs was increase. On the other hand, at 800^{o}C large metal particles formation and rapid decomposition of carbon on the surface were inactivating the Co and Ni particles and also CNTs formation. Metal amounts 2 % wt/wt were sufficient for CNT formation. But 4 % wt/wt gave the highest carbon conversion. For that reason, the reaction temperature and the catalyst were chosen to be 700^{o}C and 4 wt % Fe- FSM-16 for appropriate CNTs formation.

- The effect of acetylene flow rate on ability of CNTs production of 4 wt % Fe-FSM-16 at 700^{o}C using 40 mL/min-120 mL/min acetylene flow rate was studied. The carbon amount deposited on the Fe catalyst increased until the acetylene flow rate reached 80 ml/min and it was constant with increasing flow rate. This behavior was the result of equilibrium of carbon concentrations between acetylene/metal interfaces. Moreover, SEM images demonstrated that CNTs diameter was almost same with increasing acetylene flow rate.

- Raman spectra was used to distinguish SWCNTs between MWCNTs. Raman results clearly indicated that CNTs were MWCNTs. The metal type and temperature effect can be explained by I_D/I_G ratio which indicates the degree of crystallinity of CNTs. It can be concluded that CNTs formation on both 4 wt/wt % and 2 wt/wt % metal impregnated catalysts were almost same. However, significant crystallinity difference was observed for CNTs grown over 4 wt % Fe-FSM-16 and 2 wt % Fe-FSM-16. Raman results demonstrated that CNTs grown on 4 wt % Fe-FSM-16 had higher crystallinity than those for 2 wt % Fe-FSM-16. Although, the CNTs grown on Co and Ni catalysts exhibited comparable degree of crystalline character, numbers of CNTs grown on those catalysts were really low. Therefore, Raman results supported that CNTs can be grow over 4 wt % Fe-FSM-16 with high crystallinity and yield.

- Some of the as-grown CNTs were also examined by TGA for having an idea about quality of CNTs. Thermal decomposition differences were observed during the burning of CNTs. At low temperatures, CNTs started decomposition below 400^{o}C due to burning of amorphous carbon. As the CVD, temperature increased, samples contained less amorphous carbon and more CNTs thus burning temperatures shifted toward to higher temperatures. Unlike SEM and Raman results, TGA results revealed that degree of quality was increase with increasing temperature. On the other hand, TGA results supported the Raman results for CNT production under different acetylene flow rate. It was found that, inflection temperature was almost same and optimum flow rate was in the range of in the range of 60-120 mL/min.

- According to SEM, Raman Spectroscopy and TGA results proposed optimal conditions were as follows: catalyst 4 wt % Fe-FSM-16, acetylene flow rate 80 mL/min, reaction temperature 700^{o}C.

References

[1] V.N Popov. Carbon nanotubes: properties and application. *Materials Science & Engineering R-Reports*, 43:61-102, 2004.

[2] T. Somanathan, A. Pandurangan, and D. Sathiyamoorthy. Catalytic influence of mesoporous Co-MCM-41 molecular sieves for the synthesis of SWNTs via CVD method. *Journal of Molecular Catalysis A-Chemical*, 256:193-199, 2006.

[3] M. Paradise and T. Goswami. Carbon nanotubes - Production and industrial applications. *Materials & Design*, 28:1477-1489, 2007.

[4] Q. Zhao, Y.H. Li, X.P. Zhou, T.S. Jiang, C.S. Li, and H.B. Yin. Synthesis of multi-wall carbon nanotubes by the pyrolysis of ethanol on Fe/MCM-41 mesoporous molecular sieves. *Superlattices and Microstructures,* 47: 432-441, 2010.

[5] http://www.nsec.northwestern.edu/Curriculum%20Projects/Carbon%20Allotropes.pdf, 2007.

[6] D.D. Ebbing, S.D. Gammon. *General Chemistry*. Cengage Learning, 2007.

[7] Fullerene, http://en.wikipedia.org/wiki/Fullerene, 2011

[8] S. Iijima. Helical microtubules of graphitic carbon. *Nature,* 354:56-58, 1991.

[9] M. Monthioux, and V.L. Kuznetsov. Who should be given the credit for the discovery of carbon nanotubes? *Carbon*, 44:1621-1623, 2006.

[10] R.H. Xie, Q. Rao. Third-order optical nonlinearities of chiral graphene tubules. *Chemical Physics Letters*, 313:211–216, 1999.

[11] R.Saito, G. Dresselhaus, M.S Dresselhaus. *Physical properties of carbon*

nanotubes. Imperial College Press, 1998.

[12] E. B. Barrosa, A.J. Georgii, G. Samsonidze, R.B. Capaz, A.G.S. Filho, J.M. Filho, G. Dresselhaus, M.S. Dresselhaus. Review on the symmetry-related properties of carbon nanotubes. *Physics Reports,* 431:261-302, 2006.

[13] http://www-ibmc.u-strasbg.fr/ict/vectorisation/nanotubes_eng.shtml.

[14] S. Niyogi, M.A. Hamon, H.Hu, B. Zhao, P. Bhowmik, R. Sen, M.E. Itkis, R.C. Haddon. Chemistry of single-walled carbon nanotubes. *Accounts of Chemical Research*, 35:1105-1113, 2002.

[15] P. Avouris. Carbon nanotube electronics. *Chemical Physics*, 281:429-445, 2002.

[16] J.P. Salvetat, J.M. Bonard, N.H. Thomson, A.J. Kulik, L. Forro, W. Benoit, L. Zuppiroli. Mechanical properties of carbon nanotubes. *Appl. Phys. A*, 69:255–260, 1999.

[17] N. Grobert, Carbon nanotubes –becoming clean. *Materials Today*, 10:28-35, 2007.

[18] M.M.J. Treacy, T.W. Ebbesen, J.M. Gibson. Exceptionally high Young's modulus observed for individual carbon nanotubes. *Nature*, 381:678-680, 1996.

[19] A. Krishnan, E. Dujardin, T.W. Ebbesen, P.N. Yianilos, M.M.J. Treacy, Young's modulus of single-walled nanotubes. *Physical Review B*, 58:14013-14019, 1998.

[20] E.W. Wong, P.E. Sheehan, C.M. Lieber. Nanobeam mechanics: Elasticity, strength, and toughness of nanorods and nanotubes. *Science*, 277: 1971-1975, 1997.

[21] J.P. Salvetat, A.J. Kulik, J. M. Bonard, G.A.D. Briggs. Elastic modulus of ordered and disordered multiwalled carbon nanotubes. *Advanced Materials*, 11:161-165, 1999.

[22] M.F. Yu, O. Lourie, M.J. Dyer, K. Moloni, T.F Kelly, R.S. Ruoff. Strength and breaking mechanism of multiwalled carbon nanotubes under tensile load. *Science*,

287:637-640, 2000.

[23] B.G. Demczyk, Y. M. Wang, J. Cumings, M. Hetman, W. Han, A. Zettl, R.O. Ritchie, Direct mechanical measurement of the tensile strength and elastic modulus of multiwalled carbon nanotubes. *Materials Science and Engineering a-Structural Materials Properties Microstructure and Processing,* 334:173-178, 2002.

[24] T.W. Ebbesen, P.M. Ajayan. Large-scale synthesis of carbon nanotubes. *Nature,* 358:220-222, 1992.

[25] http://students.chem.tue.nl/ifp03/Wondrous%20World%20of%20Carbon%20Nanotubes_Final.pdf, 2003

[26] T. W. Ebbesen, P. M. Ajayan, H. Hiura, K. Tanigaki. Purification of nanotubes. *Nature,* 367:519-519, 1994.

[27] T. Guo, P. Nikolaev, A. Thess, D.T. Colbert, R.E. Smalley, Catalytic growth of single-walled nanotubes by laser vaporization. *Chemical Physics Letters*, 243:49-54, 1995.

[28] E. Borowiak-Palen, E. Mendoza, A. Bachmatiuk, M.H. Rummeli, T. Gemming, J. Nogues, V. Skumryev, R. J. Kalenczuk, T. Pichler, S.R.P. Silva. Iron filled single-wall carbon nanotubes - A novel ferromagnetic medium. *Chemical Physics Letters*, 421:129-133, 2006.

[29] M.J. Yacaman, M.M. Yoshida, L. Rendon, J.G. Santiesteban. Catalytic growth of carbon microtubules with fullerene structure. *Applied Physics Letters*, 62:202-20, 1993.

[30] V.Shanov, Y.Yun , M.J. Shulz. Synthesis and characterization of carbon nanotube materials. *Journal of University of Chemical Technology and Metallurgy,* 41:377-390, 2006.

[31] G. P. Veronese, R. Rizzoli, R. Angelucci, M. Cuffiani, L. Malferrari,A. Montanari, F. Odorici. Effects of Ni catalyst-substrate interaction on carbon nanotubes growth by CVD. *Physica E-Low-Dimensional Systems & Nanostructures*, 37:21-25, 2007.

[32] R.S. Wagner, W.C.Ellis. The vapor-liquid-solid mechanism of crystal growth and its application to silicon. *Trans. Met. Soc. AIME*, 233:1053-1064, 1965.

[33] F. Ding, K. Bolton, A. Rosen. Nucleation and growth of single-walled carbon nanotubes: A molecular dynamics study. *Journal of Physical Chemistry B*, 108:17369-17377, 2004.

[34] A.C. Dupuis, The catalyst in the CCVD of carbon nanotubes - a review. Progress in Materials Science, 2005. 50(8): p. 929-961.

[35] H. Kanzow, A. Ding. Formation mechanism of single-wall carbon nanotubes on liquid-metal particles. *Physical Review B*, 60:11180-11186, 1999.

[36] W. Merchan, A.V. Saveliev, L. Kennedy, W.C. Jimenez. Combustion synthesis of carbon nanotubes and related nanostructures. *Progress in Energy and Combustion Science*, 36:696-727*,* 2010.

[37] J. Dijon, P.D. Szkutnik, A. Fournier, T.G. de Monsabert, H. Okuno, E. Quesnel, V. Muffato, E. De Vito, N. Bendiab, A. Bogner, N. Bernier. How to switch from a tip to base growth mechanism in carbon nanotube growth by catalytic chemical vapour deposition. *Carbon*, 48:3953-3963, 2010.

[38] Z. Spitalsky, D. Tasis, K. Papagelis, C. Galiotis. Carbon nanotube-polymer composites: Chemistry, processing, mechanical and electrical properties. *Progress in Polymer Science*, 35:357-401, 2010.

[39] Y. Wang, J.T.W. Yeow. A review of carbon nanotubes-based gas sensors. *Journal of Sensors,* 2009:1-24, 2009.

[40] http://www.sjsu.edu/faculty/selvaduray/page/papers/mate115/chiaoku.pdf, 2004.

[41] *IUPAC Compendium of Chemical Terminology* Edition 2, Volume 31, 1997.

[42] *IUPAC Compendium of Chemical Terminology*. Edition 2, Volume 46, 1997.

[43] P. Ugliengo, M. Sodupe, F. Musso, I.J. Bush, R. Orlando, R. Dovesi. Realistic models of hydroxylated amorphous silica surfaces and MCM-41 mesoporous material simulated by large-scale periodic B3LYP calculations. *Advanced Materials*, 20:4579-4583, 2008.

[44] J. C. Vartuli, A. Malek, W. J. Roth, C. T. Kresge, S.B. McCullen. The sorption properties of as-synthesized and calcined MCM-41 and MCM-48. *Microporous and Mesoporous Materials*, 44:691-695, 2001.

[45] T.Yanagisawa, T.Shimizu, K.Kuroda, C.Kato, The preparation of alkyltriinethylaininonium–kanemite complexes and their conversion to microporous materials. *Bull.Chem.Soc.Jpn*, 63:988-992, 1990.

[46] Q. S. Huo, D.I. Margolese, U. Ciesla, D.G. Demuth, P.Y. Feng, T.E. Gier, P. Sieger, A. Firouzi, B.F. Chmelka, F. Schuth, G.D. Stucky. Organization of organic-molecules with inorganic molecular-species into nanocomposite biphase arrays. *Chemistry of Materials*, 6:1176-1191, 1994.

[47] Q. Huo, D.I. Margolese, G.D. Stucky. Surfactant control of phases in the synthesis of mesoporous silica-based materials. *Chem. Mater*, 8:1147-1160, 1996.

[48] http://www.gly.uga.edu/Schroeder/geol6550/CM06.html, 2008.

[49] T. Kimura, K. Kuroda. Ordered mesoporous silica derived from layered silicates. *Advanced Functional Materials*, 19:511-527, 2009.

[50] J.S. Beck, J.C. Vartuli, W.J. Roth, M.E. Leonowicz, C.T. Kresge, K.D. Schmitt, C.T.W. Chu, D.H. Olson, E.W. Sheppard. A new family of mesoporous molecular sieves prepared with liquid crystal templates. *J. Am. Chem. Sot.*, 114:10834-10843, 1992.

[51] J.C. Vartuli, C.T. Kresge, M.E. Leonowicz, A.S. Chu, S.B. Mccullen, I.D. Johnsen, E.W. Sheppard,. Synthesis of mesoporous materials - liquid-crystal templating versus intercalation of layered silicates. *Chemistry of Materials*, 6:2070-2077, 1994.

[52] A.Corma. Preparation and catalytic properties of new mesoporous materials. *Topics in Catalysis*, 4:249–260, 1997.

[53] T. Kimura, T. Kamata, M. Fuziwara, Y. Takano, M. Kaneda, Y. Sakamoto, O. Terasaki, Y. Sugahara, K. Kuroda. Formation of novel ordered mesoporous silicas with square channels and their direct observation by transmission electron microscopy. *Angewandte Chemie-International Edition*, 3:3855-3859, 2000.

[54] S. Inagaki, A. Koiwai, N. Suzuki, Y. Fukushima, K. Kuroda. Syntheses of highly ordered mesoporous materials, FSM-16, derived from kanemite. *Bulletin of the Chemical Society of Japan*, 69:1449-1457, 1996.

[55] K.S.W. Sing, D.H. Everett, R.A.W. Haul, L. Moscou, R.A. Pierotti, J. Rouquerol, T.Siemieniewska. Reporting physisorption data for gas solid systems with special reference to the determination of surface-area and porosity. *Pure and Applied Chemistry*, 57:603-619, 1985.

[56] M. Ghattas. Cobalt modified mesoporous FSM-16 silica: Characterization and catalytic study. *Microporous and Mesoporous Materials* 97:107-113, 2006.

[57] A. Ruban, B. Hammer, P. Stoltze, H.L. Skriver, J.K. Nørskov. Surface electronic structure and reactivity of transition and noble metals. *Journal of Molecular Catalysis A: Chemical*, 115:421–429, 1997.

[58] A. Kukovecz, Z. Konya, N. Nagaraju, I. Willems, A. Tamasi, A. Fonseca, J. B. Nagy, I. Kiricsi. Catalytic synthesis of carbon nanotubes over Co, Fe and Ni containing conventional and sol-gel silica-aluminas. *Physical Chemistry Chemical Physics*, 2:

3071-3076, 2000.

[59] R. Sen, A. Govindaraj, C.N.R. Rao .Carbon nanotubes by the metallocene route. *Chemical Physics Letters*, 267:276-280, 1996.

[60] K. Hernadi, A. Fonseca, J.B. Nagy, A. Siska, I.Kiricsi. Production of nanotubes by the catalytic decomposition of different carbon-containing compounds. *Applied Catalysis A: General,* 199:245–255, 2000.

[61] G.S. Duesberg, A.P. Graham, M. Liebau, R. Seidel, E. Unger, F. Kreupl, W. Hoenlein. Growth of isolated carbon nanotubes with lithographically defined diameter and location. *Nano Letters*, 3:257-259, 2003.

[62] C. Klinke, J.M. Bonard, K. Kern. Comparative study of the catalytic growth of patterned carbon nanotube films. Surface Science, 492:195-201, 2001.

[63] M.A. Ermakova, D.Y. Ermakov, A.L. Chuvilin, G. Kuvshinov. Decomposition of methane over iron catalysts at the range of moderate temperatures: The influence of structure of the catalytic systems and the reaction conditions on the yield of carbon and morphology of carbon filaments. Journal of Catalysis, 201:183-197, 2001.

[64] D. Venegoni, P. Serp, R. Feurer, Y. Kihn, C. Vahlas, P. Kalck. Parametric study for the growth of carbon nanotubes by catalytic chemical vapor deposition in a fluidized bed reactor. *Carbon*, 40:1799-1807, 2002.

[65] Y.S. Cho, G.S. Choi, S. Y. Hong, D. Kim. Carbon nanotube synthesis using a magnetic fluid via thermal chemical vapor deposition. *Journal of Crystal Growth*, 243:224-229, 2002.

[66] R. Atchudan, A. Pandurangan, T. Somanathan. Bimetallic mesoporous materials for high yield synthesis of carbon nanotubes by chemical vapour deposition techniques. *Journal of Molecular Catalysis A-Chemical*, 309:146-152, 2009.

[67] Y.M. Li, W. Kim, Y.G. Zhang, M. Rolandi, D.W. Wang, H.J. Dai. Growth of single-walled carbon nanotubes from discrete catalytic nanoparticles of various sizes. *Journal of Physical Chemistry B,* 105:11424-11431, 2001.

[68] C.L. Cheung, A. Kurtz, H. Park, C.M. Lieber. Diameter-controlled synthesis of carbon nanotubes. *Journal of Physical Chemistry B,* 106:2429-2433, 2002.

[69] T. Somanathan, A. Pandurangan. Catalytic activity of Fe, Co and Fe-Co-MCM-41 for the growth of carbon nanotubes by chemical vapour deposition method. *Applied Surface Science*, 254:5643-5647, 2008.

[70] H. Ago, T. Komatsu, S. Ohshima, Y. Kuriki, M. Yumura. Dispersion of metal nanoparticles for aligned carbon nanotube arrays. *Applied Physics Letters*, 77:79-81, 2000.

[71] J.F. Colomer, C. Stephan, S. Lefrant, G. Van Tendeloo, I. Willems, Z. Konya, A. Fonseca, C. Laurent,J.B. Nagy. Large-scale synthesis of single-wall carbon nanotubes by catalytic chemical vapor deposition (CCVD) method. *Chemical Physics Letters*, 317:83-89, 2000.

[72] Z.F. Ren, Z.P. Huang, J.W. Xu, J.H. Wang, P. Bush, M.P. Siegal, P.N. Provencio. Synthesis of large arrays of well-aligned carbon nanotubes on glass. *Science,* 282:1105-1107, 1998.

[73] J. Jiao, S. Seraphin. Single-walled tubes and encapsulated nanoparticles: comparison of structural properties of carbon nanoclusters prepared by three different methods. *Journal of Physics and Chemistry of Solids*, 61:1055-1067, 2000.

[74] E.F. Kukovitsky, S.G. L'vov, N.A. Sainov, V.A. Shustov, L.A. Chernozatonskii. Correlation between metal catalyst particle size and carbon nanotube growth. *Chemical Physics Letters,* 355:497-503, 2002.

[75] S.B. Sinnott, R. Andrews, D. Qian, A.M. Rao, Z. Mao, E.C. Dickey, F. Derbyshire Model of carbon nanotube growth through chemical vapor deposition. *Chemical*

Physics Letters, 315:25–30, 1999.

[76] C. P. Deck, K. Vecchio. Prediction of carbon nanotube growth success by the analysis of carbon–catalyst binary phase diagrams. *Carbon*, 44:267–275, 2006.

[77] C.J. Lee, J. Park, J.A. Yu. Catalyst effect on carbon nanotubes synthesized by thermal chemical vapor deposition. *Chemical Physics Letters*, 360:250-255, 2002.

[78] M. Hansen, K. Anderko. *Constitution of binary alloys*. McGraw-Hill, 1958.

[79] V. Ivanov, J.B. Nagy, P. Lambin, A. Lucas, X.B. Zhang, X.F. Zhang, D. Bernaerts, G. Vantendeloo, S. Amelinckx, J. Vanlanduyt. The study of carbon nanotubules produced by catalytic method. *Chemical Physics Letters,* 223:329-335, 1994.

[80] A. Matsumoto, T. Sasaki, N. Nishimiya, K.Tsutsumi. Thermal stability and hydrophobicity of mesoporous silica FSM-16. *Colloids and Surfaces A: Physicochemical and Engineering Aspects*, 203:185-193, 2001.

[81] A. de Lucas, L. Rodríguez, J. Lobato, P. Sánchez. Synthesis of crystalline δ-$Na_2Si_2O_5$ from sodium silicate solution for use as a builder in detergents. *Chemical Engineering Science,* 57:479-486, 2001.

[82] W. Hammond, E. Prouzet, S.D. Mahanti, T.J. Pinnavaia. Structure factor for the periodic walls of mesoporous MCM-41 molecular sieves. *Microporous and Mesoporous Materials*, 27:19-25, 1999.

[83] R. Kohn,and M. Froba. Nanoparticles of 3d transition metal oxides in mesoporous MCM-48 silica host structures: Synthesis and characterization. *Catalysis Today*, 68:227-236, 2001.

[84] X. Xie, M. Satozawa, K. Kunimori, S. Hayashi. NMR study of pore surface and size in the mesoporous material FSM-16. *Microporous and Mesoporous Materials*, 39:25-35, 2000.

[85] K.J. Chao, C.N. Wu, H. Chang, L.J. Lee, S. F. Hu. Incorporation of vanadium in mesoporous MCM-41 and microporous AFI zeolites. *Journal of Physical Chemistry B*, 101:6341-6349, 1997.

[86] M. Katoh, M. Shinkawa, T. Tomida. Adsorption properties of gases on mesoporous chromium silicate. *Journal of Colloid and Interface Science,* 277:280-284, 2004.

[87] Y. Kitayama, H. Asano, T. Kodama, J.Abe. Synthesis of Sn- Incorporated Folded Sheets Mesoporous Materials (FSM-16). *Journal of Porous Materials*, 5:139-146, 1998.

[88] http://www.sv.vt.edu/classes/MSE2094_NoteBook/96ClassProj/examples/FeC.gif, 1999.

[89] H.W. Pollack, *Materials Science and Metallurgy*. Prentice Hall, 1988.

[90] Zhang, K.J. Smith. A kinetic model of CH_4 decomposition and filamentous carbon formation on supported Co catalysts. *Journal of Catalysis*, 231:354-364, 2005.

[91] S.G. Zavarukhin, G.G. Kuvshinov. The kinetic model of formation of nanofibrous carbon from CH4-H-2 mixture over a high-loaded nickel catalyst with consideration for the catalyst deactivation. *Applied Catalysis A-General*, 272:219-227, 2004.

[92] C.M. Chen, Y.M. Dai, J.G. Huang, J.M. Jehng. Intermetallic catalyst for carbon nanotubes (CNTs) growth by thermal chemical vapor deposition method. *Carbon,* 44:1808-1820, 2006.

[93] M.S. Dresselhaus, G. Dresselhaus, R. Saito, A. Jorio. Raman spectroscopy of carbon nanotubes. *Physics Reports-Review Section of Physics Letters*, 409:47-99, 2005.

[94] S. Scaccia, M. Carewska, P.P. Prosini. Study of purification process of single-walled carbon nanotubes by thermoanalytical techniques. *Thermochimica Acta*,

435:209-212, 2005.

[95] C.J. Lee, J. Park, Y. Huh, J.Y. Lee. Temperature effect on the growth of carbon nanotubes using thermal chemical vapor deposition. *Chemical Physics Letters*, 343:33-38, 2001.